The Impact of Mountain Topography and Environmental Flow on the Predictability of Localized Thunderstorms

地形と環境風が局地的な雷雨の予測可能性に及ぼす影響

Pin-Ying Wu

Division of Earth and Planetary Sciences,

Graduate School of Science, Kyoto University

June 2022

Abstract

The numerical simulations of localized thunderstorms characterized by diurnal cycles are conducted with the Weather Research and Forecasting (WRF) model in an idealized framework to investigate predictability and the associated error growth. Identical twin experiments are performed with different topography and flow conditions to assess the impacts of these conditions. The differences between the control and perturbed simulations in each twin experiment are regarded as the errors, measured by a metric referred to as convective moist difference total energy (CMDTE) proposed in this study. The results show that mountain topography restrains the error growth during the convection initiation, while this effect is sensitive to the mountain geometry and the background wind. Specifically, topographic effects are more evident with a higher and narrower mountain and less apparent without background wind. Nevertheless, the restraining effect of topography on error growth becomes unclear when moist convection matures and triggers rapid error growth through diabatic heating from latent release. This rapid error growth destroys the predictability of thunderstorms. Consequently, the predictability limit of thermally induced thunderstorms is determined by the time of the maximum convective activity at which mountain topography affects little. In comparison, environmental flows affect the time of losing predictability because of the changes in the maximum convective activity time. The predictability limit assessed by the hourly rainfall patterns also suggests less impact from topography than environmental flows. Conversely, topography notably impacts the prediction of several-hours accumulated rainfall due to its restraint on the error of moisture field and the rainfall distribution at the domain scale.

Contents

List of Figures

List of Tables

Chapter 1 Introduction

The atmosphere is a dynamical system that contains various weather phenomena. In the troposphere, water vapor plays an important role in the variation of the weather. The phase transition of water vapor results in the formation of clouds. The convective circulation with moist processes related to the phase transition of water, which is usually referred to as moist convection, forms cumulus. When moist convection is deep enough in the vertical direction, it results in precipitating convective clouds, or cumulonimbus. Thunderstorms are vigorous cumulonimbus resulting from deep moist convection that brings heavy rainfall or hail together with thunder and lightning, usually accompanying with strong wind. Thunderstorms are highly-impact weather phenomena that influence people's daily lives and commercial activities, sometimes even leading to the loss of property and human life (Changnon 2001). People use day-to-day weather forecasts to make their decisions of daily activity and prevent disasters. Nowadays, a great part of weather forecasts relies on the dynamical prediction provided by numerical weather prediction (NWP) models. Thus, it is important to improve the ability of NWP models and provide more accurate predictions, especially for severe weather such as thunderstorms.

This study investigates the predictability of thunderstorms, aiming to provide new insight into the application of NWP models on high impact weather phenomena at convective scales. We especially focus on the thermally induced thunderstorms in the solar radiative diurnal cycles, which have short time scales of one to a few hours and localized spatial scales at O(10 km). In this chapter, the thermally induced thunderstorms in diurnal cycles are introduced first, and then a brief literature review of atmospheric predictability is provided. Finally, the predictability of thunderstorms and the purpose of this study are further described.

1.1 Thermally induced thunderstorms in diurnal cycles

Thermally induced thunderstorms during the daytime, usually in the afternoon, are common phenomena on fair weather days in warm seasons over the world (e.g., Wallace 1975; Kerns et al. 2010; Nomura and Takemi 2011). On fair-weather days with a weak synoptic forcing condition in warm seasons, solar radiation heats the land surface and low-level atmosphere in the daytime, leading to the development of convective boundary conditions that are favorited by convection initiation (Grimsdell and Angevine 2002). These conditions promote thunderstorms to occur during the daytime and dissipate at night, resulting in clearer rainfall diurnal cycles than those in other seasons (Chen et al. 1999).

For moist convection developing under solar radiative heating, environmental conditions such as humidity and atmospheric instability are crucial for its initiation and development (e.g., Crook 2001; Nomura and Takemi 2011). For example, Takemi (2014) indicated the importance of middle-level moisture for the afternoon rainfall caused by thunderstorms over Nobi Plain, Japan, and its surrounding mountains by examining the environmental conditions from operational meteorological data.

Topography, which greatly decides the distribution of atmospheric fields like wind and moisture, is then an important factor that participates in the generation of thermally induced thunderstorms. Generally, mountain topography affects the development of moist convection and accompanying precipitation in various ways, such as mountain waves or blocking effects on precipitation (Roe 2005; Houze 2012; Kirshbaum et al. 2018). Previous studies have indicated the impact of topography on the intensity and distribution of thunderstorms and precipitation by investigating observation data (Chen and Chen 2003; Kovacs and Kirshbaum 2016; Cheng and Yu 2019) or results from numerical models (Fu and Guo 2012; Flesch and Reuter 2012; White et al. 2021).

Topography also impacts the diurnal cycle of moist convection and rainfall (Wallace 1975; Nesbitt et al. 2008; Romatschke and Houze 2010; Jury 2020). In warm seasons, the largest day-night differences are usually observed over mountain areas (Kerns et al. 2010; Levizzani et al. 2010; Li et al. 2017). During the diurnal cycle of solar radiation, topography results in different heating and cooling between elevated mountains and the surrounding valley or plain, driving diurnally varying circulation (Vergeiner and Dreiseitl 1987; Whiteman 1990; Demko et al. 2009; Schmidli 2013). The heated mountain and the corresponding thermally driven circulation then further affect the development and structure of the daytime boundary layer which is important for convection development (Banta 1984; Gopalakrishnan et al. 2000; Serafin et al. 2018). In this way, topography plays an important role in the generation and development of thermally induced thunderstorms in diurnal cycles as well as the accompanying rainfall (Fig. 1.1).

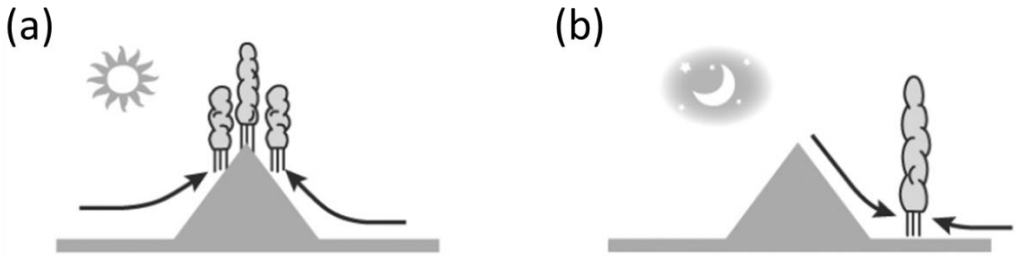

Figure 1.1 Schematic of the mechanisms for convective initiation over mountains in a solar radiation cycle from Houze (2012, their Fig. 3). Copyright 2012 by the American Geophysical Union.

In addition, the existence of prevailing winds adds to the complexity of how topography affects the development of thunderstorms. Previous studies have indicated the importance of environmental wind conditions on the organization of convective clouds (Fu and Guo 2012; Muller 2013). It also has been reported that topography can affect the formation of clouds by changing the flow distribution under a prevailing wind (Smolarkiewicz et al. 1988; Akaeda et

al. 1995; Kirshbaum and Durran 2005; Johnston et al. 2018). Banta and Schaaf (1987) investigated the observation data over Rocky Mountain and showed that the "genesis zones" of thunderstorms are relevant to the prevailing wind. They proposed four different patterns of the interaction between the background wind and mountain terrain that trigger deep convection (Fig. 1.2), highlighting the roles of environmental wind and topography on the generation of thunderstorms.

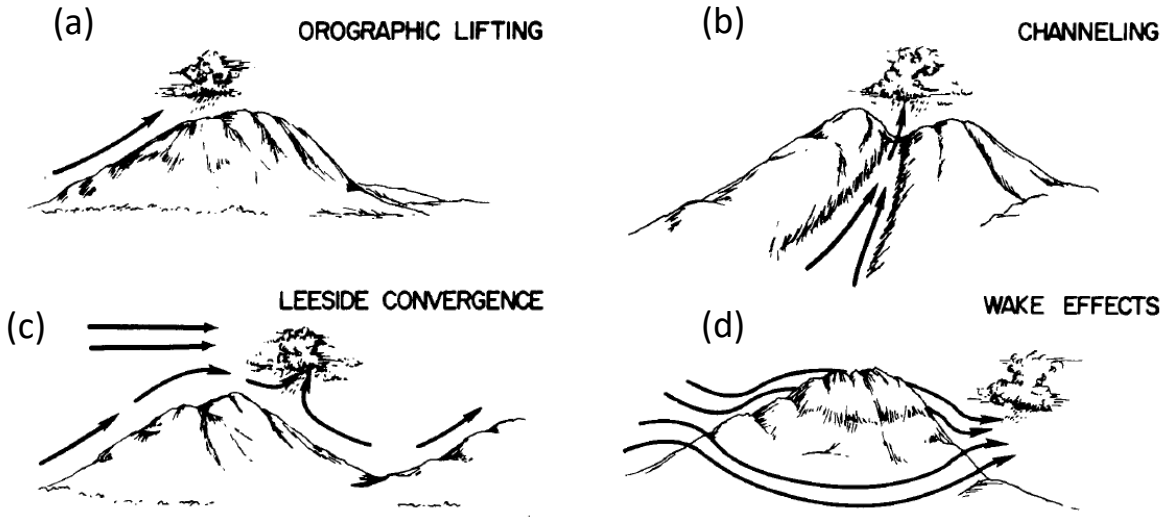

Figure 1.2 Schematic of the mechanisms which lead to moist convection near mountains from Banta and Schaaf (1987, their Fig. 1). Published 1987 by the American Meteorological Society.

On fair weather days in warm seasons, background prevailing winds can further interact with the thermally driven circulation over mountain topography and then induce the occurrence of thunderstorms (Carbone et al. 1995; Chen and Lin 1997). For example, deep moist convection could be initiated by the convergence of prevailing wind and the upslope wind on the lee side of mountains (Fig 1.2c). The environment for the thermally induced thunderstorms over mountainous areas under the presence of background wind would be more complicated because the direction, speed, and vertical shear of the prevailing wind could

further affect where the thunderstorm will occur around the mountains (Chen et al. 2002; Hagen et al. 2011). Thus, the occurrence, movement, and organization of thermally induced thunderstorms are complicatedly impacted by both the topography and flow conditions at the same time (Kuo and Wu 2019; Miao and Yang 2020).

Overall, predicting thermally induced thunderstorms over mountainous areas is challenging because such thunderstorms result from multiple processes in the atmosphere, including radiation heating, the building of convective boundary layer, the thermally driven flow, and the interaction of prevailing winds and topography. To accurately predict thermally induced thunderstorms, numerical models have to correctly capture crucial processes that would impact the initiation and development of moist deep convection, which is still a challenging task for current operational models. Meanwhile, some of these processes, such as the turbulence in the boundary layer around mountains or the microphysical processes in convective clouds, have relatively small characteristic scales and high nonlinearity, which implies an intrinsic predictability limit even with the use of a model simulating these processes perfectly. In the following, the general atmospheric predictability is briefly introduced in Section 1.2 first; then, an introduction of the predictability of thunderstorms is presented in Section 1.3.

1.2 Atmospheric predictability

The atmosphere is a chaotic system with limited predictability, i.e., the time length of capable numerical predictions is finite. Specifically, because of the chaotic nature of the atmosphere, the predictable time range of an instantaneous dynamical prediction from an NWP system cannot be extended infinitely by continuously reducing the errors in the initial conditions (Palmer et al. 2014). Because the error in the model initial condition is inevitable, the limit of atmospheric predictability is an unavoidable issue when using NWP models, and

has been noticed and extensively discussed since the early days of the development of NWP. This section introduces the background and current understanding of atmospheric predictability. The introduction of the predictability of thunderstorms will be presented in the next section.

1.2.1 Background and literature review

The concept of NWP can be traced back to the early 20th century (Bjerknes 1904; Richardson 1922), while NWP did not actually come true before the achievement of sufficient computing power in the 1950s (Charney et al. 1950). After the 1950s, the capability of NWP models was gradually recognized. More and more operational centers started to use numerical models for weather prediction at this time (Persson 2005).

In the meantime, the unstable dynamical natures of the atmosphere in which a small perturbation would amplify and contaminate predictions were also indicated by studies that developed mathematical models of atmospheric flows (Charney 1947; Thompson 1953). It was natural to ask how far ahead the weather can be predicted by numerical models. Early in 1949, the growth of small disturbances and the ultimate predictable limit were discussed with the use of a relatively simple baroclinic wave model (Eady 1949). Thompson (1957) investigated the maximum range beyond which detailed forecasts will lose economic value. He concluded that beyond a certain time range, the rapid error growth nature will destroy the benefits of doubling the density of weather stations; this basic framework of predictability is still valid today.

Later, Lorenz (1963) proposed a simple three-variable model derived from the equations of thermal convection. The model, which is now well known as the Lorenz-63 model, provides non-periodic solutions with nonlinear dynamics. With this model, Lorenz indicated the dependence of forecast error on the initial states for a nonlinear and non-periodic dynamical

system; i.e., a small initial difference between two solutions will grow with time and become as large as the difference between two randomly selected states. Lorenz (1963) put forth a fundamental theory of the chaotic system, inspired many later studies, and have motivated scientists to understand the nonlinear dynamics. Lorenz (1963) anticipated that it is impossible to predict the weather in the distant future unless the current situation is known accurately. The inherent finite range of predictability was further investigated in Lorenz's later seminal paper in 1969.

Lorenz (1969) used a simple mathematical model based on the equations of two-dimensional vorticity flows, which describes a multi-scale deterministic fluid system with a one-dimensional cascade of error energy in a wide range of wavenumbers. Besides the error growth with time, Lorenz (1969) showed that errors at smaller scales grow more rapidly. He indicated that once the initial error has been refined to a certain point, the finite range of predictability cannot be noticeably extended by further improving the initial condition through resolving finer scales because the more rapid error growth at finer scales would nearly offset the expected gain of predictability. Meanwhile, due to more rapid error growth and smaller background energy at smaller scales, Lorenz expected that the saturation of the error at small scales would happen more quickly, resulting in lower predictability of phenomena at smaller scales (Fig. 1.3). In other words, atmospheric predictability is scale dependent.

After Lorenz (1969), many follow-up studies in the late 20th century have increasingly paid attention to predictability problems. The limit of predicting multi-scale chaotic flows like the atmosphere was widely recognized. Studies investigated error growth properties at different scales and estimated the finite predictability range by using various numerical models, such as the models of turbulent flows (Leith and Kraichnan 1972; Métais and Lesieur 1986; Boffetta et al. 1997) and baroclinic waves (Daley 1981), and also by using operational NWP models to provide more realistic perspectives (Lorenz 1982; Dalcher and Kalnay 1987; Boer

1994; Simmons et al. 1995). These early studies laid the foundation for the understanding of predictability. For example, Dalcher and Kalnay (1987) used a simple error growth model modified from the one in Lorenz (1982) to estimate the error growth rate and the theoretical predictability time at different scales, considering both situations of perfect and imperfect models (refer to Eq. (1.1)). They defined the limit of predictability at the time when error variance reached 95% of the saturation value and showed that predictability decreases monotonically with the scale. The estimation method and the error growth model in Dalcher and Kalnay (1987) are still valid and being used nowadays (Judt 2018; Zhang et al. 2019).

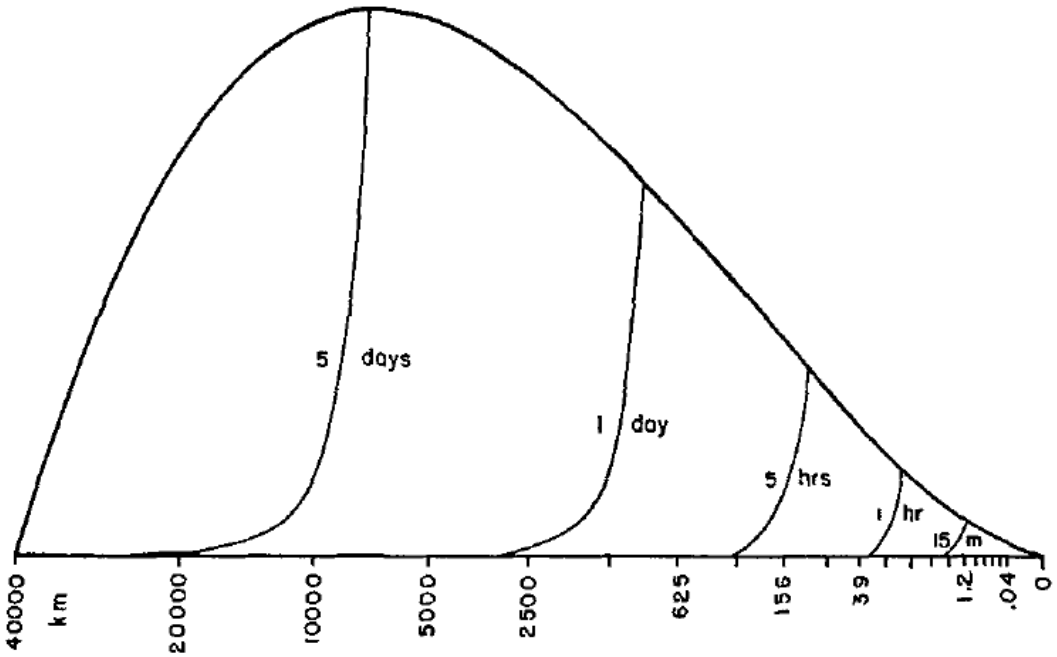

Figure 1.3 Schematic diagram showing that energy spectra of error saturating first at small scales, taken from Lorenz (1969, his Fig. 2). The horizontal axis shows the length scales. The thick curve depicts the background energy spectrum; the thin curves represent the error at different lead times. Copyright 1969 Blackwell Munksgaard.

At the same time, since the initial error of NWP is inevitable, studies also developed ensemble prediction techniques in which a number of slightly different initial conditions are incorporated to deal with the uncertainty of weather predictions (Tracton and Kalnay 1993;

Toth and Kalnay 1993). Toth and Kalnay (1993), proposing the procedure to produce appropriate ensemble initial conditions, illustrated different modes of error growth dynamics at synoptic and convective scales (Fig. 1.4). The faster error growth mode at convective scales was considered irrelevant to the instability embedded in baroclinic modes corresponding to synoptic-scale weather. Therefore, Toth and Kalnay (1993) suggested that the perturbations resulting in such convective-scale growth modes should be avoided when producing initial conditions of an ensemble prediction system for synoptic-scale weather.

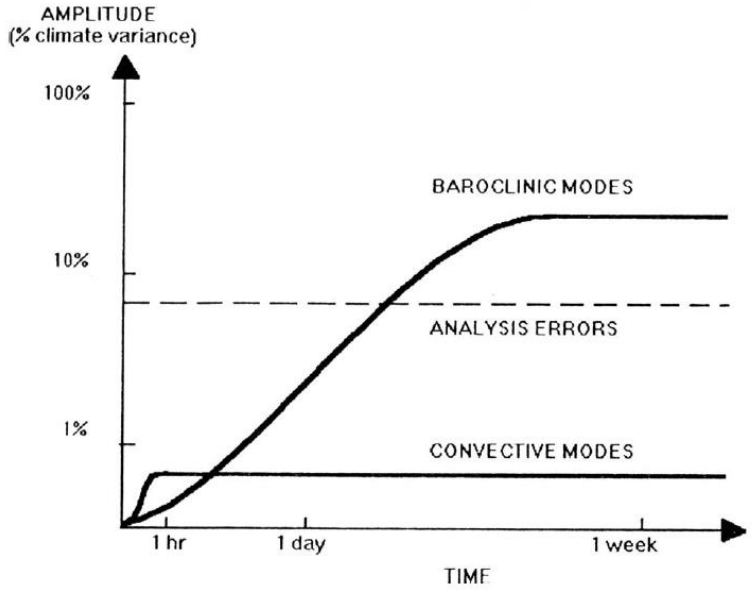

Figure 1.4 Schematic diagram showing that error growth mode at convective scales is more rapid and has smaller saturation level and earlier saturation time than that at synoptic scales. From Toth and Kalnay (1993, their Fig. 6). © American Meteorological Society. Used with permission.

In the 21st century, atmospheric predictability is investigated by numerous studies. The theoretical understanding of chaotic dynamics and predictability has been achieved by using relatively simplified models, like turbulence models (e.g., Morss et al. 2009; Ngan et al. 2009; Durran and Gingrich 2014; Boffetta and Musacchio 2017). Such studies benefited from simplified models without complicated physical parameterizations for their better flexibility

in conducting numerical experiments and easier interpretation of the results. Those studies have deepened theoretical understandings that would help to interpret results from more complex models. For example, by revisiting and generalizing the turbulence model in Lorenz (1969), Rotunno and Snyder (2008) confirmed the hypothesis of Lorenz (1969) about the relationship of predictability and the slope of a flow's kinetic energy spectrum. They demonstrated that in the model based on the two-dimensional vorticity equation (with a "−3" spectrum slope), the predictability is unlimited; and in the model applied to the surface quasi-geostrophic equations (with a "−5/3" spectrum slope), the predictability is limited. Nowadays, studies using relatively simplified models continue advancing the understanding of predictability (Leung et al. 2019; Clark et al. 2021). Recently, Sun and Zhang (2020) proposed a theoretical framework based on the hybrid energy spectrum with slopes equal to −3 and −5/3 by revisiting the model described in Rotunno and Snyder (2008), further connecting the idealized behavior of flows and the real atmosphere.

However, we still need to keep in mind that the real atmosphere is more complicated than idealized turbulence models. The findings from relatively simplified models might not well explain the behavior of the real atmosphere. Thus, more realistic models that simulate the behaviors of the atmospheric flows with parameterized physical processes, such as NWP models, are also extensively used to explore atmospheric predictability. Using NWP models, studies can be performed with either global or limited-area models. With global models, the error growth and the predictability of the atmospheric flows can be estimated at wide scales (Harlim et al. 2005; Mapes et al. 2008; Ngan and Eperon 2011; Buizza and Leutbecher 2015). Since global models play an important role in weather forecasting, these studies have been helping researchers and forecasters to improve NWP models and interpret model results for synoptic weather forecasts. Recently, because of the improvement in computing power, scientists are able to use convection-permitting global models and further advance our

understanding of the predictability limit resulting from the error growth associated with both convective activity and synoptic weather systems at various scales (Judt 2018; Zhang et al. 2019; Judt 2020).

Meanwhile, higher-resolution simulations can be applied with limited-area models to investigate the error growth dynamics at finer scales (Leoncini et al. 2010; Weyn and Durran 2018). Limited-area models consume less computing resource than global models for the same resolution. Thus, numerous studies are performed with various limited-area models to investigate atmospheric predictability, especially with regard to the behaviors of moist convection and precipitation (Bei and Zhang 2007; Leoncini et al. 2010; Selz and Craig 2015; Zhang et al. 2016; Weyn and Durran 2017; Potvin et al. 2017). Limited-area models have been used to study the predictability of specific phenomena at different scales, such as typhoons (Judt et al. 2016), Mei-yu front (Zhuang et al. 2020), Madden-Julian Oscillation (Ying and Zhang 2017), and baroclinic waves (Zhang et al. 2007; Bei and Zhang 2014). Many sensitivity tests for understanding predictability at different conditions are also performed with idealized frameworks of limited-area models by changing model configuration such as grid-spacing (Potvin et al. 2017; Weyn and Durran 2018), background wind conditions (Zhang and Tao 2013; Weyn and Durran 2017), and other parameters that may affect predictability such as Rossby number (Bierdel et al. 2018).

Atmospheric predictability has been extensively investigated since the days of Lorenz. Sometimes, the term “predictability” could be referred to as slightly dispersed definitions and descriptions in various literature. In a broad sense, the contents of studies investigating “predictability” could vary from the investigation of error growth dynamics and the estimation of the predictability limit (Zhang et al. 2007; Hohenegger and Schär 2007b; Buizza and Leutbecher 2015; Zhuang et al. 2020) to the evaluation of forecast skill and the ability of NWP models to reproduce particular weather events (Surcel et al. 2015; Fang et al. 2011; Kotsuki et

al. 2019; Cheng et al. 2020). In the context of assessing the limit of NWP, some literatures separated the concept of predictability into two perspectives: intrinsic and practical (Melhauser and Zhang 2012; Sun and Zhang 2016; Ying and Zhang 2017; Wu et al. 2020). Intrinsic predictability refers to an upper bound of the length of capable predictions that cannot be broken even if the model and initial conditions are nearly perfect (Lorenz 1969). Intrinsic predictability is an inherent property of chaotic dynamic systems, varying with time and space in the case of atmospheric predictability. Identical twin experiments under a perfect model assumption are the approach usually utilized to investigate intrinsic predictability (e.g., Zhang et al. 2016; Judt 2018; Zhang et al. 2019). On the other hand, practical predictability is more like the ability to make skillful predictions using given realistic uncertainties in the current best-known NWP procedure (Lorenz 1982; Froude et al. 2013; Magnusson and Källén 2013; Zhang et al. 2015; Surcel et al. 2015; Buizza and Leutbecher 2015; Nielsen and Schumacher 2016). In addition to the limit because of the chaotic nature of dynamic systems, practical predictability is limited by the deficiencies in the current procedures of NWP, including observations, data assimilation, initial and boundary conditions, and numerical models.

From both perspectives, previous studies have largely clarified the nature of error growth and predictability and specified the model components that need improvement. In this study, we focus on the limit of predicting thunderstorms by using identical twin experiments which estimate the departures of two initially close model states using the same model configuration. The investigation will be focused on the predictability of thunderstorms limited by the growth of the initial uncertainty. The introduction of the atmospheric predictability limit and the error growth dynamic are provided in the following.

1.2.2 Current understanding of the atmospheric predictability limit

The limit of atmospheric predictability is a widely accepted concept nowadays. In previous studies, the error growth rate is usually used to imply the degree of predictability

(Kalnay 2002; Mu et al. 2017). Rapid error growth implies low predictability and vice versa. The evolution of initial errors in chaotic systems whose solution exists in a bounded space shares some common properties: the error growth develops exponentially at first, but will finally slow down and reach a certain saturate level. The level of saturation is determined by the average distance between two randomly selected states in the system. This error growth properties can be described by a simple error growth model (Dalcher and Kalnay 1987; Kalnay 2002):

$$\frac{d\varepsilon}{dt} = (\alpha\varepsilon + \beta)(1 - \varepsilon). \tag{1.1}$$

In the above equation, *t* represents time, and ε is the normalized error which makes ε approximately equal to 1 at a long time; α represents the error growth rate, and β is an external error source, normally referred to as the contribution from model deficiencies (Dalcher and Kalnay 1987; Reynolds et al. 1994; Magnusson and Källén 2013). Figure 1.5 shows the error growth illustration plotted according to Eq. (1.1). The time when the error becomes close to the saturation level is usually seen as the time of predictability limit (Dalcher and Kalnay 1987; Zhang et al. 2019).

In the case of the real atmosphere, the nature of error growth rate, and so does the predictability, varies in time and space, depending on the underlying dynamics and instabilities. For synoptic-scale weather in the extratropical regions, the predictability limit was estimated to be around two to three weeks by using global models (Lorenz 1982; Simmons and Hollingsworth 2002; Froude et al. 2013; Buizza and Leutbecher 2015; Zhang et al. 2019).

In comparison with the midlatitudes, some studies expected greater potential predictability at synoptic scales in the tropics (Kalnay 2002; Straus and Paolino 2008). Recently, Judt (2020) indicated that equatorial waves play a role in the higher predictability of the tropics. Meanwhile, other studies showed that the predictability in the tropics could vary

from several days at small scales to around two weeks at scales larger than 1000 km (Ying and Zhang 2017; Mapes et al. 2008). Since it was not until recently that NWP models became able to better represent the activity of convection, which dominates the weather in the tropic, more studies are still needed to explore the predictability in the tropics.

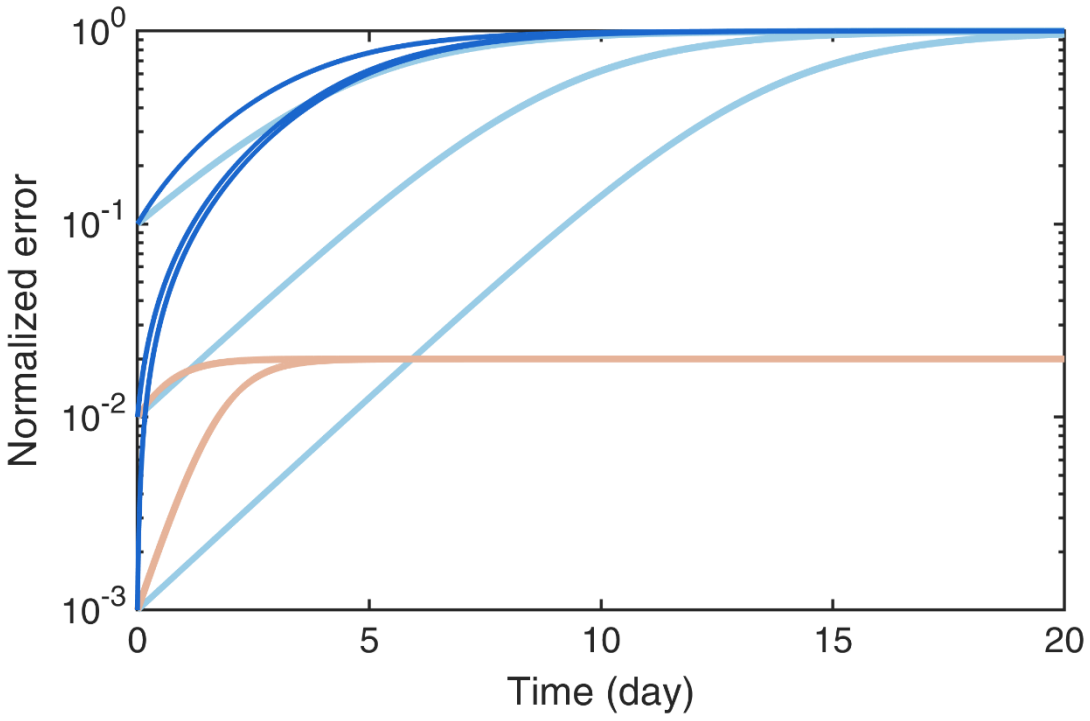

Figure 1.5 Schematic diagram illustrating the error growth properties in chaotic systems. Starting with the ε having amplitude smaller than one, two, and three orders of the saturation level, the light- and dark-blue curves are plotted according to Eq. (1.1) using $\alpha = 0.51$ and $\beta = 0$ and 0.0054, respectively, with reference to the values of the summer case in Dalcher and Kalnay (1987; their table 2). The orange curves illustrate the possible situation of the error growth at smaller scales, imitating the one shown in Fig. 1.4.

Similarly, at meso- and convective scales, the attention was not widely paid until recent two decades after we had enough computing resources to simulate the development of convection explicitly. It has been expected that the predictability of phenomena at convective scales is low because of the more rapid error growth at smaller scales. However, different specific weather phenomena, such as tropical cyclones, Mei-yu front, and mesoscale

convective systems, have their own nature of error growth dynamics and predictability. The underlying dynamics, such as environmental flows (Zhang and Tao 2013; Weyn and Durran 2017; Wu et al. 2020) or synoptic-scale weather conditions (Walser et al. 2004; Johnson et al. 2014; Weyn and Durran 2019; Zhuang et al. 2020), could also affect the convection development and the following error growth dynamics and predictability. Therefore, the predictability at meso- and convective scales is highly flow-dependent and varies from case to case (Done et al. 2012; Johnson et al. 2014; Nielsen and Schumacher 2016; Walser et al. 2004; Weyn and Durran 2019), making it difficult to have a universal convincing estimation of predictability. While increasing attention is being paid recently, studies on meso- and convective-scale predictability are underway. Further introduction to the predictability of thunderstorms is provided in the next section.

Besides investigating the finite range of predictability, studies have been trying to explain the factors that determine the error growth that eventually limits predictability. From the relationship between atmospheric dynamics and predictability, the nature of the spectral energy cascade of atmospheric flows is usually considered when investigating atmospheric predictability. Nowadays, the energy spectra of the real atmosphere have been shown to have near -3 and $-5/3$ slope at synoptic-scale and mesoscale, respectively, by both observation data (Nastrom and Gage 1985) and numerical model outputs (Skamarock et al. 2014). Judt (2018) used a convective-permitting global model and showed that error growth resembles the case of turbulent flow with a $-5/3$ spectrum slope at mesoscale and mirrored the case of turbulent flow with a -3 slope at synoptic scales.

Based on the theoretical understanding (Lorenz 1969; Rotunno and Snyder 2008), the weather at synoptic scales whose energy spectra show a -3 slope is expected to have infinite predictability, i.e., forecasts can be continuously improved by reducing the initial error. Nevertheless, recent studies have shown explicit evidence of the intrinsic predictability limit

of the atmosphere (Judt 2018; Zhang et al. 2019). For example, Zhang et al. (2019) used identical twin experiments performed with convection-permitting global models and indicated that the predictability of synoptic weather in midlatitudes is intrinsically limited. Their results showed that even in a perfect model assumption, the error growth fits Eq. (1.1) well with non-zero β values. Zhang et al. (2019) attributed the non-zero β term to the errors growing upscale from smaller scales, which eventually contaminate the prediction at synoptic scales.

Since the atmosphere is a multiple-scale flow, the error growth due to the processes at smaller scales having energy spectra with a $-5/3$ slope is considered to be the major cause of the predictability limit at synoptic scales. Thus, the error growth behavior among different scales is a key factor in understanding atmospheric predictability and has been investigated by numerous studies. While most previous studies agreed with the existence of an atmospheric predictability limit, consensus on how errors grow at different scales and limit the predictability has not been well established. Studies have been using initial errors at large and small scales to assess how error grows and limits predictability (e.g., Tribbia and Baumhefner 2004; Johnson et al. 2014; Durran and Weyn 2016). Two types of error growth dynamics, up-scale and up-magnitude growth, have been pointed out by different studies. As the representative studies that suggested the up-scale error growth, Zhang et al. (2007) and Judt (2018) showed that errors first grew through moist convection and other mesoscale processes and quickly saturated at the convective scales; the errors then grew with the background baroclinic instability at larger scales. On the other hand, other studies showed that errors could grow at all scales at the same time (i.e., up-magnitude growth) before reaching to a saturation level at smaller scales (Simmons and Hollingsworth 2002; Tribbia and Baumhefner 2004; Mapes et al. 2008; Ngan et al. 2009; Durran and Gingrich 2014).

Both types of error growth aspects cannot completely explain the behavior of the complicated real atmosphere (Nielsen and Schumacher 2016). However, no matter how error

grows at different scales, most studies investigating the error growth associated with different weather phenomena in the atmosphere agree that error grows mainly with the development of moist convection and the accompanying precipitation (Hohenegger et al. 2006; Selz and Craig 2015; Judt 2018; Zhuang et al. 2020). For example, Zhang et al. (2003) performed simulations with a mesoscale model at 3.3 km grid-spacing and showed that the error growth is more rapid in simulations with moist processes included than in dry simulations (Fig. 1.6).

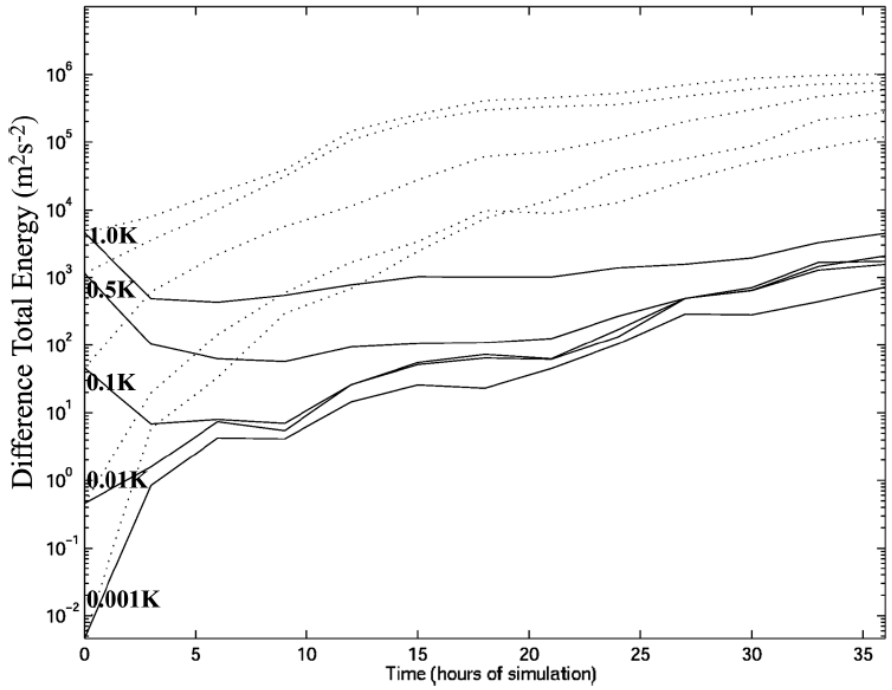

Figure 1.6 Evolution of errors from different initial magnitudes (i.e., 0.001, 0.01, 0.1, 0.5, 1 K) in the experiments with (dotted) and without moist processes (solid) from Zhang et al. (2003, their Fig. 7). © American Meteorological Society. Used with permission.

Moist convective processes, such as buoyancy forcing and latent heating generated by moist dynamical and thermodynamical processes, have been shown to play an important role in building the −5/3 slope of energy spectrum at the mesoscale (Takemi and Rotunno 2003; Bryan et al. 2003; Sun et al. 2017). Sun and Zhang (2016) used the simulation of idealized baroclinic waves and showed that the predicting errors in the dry experiment decrease

continuously by reducing the initial error, implying infinite predictability. In contrast, under the moist environment with strong convective instability, the rapid error growth due to moist convection is less sensitive to the reduction of initial error, which means that the predictable time range cannot be increased by continuously reducing the initial error, implying the intrinsic limit of predictability. In other words, moist processes play a vital role in error growth and thus limit atmospheric predictability.

In summary, the atmospheric predictability is limited, even for the flows at the scales with a -3 slope energy spectrum. This limit is attributed to the error growth associated with moist convection and mesoscale phenomena. Nevertheless, as described above, the atmosphere is a complicated system in which different phenomena could have different predictability limits. Meanwhile, none of our models can perfectly describe the behavior of the real atmosphere. The error growth could differ depending on model configurations such as grid spacing and physics parameterizations (Weny and Durran 2018; Selz 2019). The estimate of the predictability limit may also vary depending on how errors are quantified (Weny and Durran 2019). Our understanding of predictability is limited by both the model and the measurements used to investigate the predictability. Therefore, further studies are still needed, especially for weather phenomena at scales smaller than a synoptic-scale and not directly affected by midlatitude weather systems.

1.3 The predictability of thunderstorms and the purpose of this study

Whether thunderstorms are predictable with NWP models was asked more than 30 years ago (Lilly et al. 1990). Based on the findings of previous studies, thunderstorms are expected to have low predictability because of the natures of faster error saturation at their small characteristic scales (Figs. 1.3 and 1.4) and the more rapid error growth associated with moist

processes (Fig. 1.6).

Besides the difficulty due to the inherent low predictability of thunderstorms, NWP models may also suffer from the insufficient capability to accurately predict the generation and development of convection that results in thunderstorms. For example, in the case of thermally induced thunderstorms over mountainous areas, inadequate resolution of the model can lead to a failure in representing the turbulent motion and thermally driven circulation over mountains (Barthlott et al. 2006; Schmidli et al. 2018). Models could also fail in simulating the exact time of the diurnal cycle of thunderstorms and accompanying rainfall (Janowiak et al. 2007; Dai and Trenberth 2004; Langhans et al. 2013). It was reported that predicting rainfall could be particularly challenging in warm seasons because NWP models cannot accurately represent the processes of deep moist convection (Fritsch and Carbone 2004).

Fortunately, the capability of NWP models is continuously improving with the benefit of the great improvement in computing power. Convection-permitting models (CPMs) have become widely used over the past two decades, improving rainfall predictions (Clark et al. 2016). Meanwhile, CPMs promote various studies to investigate the predictability and error growth associated with moist convection and rainfall (Hohenegger and Schär 2007a, b; Leoncini et al. 2010; Durran and Weyn 2016; Miglietta et al. 2016; Zhuang et al. 2020). Studies focusing on thunderstorms with localized spatial scales have assessed the capability of NWP models for simulating convection and clarified the factors that are important for the successful prediction of thunderstorms (Hanley et al. 2011; Cintineo and Stensrud 2013; Zhang et al. 2015). For example, Hanley et al. (2011) investigated the predictability of an isolated mountain thunderstorm over the Black Forest with ensemble simulations. They showed that the deficiency of the soil and atmospheric moisture represented in the model is responsible for the failure in simulating deep convection. In this way, studies provided insights into improving NWP models to predict thunderstorms better. Despite the increasing attention to the

predictability of thunderstorms in the past decade or so, further investigations are still needed. The followings are some remaining issues.

First, most previous studies on the predictability of thunderstorms focused on the practical perspective. Relatively little was known about the intrinsic limit of predicting thunderstorms. Recent increasing computing power and the improvement of NWP models enable us to conduct further investigations of the predictability at convective scales. The strong flow-dependent predictability at convective scales is a complex problem and deserves more attention to complement the knowledge of atmospheric predictability.

Second, relatively little has been known about the predictability of thermally induced thunderstorms in diurnal cycles. Although some recent studies have investigated the predictability limit of supercell thunderstorms (Lawson 2019; Markowski 2020), most of these studies focused on simulations within three hours or less. Less attention has been devoted to the predictability of thunderstorms during a diurnal cycle. In warm seasons, thermally induced thunderstorms are very common phenomena that impact people's daily lives and are difficult to be predicted with NWP models in operational weather centers. Providing more informative forecasts of thermally induced thunderstorms is challenging but essential for the day-to-day weather forecast in warm seasons. When we try to improve the forecast of thermally induced thunderstorms, understanding where the prediction limits are is also important for developing better strategies for improving NWP. For example, if the benefit of reducing initial errors is limited in deterministic prediction, we need to put more efforts on developing better ensemble perdition systems to tackle the uncertainty of predicting thunderstorms than on improving the accuracy of initial conditions.

Finally, in the previous studies of predictability, only a limited number of previous studies addressed the impact of topography. Recently, Bachmann et al. (2019, 2020) investigated the impact of topography on the predictability of moist convection from a practical perspective.

They evaluated the forecast skill of rainfall with scores at different scales and showed that topography could better the rainfall prediction at a finer scale. However, compared to the importance of topography on affecting convection development that has been reported by numerous studies (refer to the references in Section 1.1), the impacts of topography on predictability remain less understood, especially in the context of error growth dynamics and intrinsic predictability. For example, the mountain shape such as the height and width of a mountain is shown to impact the development of moist convection as well as the amount and distribution of rainfall (Flesch and Reuter 2012; Hassanzadeh et al. 2016; Imamovic et al. 2019; Mulholland et al. 2020). It is required to further examine how such topographic impact on convection development appears in the context of the predictability of thunderstorms.

To address the above concerns, this study investigates the predictability and error growth associated with thermally induced thunderstorms based on a perfect model context. The questions we focus on here are: if an NWP model is initialized in the morning before the convection initiation, how will the initial error grow and destroy the predictability; and how long is the limit of predicting thermally induced thunderstorms and the accompanying rainfall? Special attention is paid to the impact of topography. In addition, since previous studies showed that environmental conditions could impact the predictability of typhoons (Zhang and Tao 2013), mesoscale convective systems (Weyn and Durran 2017), and tornadic supercells (Lawson 2019), we also investigate the impact of different environmental flows on the predictability of thermally induced thunderstorms.

To achieve the above purposes, first we investigate the error growth dynamics associated with thermally induced localized thunderstorms in Chapter 3. A particular focus is paid to the impact of topography. A number of the experimental parameters, such as mountain geometry and background winds, are considered to examine the sensitivity of topographic effects. Understanding error growth dynamics is the first step to investigate the predictability limit.

By analyzing the error growth and topographic effect, we assess the factors that affect the sensitivity of predicting thunderstorms, especially in an earlier time period during convection initiation. The results are also expected to provide some insights into the design of ensemble prediction systems that tackle the uncertainty in NWP.

The nature of error growth dynamics in chaotic systems results in limited predictability. Next, we examine the predictability limit of thermally induced thunderstorms and the accompanying rainfall in Chapter 4. Both the impacts of topography and environmental flow are examined. Here, we aim to address the factors that determine the predictability limit of the localized thunderstorms in a diurnal cycle, which is not well elaborated in previous studies. At the same time, the predictability limit of rainfall is also estimated from the viewpoint of providing better day-to-day weather forecasts that are useful to society.

The structure of the rest of this thesis is as follows. The model configuration and experimental settings are provided in Chapter 2. Chapter 3 presents the results of the simulated thunderstorms and the associated error growth dynamics and discusses the impact of topography. The predictability of thermally induced thunderstorms is shown and discussed in Chapter 4. Chapter 5 concludes the finding of this study.

Chapter 2 Methodology

2.1 Model description

The model used in this study is the Weather Research and Forecasting (WRF) model, which is a mesoscale numerical weather prediction system designed for both atmospheric research and operational forecasting applications. The development of the WRF model began in the latter 1990s by a collaborative partnership of the National Center for Atmospheric Research (NCAR), the National Oceanic and Atmospheric Administration (NOAA), the U.S. Air Force, the Naval Research Laboratory, the University of Oklahoma, and the Federal Aviation Administration (FAA).

Since its first release in 2000, WRF has become one of the most widely used NWP models in the world and has grown to provide a variety of options and capabilities for a wide range of applications (Powers et al. 2017). WRF provides a flexible and computationally efficient platform for operational forecasting, and at the same time reflects the latest developments in physics, numerical values, and data assimilation from the broad research community. It is allowed to generate simulations based on either the real atmospheric data (i.e., observation and analysis data) or idealized conditions. The model serves a wide range of meteorological applications from the large-eddy to global scales and has been proven to perform well in simulating atmospheric convection (Skamarock 2004; Vincent and Lane 2016). It has made meaningful contributions to not only weather forecasting and sciences research but also education and commercial works worldwide.

The WRF system contains two types of dynamic solver, NMM (Non-hydrostatic Mesoscale Model) and Advanced Research WRF (ARW) cores. This study uses version 4.1.2

of the ARW model (Skamarock et al. 2019). ARW offers an extensive menu of options for physical process schemes, such as microphysics, radiative process, boundary layer, and land surface models, for different uses of focus scales and area. It also encompasses numeric/dynamic options, initialization routines, and a data assimilation package (WRFDA) with a variety of data assimilation approaches.

The governing equations adopted in ARW is a set of fully compressible, Eulerian non-hydrostatic solver that conserves dry air mass and scalar mass. The vertical coordinates are η coordinates that follow the terrain; the horizontal grids are Arakawa C-grid staggered grids (Arakawa and Lamb 1977). The time integration uses the second-order or third-order Runge-Kutta method. The prognostic variables in the ARW version 4 include three-dimensional (3D) velocity (u, v, w), perturbation moist potential temperature, perturbation geopotential, and perturbation dry-air surface pressure. Other scalars such as turbulent kinetic energy, mixing ratios of water vapor/hydrometeors, and chemical species are optional forecast variables. For a further introduction of science and algorithmic approaches such as dynamical solver and physics options in the ARW Version 4, please refer to Skamarock et al. (2019).

2.2 Model configuration

This study uses an idealized framework of the ARW model with full physics packages. The computational domain covers a horizontal area of 300 km by 300 km with the depth of 25 km resolved at 1-km horizontal grid spacing and with 50 vertical levels. The lateral boundary condition is doubly periodic (Fig. 2.1). The physics parameterizations used in this study include the WRF Single-moment 6-class (WSM6) scheme (Hong and Lim 2006) for microphysics, Rapid Radiative Transfer Model for General Circulation Models (RRTMG) scheme (Iacono et al. 2008) for long- and short-wave radiation, Mellor-Yamada-Janjic (MYJ) scheme (Janjić 1994) for the planetary boundary layer (PBL) mixing, and Noah Land Surface

Model scheme (Tewari et al. 2004) for the land-surface processes. The 3D Smagorinsky scheme (Lilly 1962; Smagorinsky 1963) is used for turbulent diffusion, and an implicit gravity-wave damping layer is imposed in the upper-5-km layer to avoid wave reflections at the upper boundary. Both planetary boundary layer parameterization and 3D turbulent diffusion are used here to let the PBL scheme cover the solution on the sub-grid scale vertical transport besides the solution from the Smagorinsky scheme (Tompkins and Semie 2017) because the grid spacing of 1 km may not be fine enough to use only the 3D Smagorinsky solution. The cloud and precipitation particles parameterized in the microphysics scheme include cloud water, rain, cloud ice, snow, and graupel. The land use is set to wooden wetland homogeneously.

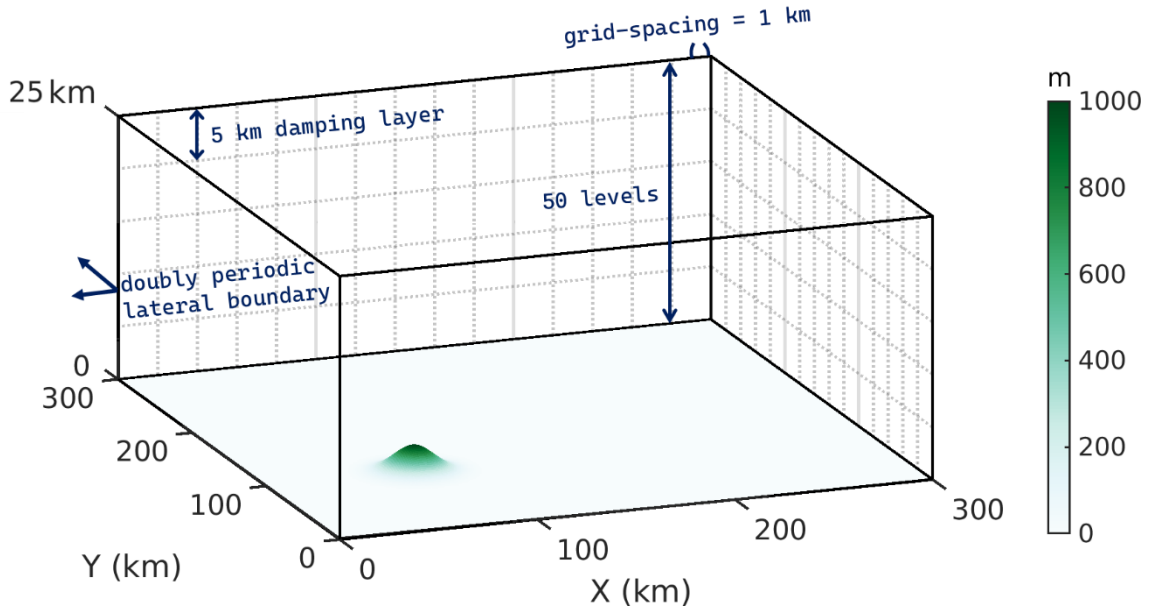

Figure 2.1 The schematic diagram of the domain settings for all experiments and the terrain (color shaded) in experiment TOPO. Note that the length scale of 3-dimensional direction and the terrain height is not shown in realistic ratio for better illustrating.

The diurnal cycle of precipitation over the Kii Peninsula in summer is pronounced (Takemi and Tsuchida 2014), and therefore is considered to be a suitable choice to determine the mountain and environmental conditions in the present numerical experiments. For the

initial vertical profile, a sounding observation at the Shionomisaki station, located at the Kii Peninsula, Wakayama, Japan, at 0900 Japan Standard Time (JST or UTC+9) on 19 August 2019 (Fig. 2.2) is homogeneously extended horizontally. The Coriolis parameter is set constant with a value of $7.9958 \times 10^{-5}\ \mathrm{s}^{-1}$ which corresponds to the value at the latitude of the Shionomisaki station (33.35°N). The vertical sounding observation to initialize simulations is chosen arbitrarily from a summer day, on which afternoon rainfall is observed at Shionomisaki (Fig. 2.3). The vertical profile provides a relatively less stable condition with almost zero convective inhibition (CIN) and convective available potential energy (CAPE) about 1617 $\mathrm{J\ kg}^{-1}$; the height of lifted condensation level (LCL) is almost the same as the level of free convection (LFC; refer to the black dashed curve in Fig. 2.2). Thus, the development of deep convection is relatively easy as long as there is an updraft triggered by other factors. The wind is northeasterly with a speed of around $3\ \mathrm{m\ s}^{-1}$ near the surface and turns to southwesterly above 850-hPa height (Fig. 2.2, also refer to Fig. 2.5a), resulting in strong wind shear (see Fig. 2.5c) in wind direction over the boundary layer.

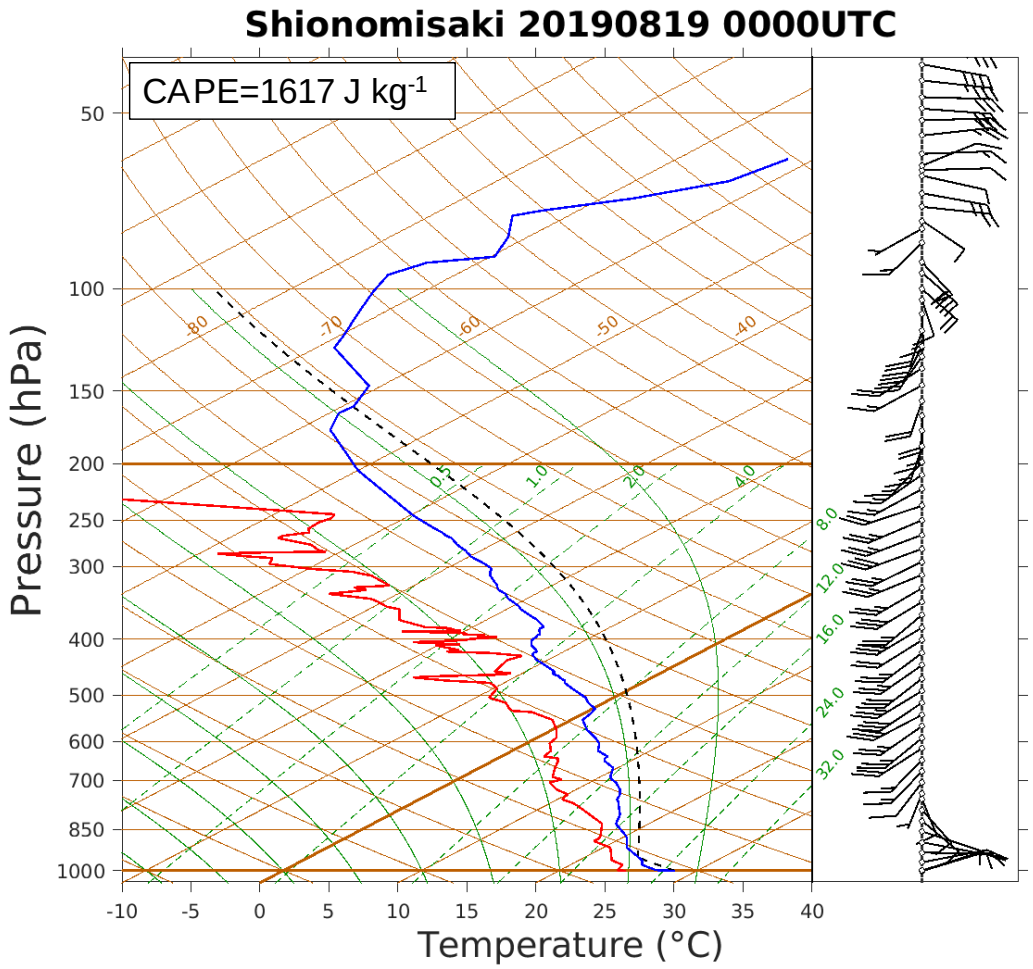

Figure 2.2 The Skew-T Log-P Diagram of the sounding data from the station at Shionomisaki, Wakayama, Japan at 0900 JST (0000 UCT) on 19 August 2019. The blue and red curves show the profile of temperature and dew point temperature, respectively. The wind barbs on the right show the profile of wind direction and speed (each short barb represents 5 knots). The dashed black curve depicts the route for a parcel adiabatic ascending from the surface.

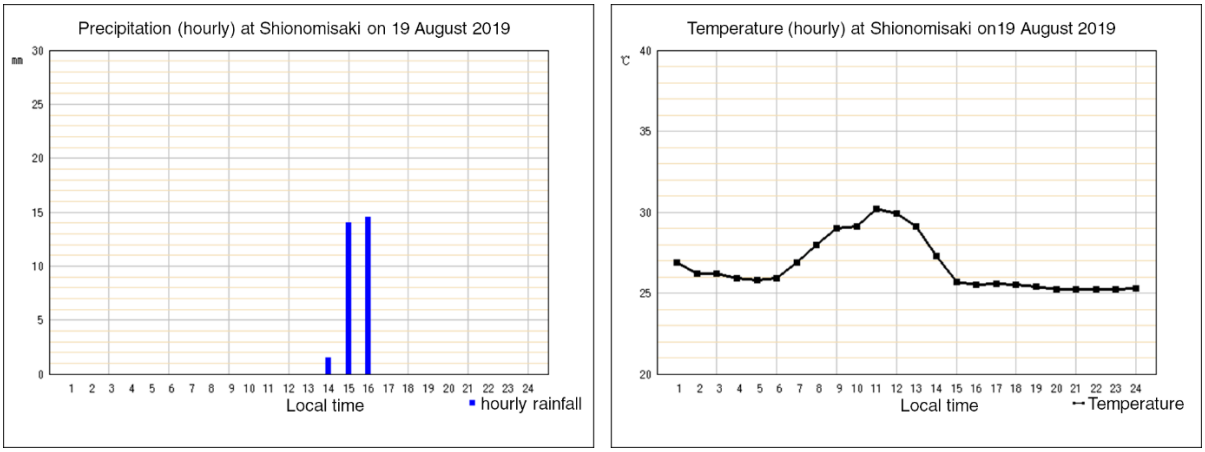

Figure 2.3 The rainfall (left) and temperature (right) observation at Shionomisaki station on 19 August 2019. Modified from the figures retrieved from the website of Japan Meteorological Agency: https://www.data.jma.go.jp/obd/stats/etrn/view/hourly_s1.php?prec_no=65&block_no=47778&year=2019&month=08&day=19&view=g_pre for the left panel, and https://www.data.jma.go.jp/obd/stats/etrn/view/hourly_s1.php?prec_no=65&block_no=47778&year=2019&month=08&day=19&view=g_tem for the right panel.

2.3 Simulation strategy and experimental settings

To investigate error growth dynamics, we conducted identical twin experiments similar to the approaches used in previous studies such as Zhang et al. (2003) and Judt (2018). Each identical twin experiment contains two simulations, control and perturbed, whose differences are regarded as errors and used for examining the error growth dynamics as well as predictability. For each experiment, the control simulation is initialized at 0000 local time (hereafter denoted as LT) 22 June, the summer solstice, by adding white noise of the potential temperature (θ) below 2 km with an amplitude of 0.01 K to the horizontally homogeneous initial condition given by the vertical profile of the sounding data. At 0600 LT 23 June, after 30-h spin-up, the perturbed simulation in each experiment is produced by adding random perturbations from a Gaussian distribution with zero-mean and standard deviation equal to 0.01 $\mathrm{g\,kg^{-1}}$ to the water vapor mixing ratio of the control simulation at every grid. This start time of perturbed simulations is set to before the initiation of thermally induced moist

convection in the morning to imitate the situation of predicting thunderstorms before their generation. For some experiments, additional sensitivity tests are also performed with different start times and initial perturbation amplitude of the perturbed simulations, and the results are discussed in Chapter 4 (see also the last column of Table 2.1).

To assess the impact of topography and environmental flow conditions on error growth and predictability, a number of experiments with different topography settings or background winds are performed (Table 2.1). A group of experiments is performed with the original wind profile of the sounding data. It contains an experiment without topography (hereafter referred to as FLAT) and several experiments with mountain topography of different geometry (see Table 2.1). Among the experiments with mountain topography, in the one that mainly used to compare with FLAT, a Gaussian-shaped mountain with a peak height near 1000 m (exactly 993.1268 m) and about 50-km width is embedded to the southwestern quadrant of the domain (centered at x=75 and y=100; refer to Fig. 2.1 and grey-dashed contours in Fig. 3.2). This experiment is hereafter referred to as TOPO.

The choice of the mountain size and height is based on the actual topography size in the real world. For example, the Kii Peninsula has an *O*(100 km) size and the overall elevation of around 1000 m. For an example of mountains outside Japan, Mount Datun in northern Taiwan, which was indicated to play an important role in the development of afternoon thunderstorms and the accompanying rainfall amount (Fig. 2.4; Kuo and Wu 2019), has a size and height of around 25 km and 1000 m, respectively. Other experiments with different mountain geometry were also conducted (Table 2.1). The experiment with the halved mountain height compared to the one in TOPO is hereafter called H500. The experiments having the halved- and doubled-volume of the mountain compared to TOPO are referred to as V05 and V20, respectively. Previous studies have shown the impact of mountain geometry on moist convection development and accompanying rainfall (Imamovic et al. 2019; Mulholland et al. 2020). Here

we will further investigate its impact on error growth and predictability. Please refer to Table 2.1 for the settings of other experiments.

Besides, other groups of experiments were conducted by replacing the vertical wind profile in the initial condition with idealized wind profiles with different wind speeds and vertical wind shear (Fig. 2.5) to investigate the impact of environmental flow. Among them, U00 represents the experiments initialized with zero wind for examining the conditions of no background wind; NS5 are the experiments with the westerly wind whose speed is 5 $\mathrm{m\,s^{-1}}$ uniformly in the vertical direction, representing the condition of no vertical wind shear; U25 are the experiments also using westerly wind with strong vertical wind speed shear and weak near-surface wind. The U25 wind profile is generated by Eq. (4) in Weisman and Klemp (1982) by using the same z_s equal to 3 km as in Weisman and Klemp (1982) and U_s equal to 25 $\mathrm{m\,s^{-1}}$. For each group of different background wind, experiments with and without mountain topography are also conducted (see Table 2.1 for the details). The mountains in these experiments are located within the western part of the domain (centered at x=50 and y=150; refer to grey-dashed contours in Figs. 3.4d–f) for adapting the westerly wind, differing from those experiments with the original sounding wind profile which have mountains located in the southwest quadrant of the domain. For each experiment, its control simulation is initialized from the temperature profile of the sounding data and their own wind profiles with their own topography settings, and the perturbed simulation is conducted by adding small perturbations to this control simulation as described previously. A brief view of the simulated thunderstorms in these experiments is presented in Chapter 3.

Table 2.1 The list of all experiments in this study and their background wind and topography settings. The last column shows the sensitivity tests that were conducted with the conditions of topography and flows of that experiment.

Wind profile (see Fig. 2.5)	**Experiment name**	**Mountain height**	**Mountain Volume**	**Sensitivity tests**
Sounding data	**FLAT**	None		noMP (Fig. 3.15); THM (Fig. 3.16); P01, P10, 08LT, 10LT (Figs. 4.1&4.2)
	V05	1000 m	0.5	
	TOPO		1	noMP (Fig. 3.15); THM (Fig. 3.16); P01, P10, 08LT, 10LT (Figs. 4.1&4.2)
	V20		2	
	H500_V05	500 m	0.5	
	H500		1	noMP (Fig. 3.15); THM (Fig. 3.16); P01 (Fig. 4.2)
	H500_V20		2	
	H750_V05	750 m	0.5	
	H750		1	
	H750_V20		2	
	H2000_V05	2000 m	0.5	
	H2000		1	
	H2000_V20		2	
U00: no background wind	**U00_FLAT**	None		P01 (Fig. 4.2)
	U00_V05	1000 m	0.5	
	U00_TOPO		1	
	U00_V20		2	
NS5: Constant wind = 5 $m\ s^{-1}$	**NS5_FLAT**	None		
	NS5_V05	1000 m	0.5	
	NS5_TOPO		1	
	NS5_V20		2	
U25: Westerly wind from 0 over the surface to 25 $m\ s^{-1}$ over mid-troposphere	**U25_FLAT**	None		P01 (Fig. 4.2)
	U25_V05	1000 m	0.5	
	U25_TOPO		1	
	U25_V20		2	

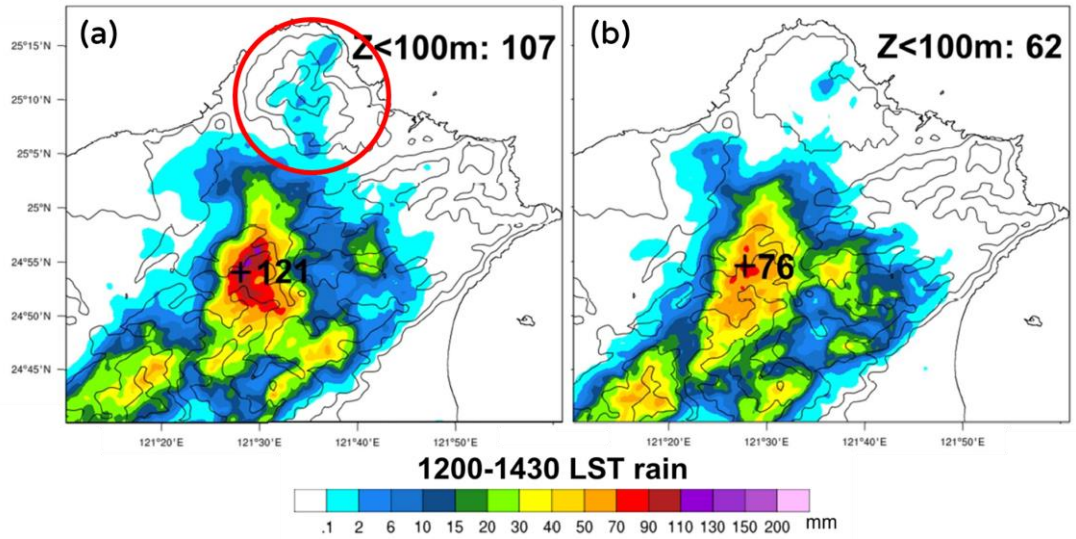

Figure 2.4 The results from Miao and Yang (2020), showing that the existence of Mount Datun (indicated by the red circle) affects the amount of afternoon rainfall over Taipei Basin from the maximum of 121 mm in the control simulation (left) to 76 mm in the simulation removing Mount Datun (right). Modified from Miao and Yang (2020, their Figs. 17a, d). Copyright 2020 Meteorological Society of Japan.

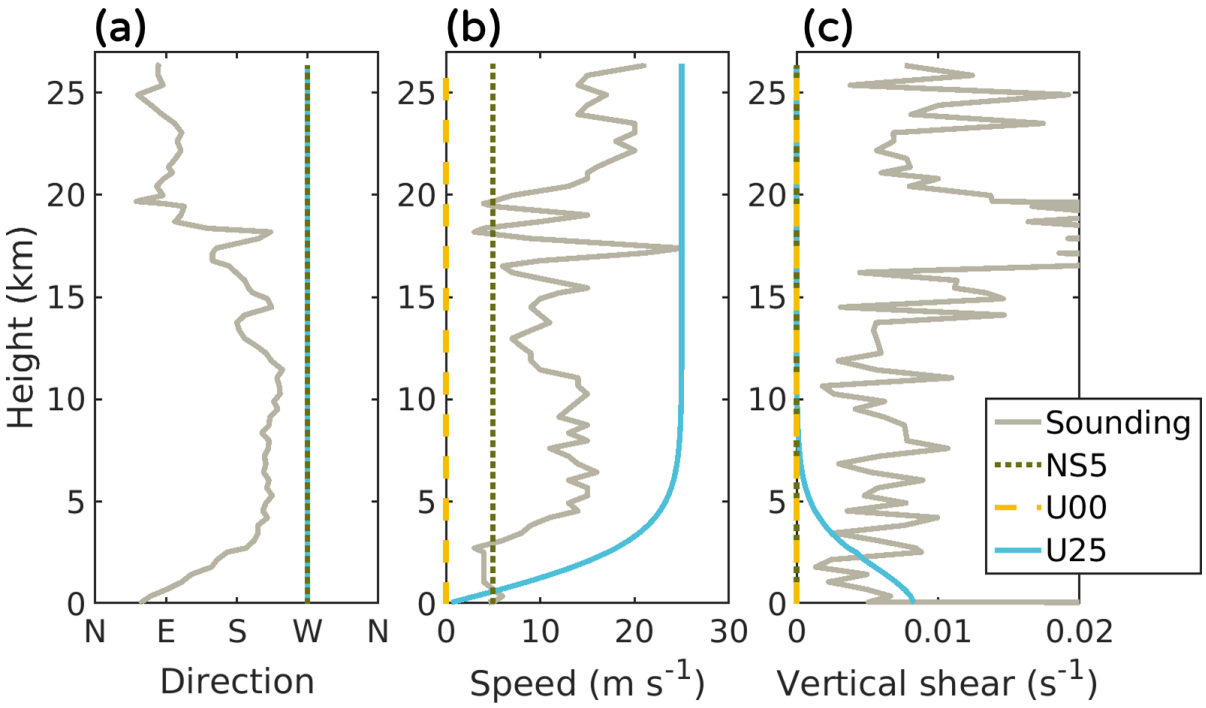

Figure 2.5 The vertical profile of (a) wind direction, (b) wind speed, and (c) vertical wind shear from the sounding observation data and the idealized ones (NS5, U00, and U25) used in this study. The U00 one has zero wind throughout all levels, so it is not shown in (a).

2.4 Analysis metrics

2.4.1 Convective moist different total energy (CMDTE)

To estimate the differences between the control and perturbed simulations, this study proposes a metric similar to the difference total energy (DTE) used in previous studies (e.g., Zhang et al. 2003; Selz and Craig 2015), but incorporating differences in water vapor and vertical velocity. We refer it to as convective moist difference total energy (CMDTE), which is calculated following the equation of moist total energy norm in Ehrendorfer et al. (1999) but including the differences in the vertical velocity as follows:

$$\mathrm{CMDTE} = \frac{1}{2}\left[u'^2 + v'^2 + w'^2 + \frac{c_p}{T_r}T'^2 + \frac{L_v^2}{c_p T_r}q_v{}'^2 + RT_r\left(\frac{p_s'}{P_r}\right)^2\right]. \quad (2.1)$$

The difference in the vertical wind is involved to better estimate the difference of the moist convective cores between the two simulations since vertical motion is one of the main characteristics of strong non-hydrostatic phenomena like moist convection. Here, u', v', w', T', and $q_v{}'$ are the differences of east-west wind, south-north wind, vertical velocity, temperature, and water vapor mixing ratio, respectively, between the two simulations at 3-dimensional grids; p_s' is the difference of surface pressure between the two simulations. T_r and P_r are the reference temperature (270 K) and reference pressure (1000 hPa), respectively, following the value used in Ehrendorfer et al. (1999); c_p, L_v, and R are the specific heat capacity at constant pressure (1004.9 J $\mathrm{kg^{-1}K^{-1}}$), the latent heat of condensation (2.4359×10^6 J $\mathrm{kg^{-1}}$), and the specific gas constant of dry air (287.04 J $\mathrm{kg^{-1}K^{-1}}$), respectively.

Besides CMDTE, the terms in Eq. (2.1) of the difference in the 3D wind (u', v', and w'), temperature (T'), and moisture ($q_v{}'$) are also calculated separately, denoted by DiKE, DiSH, and DiLH, respectively. They are used to assess the error growth in the context of kinetic energy, sensible heat, and latent heat, respectively. In Eq. (2.1), the differences in

surface pressure are two to three orders smaller than the other three terms, thus it is neglected and not examined separately here.

To investigate the error growth dynamics from different aspects, CMDTE is compared in terms of several forms, such as the horizontal distribution or power spectra. For the horizontal distribution, we take the vertical mass-weighted average of CMDTE following Eq. (2) in Nielsen and Schumacher (2016).

For the horizontal wavenumber spectra of CMDTE, a procedure similar to the kinetic energy spectra used in Weyn and Durran (2017) is adopted. First, the two-dimensional discrete Fourier transform of u', v', w', T' $q_v{}'$, and $p_s{}'$ are calculated for each model level at a given time. For a given time and a model level, the two-dimensional discrete Fourier transform of u' and its complex conjugate will be denoted as $\widehat{u'}$ and $\widehat{u'}^*$, respectively; and so do other variables. Then the two-dimensional spectra of CMDTE are calculated by

$$\widehat{CMDTE}_{lev}(k_x, k_y) = \left[\widehat{u'}\widehat{u'}^* + \widehat{v'}\widehat{v'}^* + \widehat{w'}\widehat{w'}^* + \frac{c_p}{T_r}\widehat{T'}\widehat{T'}^* + \frac{L_v^2}{c_p T_r}\widehat{q_v{}'}\widehat{q_v{}'}^* + \frac{RT_r}{P_r^2}\widehat{p_s{}'}\widehat{p_s{}'}^*\right]/n_x n_y. \quad (2.2)$$

Here, $\widehat{CMDTE}_{lev}(k_x, k_y)$ is the two-dimensional spectra of CMDTE at a model level denoted by *lev*; k_x and k_y are the wavenumbers, and n_x and n_y are the number of grid points in the x- and y-direction, respectively. Then the vertical mean of $\widehat{CMDTE}_{lev}(k_x, k_y)$ below level 33 (~10 km) is taken, denoted by $\widehat{CMDTE}(k_x, k_y)$. Finally, the one-dimensional spectra $\widehat{CMDTE}(k_h)$ is computed by adding $\widehat{CMDTE}(k_x, k_y)$, whose wavenumber meets the condition that $k_h - \frac{1}{2} < \sqrt{k_x^2 + k_y^2} \leq k_h + \frac{1}{2}$, to the bin of $\widehat{CMDTE}(k_h)$. Here, k_h is the one-dimensional wavenumber that will be depicted in the bottom x-axis of the figures presenting the results in the spectra space (Figs. 3.7 and 3.12).

For calculating the spectra of the different terms in the CMDTE (Fig. 3.12), the above procedure is taken separately for different terms in Eq. (2.1), representing the error of different

variables. The power spectra of the control simulation (solid dark red curve in Fig. 3.7) are also calculated by the same procedure but replacing the differences between the two simulations (e.g., u', v', w', etc.) with the model variables themselves from the control simulation.

In Chapter 4, the error growth rate λ is also defined by the growth in the magnitude of domain-averaged CMDTE in a 30-minute interval, which is represented by the exponent of natural logarithm *e* as:

$$CMDTE_{t+30} = e^{\lambda} CMDTE_t \qquad (2.3a)$$

$$\text{or, } \lambda = ln(\frac{CMDTE_{t+30}}{CMDTE_t}). \qquad (2.3b)$$

Here, subscript *t* represents the time. If $\lambda = 1$, it means the error become *e* times after 30 minutes; when $\lambda = 0$, it means the error remains the same after 30 minutes.

2.4.2 Spatial correlation coefficient (SCC)

In Chapter 4, the predictability limit of rainfall distribution is estimated by the spatial correlation coefficient (SCC) of the rainfall between control and perturbed simulation, which is calculated by

$$\text{SCC} = \frac{\sum_{i=1}^{N}(Cntl_i - \overline{Cntl})(Pert_i - \overline{Pert})}{\sqrt{\sum_{i=1}^{N}(Cntl_i - \overline{Cntl})^2 \sum_{i=1}^{N}(Pert_i - \overline{Pert})^2}} \qquad (2.4).$$

Here, N is the grid number of the whole domain; *Cntl* and *Pert* represent the rainfall value of control and perturbed simulations, respectively; *i* is the index of model grids; the overbar means the domain average. The higher SCC value indicates that the rainfall distribution between the two simulations is more similar.

For estimating the accuracy of rainfall prediction at different scales, the SCC is also calculated for the rainfall distribution whose small-scale characteristics are filtered. Here, a

low-pass filter, which filters the variation of spatial characteristic with wavelength lower than a specific value, is performed to the rainfall in both the control and perturbed simulations. In more detail, the two-dimensional discrete Fourier transform of rainfall is calculated. Then the results with wavenumbers larger than a specific threshold are replaced by zero in the wavenumber space to discard the small-scale pattern. At last, the inverse discrete Fourier transform is calculated again to get the results back to horizontal spatial space. After applying the low-pass filter, the SCC is calculated with the filtered rainfall distribution, i.e., the results from the low-pass filter are used for *cntl* and *pert* in Eq. (2.4). By calculating the SCC of rainfall after applying a low-pass filter at 100 km, for example, the similarity of the rainfall pattern between the control and perturbed simulation at the scale of 100 km can be compared.

2.4.3 Definition of cloud grid

Because the evolution of moist convection among the experiments is different (see Section 3.1 for detail) and the error growth is highly dominated by the convection development (see Section 3.2), a term that helps represent the degree of moist convection development is defined and used as a reference when comparing the error in different experiments. Here, we identify the cloud grid over a horizontal plane to represent the existence of convective clouds in a vertical column in numerical simulations. The cloud grid is defined as the grids having vertically integrated hydrometeor contents larger than 0.7 $\mathrm{kg\,m^{-2}}$ in the control simulation of each experiment. This threshold corresponds to the rain rate of about 0.1 $\mathrm{mm\,h^{-1}}$, representing the grids with deep moist convection able to produce rainfall. The continuous cloud grids is then regarded as the area possessed by one convective cloud and used for comparing the error growth associated with moist convection. In addition, the cloud grid ratio (CGR) is further defined by the ratio of the number of identified cloud grids to all grids in a certain domain in the control simulation, representing the coverage of convective clouds, and is used to quantify the degree of convective activity.

2.4.4 Simulated reflectivity

In Section 3.1, the simulated vertical maximum reflectivity is presented to show the development of convective clouds. The simulated reflectivity (Z_{dB}) is calculated at each model grid based on the method described in Dowell et al. (2011). First, following the Eq. (A.4)-(A.7) in the Appendix of Dowell et al. (2011) and using the intercept parameter of the exponential drop size distribution in the WSM6 microphysics scheme, the equivalent reflectivity factor (Z_e) is calculated at each model grid as follows:

$$Z_e = 3.63 \times 10^9(\rho_a q_r)^{1.75} + 1.18 \times 10^9(\rho_a q_g)^{1.75} + 1.33 \times 10^9(\rho_a q_s)^{1.75},$$

when $T \leq 0℃$; (2.5a)

$$Z_e = 3.63 \times 10^9(\rho_a q_r)^{1.75} + 1.18 \times 10^9(\rho_a q_g)^{1.75} + 5.77 \times 10^{11}(\rho_a q_s)^{1.75},$$

when $T > 0℃$. (2.5b)

Here, q_r, q_g, and q_s are the mixing ratios of rainwater, graupel, and snow, respectively; ρ_a and T are the air density ($kg\ m^{-3}$) and temperature, respectively. The reflectivity Z_{dB} at each grid is then computed by $Z_{dB} \equiv 10log_{10}(Z_e)$ as described by Eq. (A.8) in Dowell et al. (2011). Finally, the vertical maximum reflectivity, showing the horizontal distribution of convective clouds, is generated by finding the vertically maximum value of Z_{dB} at each column of model grids.

Chapter 3 Topographic effects on the error growth dynamics and convection initiation

In this chapter, we focus on the error growth dynamics associated with thermally induced localized thunderstorms, including how initial errors grow with the development of moist convection, and how mountain topography affects this error growth. Section 3.1 first provides a brief view of simulated thunderstorms with different topography and background winds. Then, the error growth dynamics associated with moist convection is investigated using the convective moist difference total energy (CMDTE; see Section 2.4.1), based on the results of FLAT and TOPO. Next, in Section 3.2, we examine the topographic effects on the rapid error growth triggered by the initiation of moist convection by using different mountain geometry. Section 3.3 first presents the sensitivity of the topographic effects to different background winds. Then we further examine the sensitivity by (1) turning off the microphysics scheme and (2) adding initial errors on potential temperature. The former assesses the error growth and topographic effects under the situation without moist processes; the latter evaluates the sensitivity to the initial uncertainty on different model state variables. In Section 3.4, we discuss the possible reason for the sensitivity of topographic effects to mountain geometry and background winds. The summary of this chapter is presented in Section 3.5.

3.1 Simulated thunderstorms and the associated error growth dynamics

3.1.1 Simulated thunderstorms in diurnal cycles

Figure 3.1 shows the time series of domain averaged surface-air temperature and hourly rainfall of control simulations in the experiments with different topography and background winds. Clear diurnal cycles are produced in all experiments regardless of the topography and flow conditions. For surface-air temperature among the experiments with different background winds, the time of the peak values is slightly different on the second day (23 June), while those among the experiments with different topography are less different (c.f. Figs. 3.1a, b). For the rainfall among the experiments with mountain topography (Figs. 3.1c, d), there is a little shock during 0300–0900 LT on the first day (22 June) after the simulations are initialized from the random perturbation added to horizontally homogenous fields. To avoid this spin-up issue, the twin experiments are conducted from the second day. On the second day, all experiments produced a diurnal cycle of the rainfall, while the start time in the morning, peak values at noon, and the rainfall intensity in the afternoon are slightly different among the experiments.

To look at the development of simulated thunderstorms in more detail, Fig. 3.2 depicts the simulated vertical maximum reflectivity (Dowell et al. 2011; see also Section 2.4.4) on the second day of the control and perturbed simulations in FLAT and TOPO, representing the development of convective clouds without and with mountain topography, respectively. The diurnal cycle is also seen in the development of moist convection: the convective clouds are more vigorous at noon and dissipate in the evening. This diurnal cycle of convection development is shown in both FLAT and TOPO. Nevertheless, the spatial distribution and the start time of moist convection are different. The convective clouds in TOPO first appear around the mountain in the morning and organize to a larger size at noon (Figs. 3.2g-i). In comparison, the convective clouds in FLAT occur later and develop everywhere equally over the whole domain (Figs. 3.2b-d). The different spatial evolution of convective clouds results in different distributions of rainfall in FLAT and TOPO (Fig. 3.3). In FLAT, the rainfall

distributes equally over the whole domain no matter in the morning or afternoon (Figs. 3.3b, c). In comparison, the rainfall in TOPO concentrates near the mountain in the morning while distributing dispersedly outside the mountain area in the afternoon (Figs. 3.3e, f). A wide continuous area of rainfall larger than 20 mm $(6\text{h})^{-1}$ is shown near the mountain. Other experiments that have different mountain geometry (H500, V05, and V20) also produced convective clouds and rainfall near the mountain similarly to TOPO, while the initiation time or sizes of the clouds are varied among the experiments (refer to Figs. 3.8 and 4.4).

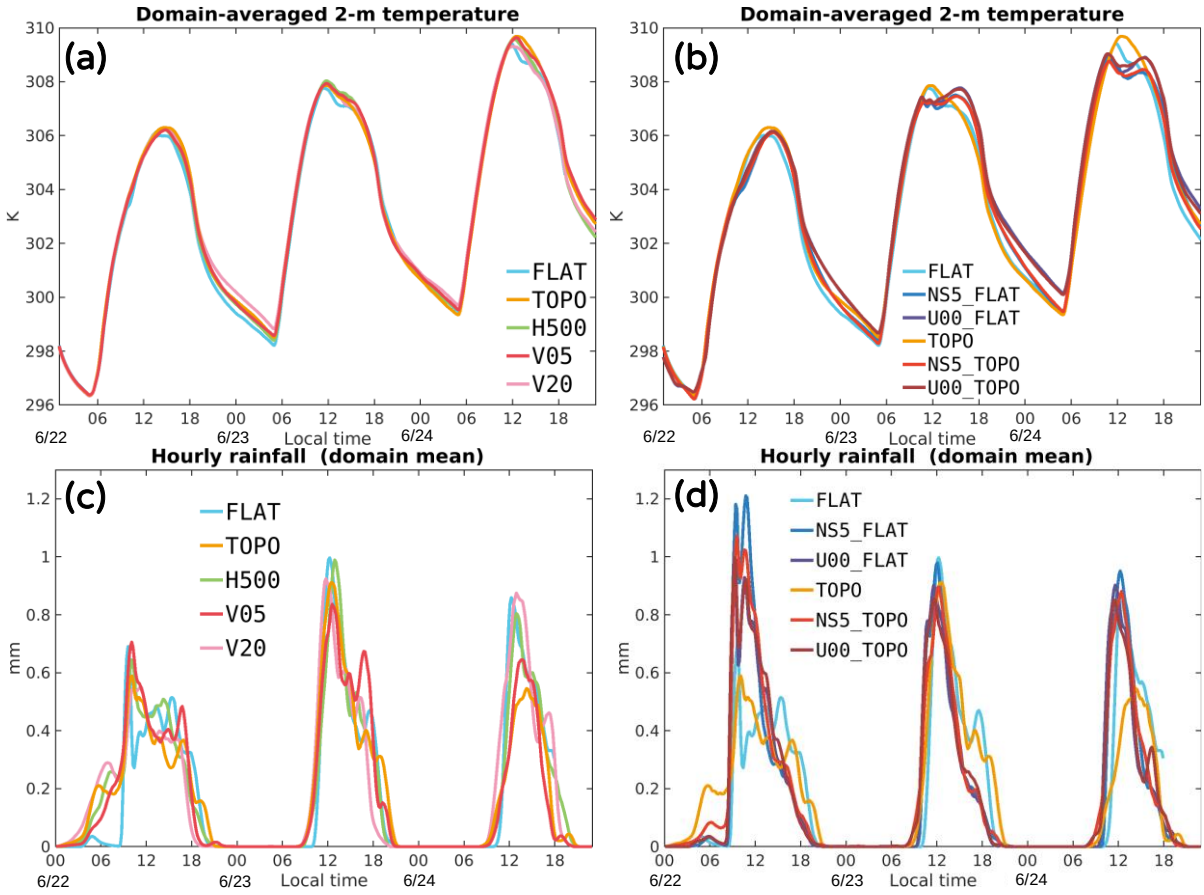

Figure 3.1 The domain averaged (a), (b) surface-air (2-m height) temperature and (c), (d) hourly rainfall from 22 to 24 June of the control simulation in the experiments with (a), (c) different topography and (b), (d) different background winds.

For the experiments with replaced initial wind profiles, the characteristic of convective clouds is different among the experiments with different background winds (Fig. 3.4). For the experiments without mountain topography, U00_FLAT and NS5_FLAT have less organized convective clouds than U25_FLAT; for the experiments with mountain topography, U00_TOPO and NS5_TOPO possess organized convective clouds in the morning over and downstream of the mountain, respectively (upper panel of Figs. 3.4d, e), while U25_TOPO has large, organized clouds over the northern part of the domain, and smaller ones downstream of the mountain.

In general, all experiments successfully simulated thermally induced localized thunderstorms characterized by diurnal cycles despite the various spatial distribution and the different times of convection initiation among the experiments with different topography and background winds. In the following, we use the CMDTE between the control and perturbed simulations of FLAT and TOPO to present the error growth dynamics associated with moist convection development. The topographic effects on the error growth will be examined in Section 3.2.

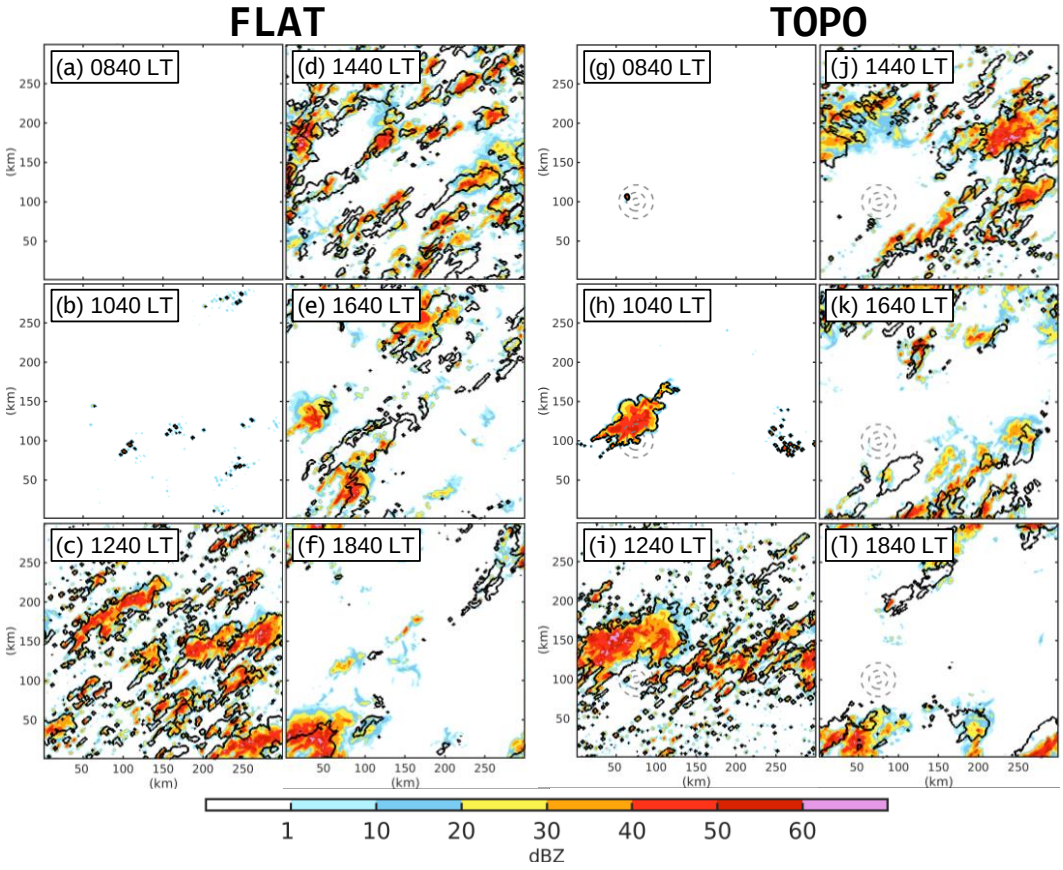

Figure 3.2 The vertical maximum reflectivity calculated from the control simulation (color shaded) and the perturbed simulation (black contour; 20 dBZ) of (a)-(f) FLAT and (g)-(l) TOPO on 23 June. The gray dashed contours in (g)-(l) represent the topography height equal to 100, 500, and 900 m, respectively, from the outside to the inside.

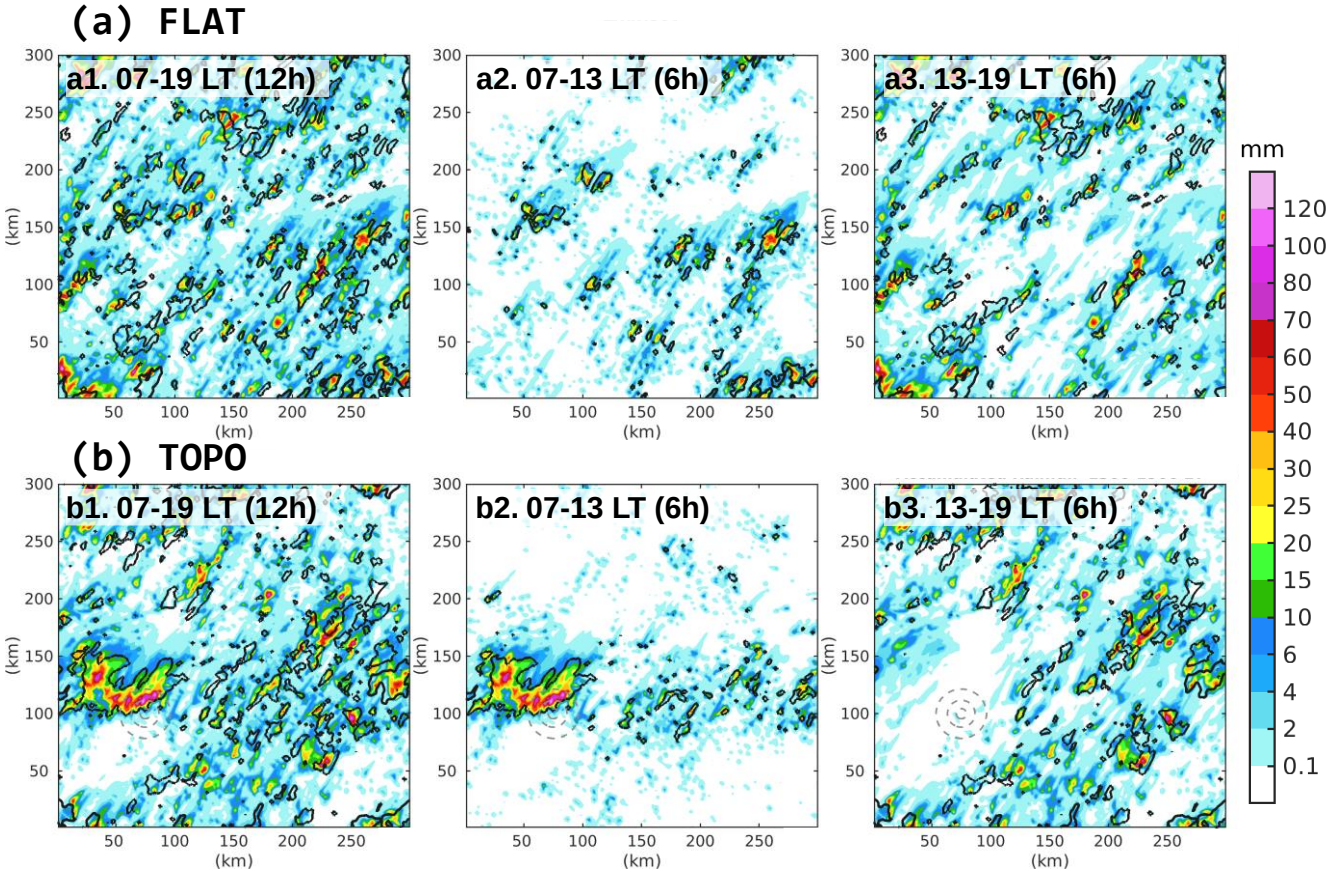

Figure 3.3 The accumulated rainfall during 0700-1900 LT (left), 0700-1300 LT (middle), and 1300-1900 LT (right) in the control simulation (color shaded) and the perturbed simulation (black contours; 10 mm) in (a) FLAT and (b) TOPO on 23 June.

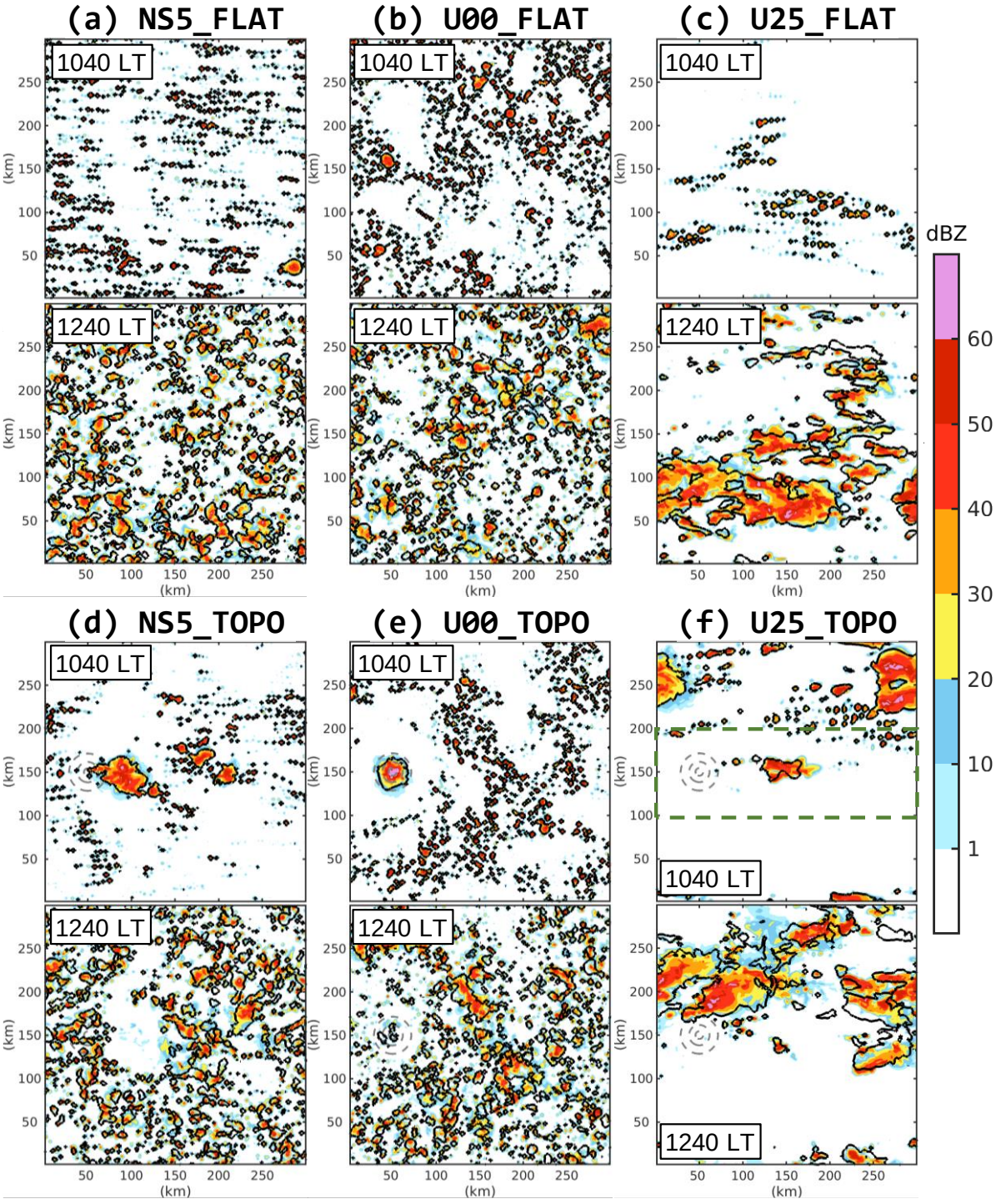

Figure 3.4 The vertical maximum reflectivity calculated from the control simulation (color shaded) and the perturbed simulation (black contour; 20 dBZ) of (a) NS5_FLAT, (b) U00_FLAT, (c) U25_FLAT, (d) NS5_TOPO, (e) U00_TOPO, and (f) U25_TOPO at 1040 and 1240 LT.

3.1.2 Error growth dynamics associated with moist convection

Figure 3.5 provides the horizontal distribution of errors in FLAT and TOPO, depicted by the vertically mass-weighted averaged CMDTE. The vertically integrated hydrometeor contents are also depicted to show the distribution of convective clouds. The error magnitude generally increases with time as convection develops. In particular, for both experiments, the horizontal distribution of the error roughly coincides with the position of convective clouds at different times, indicating that the error growth is highly related to the moist convective processes, which is also indicated in previous studies (e.g., Zhang et al. 2003).

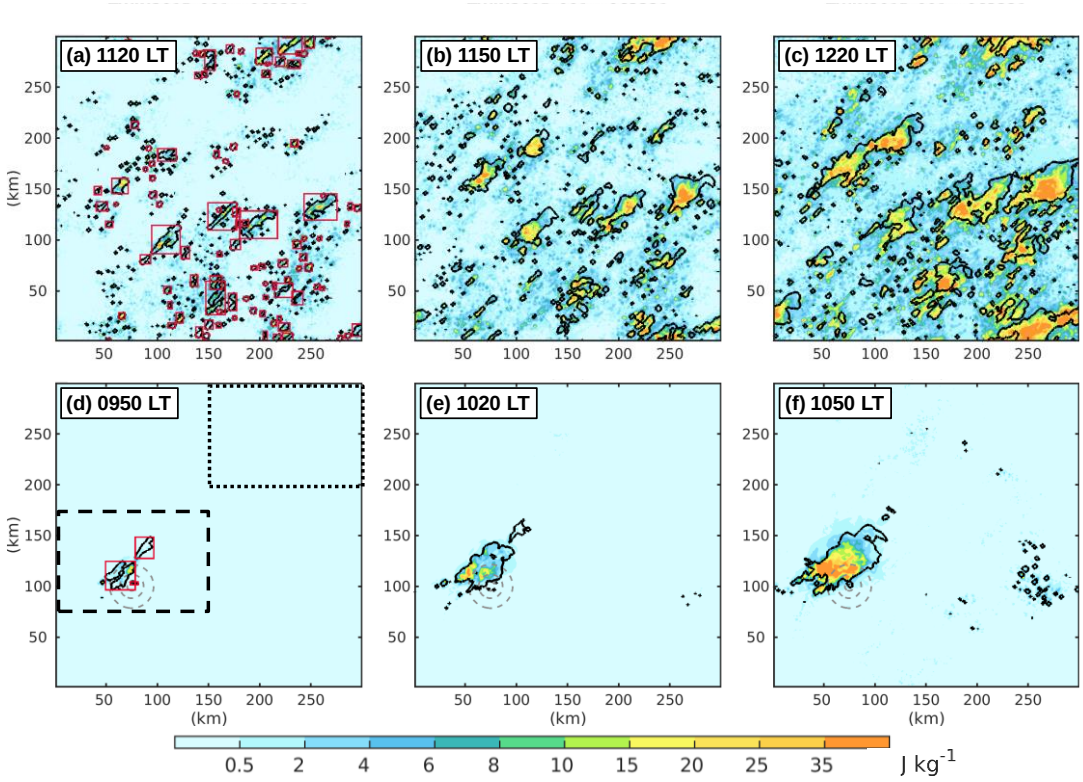

Figure 3.5 The vertical mass-weighted averaged CMDTE (color shaded) of (a)-(c) FLAT and (d)-(e) TOPO. The black contours depict the vertically integrated hydrometeor contents in the control simulation (0.7 $kg\,m^{-2}$, i.e., the defined cloud grids). The dashed-line and dotted-line boxes in (d) show the range of mountain and plain area, respectively, used for computing sub-domain average in Fig. 3.6. The red boxes in (a) and (d) illustrate the detected cloud areas used for producing Fig. 3.9.

The domination of moist convection on the error growth is also shown in the time series of CMDTE. Figure 3.6 shows the temporal evolution of the CMDTE in FLAT and TOPO over the whole domain and two sub-domains with the same size over the mountain and plain areas (depicted in Fig. 3.5d). The domain-averaged cloud grid ratio (CGR) is also presented in Fig. 3.6 to show the evolution of convective activity. The mountain area is chosen to cover the convection developing over the mountain (Figs. 3.2g-i), and the plain area represents an area away from the mountain. The whole-domain averaged errors after 1200 LT are similar FLAT and TOPO, suggesting that the two experiments result in similar total error over the whole computational domain in the afternoon. The difference in the whole-domain-averaged error evolution between TOPO and FLAT is shown from 0900 to 1200 LT because of different convection development caused by mountain topography. This is clearly seen in the error evolution over the two sub-domains.

In FLAT, the error growth is similar between the two sub-domains and the whole domain because the convective clouds have a fair chance to develop anywhere in the whole domain without the forcing of topography. The even distribution of the convection in FLAT can be seen from the very similar CGR evolutions among the three calculating domains (blue curves in the upper panel of Fig. 3.6). In contrast, the errors in TOPO are very different over the two sub-domains. For the mountain area, because the convective clouds in TOPO developed here first (Figs. 3.2g-i), the exponential error growth also starts early, corresponding to the start time of convective clouds depicted by the CGR (dashed-orange curve in the upper panel of Fig. 3.6). For the plain area in TOPO (dotted-orange curves in Fig. 3.6), the error starts the exponential growth at a later time, reflecting the late onset of the convection development over this area (Figs. 3.2h, i); the onset of rapid error growth also coincides with the CGR. The results of TOPO in Fig. 3.6 suggest that the mountain causes the various temporal and spatial evolutions of convective clouds, further resulting in the different error evolutions between the

mountain and plain areas in TOPO or between FLAT and TOPO. Similar to Fig. 3.5, Fig 3.6 again demonstrates that the error growth dynamics is closely related to the development of moist convection.

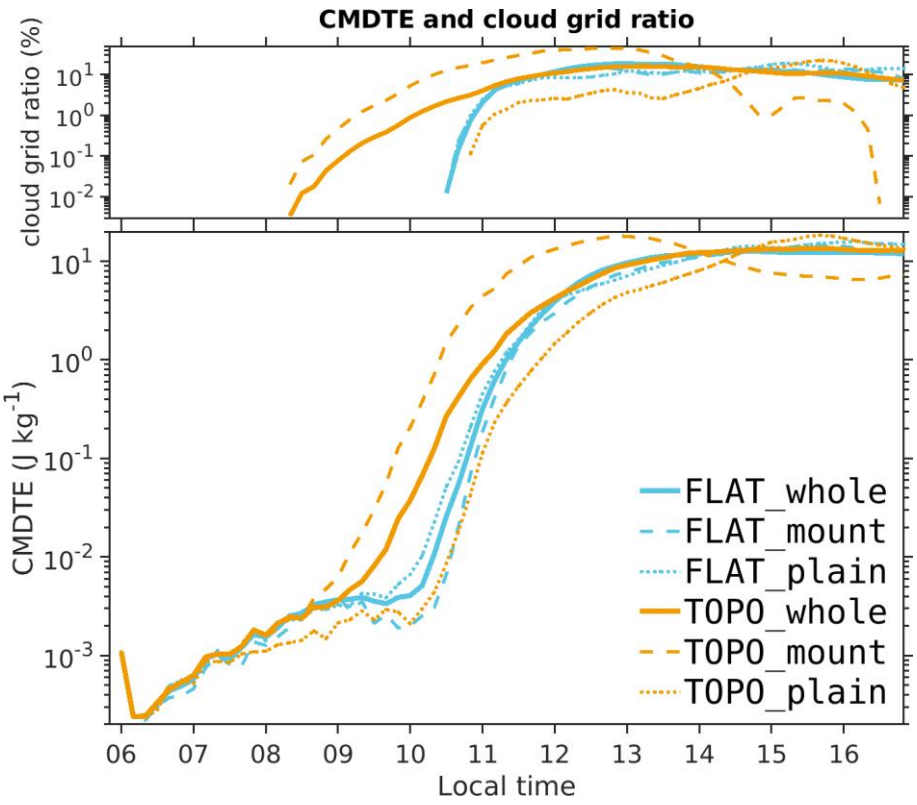

Figure 3.6 Time evolution of the CMDTE (bottom) and the CGR in the control simulation (upper) averaged over the whole domain (solid curves), the mountain area (dashed curves), and the plain area (dotted curves) for FLAT (blue) and TOPO (orange). The ranges of the mountain and plain areas are indicated in Fig. 3.5d.

To examine the initial error growth at different horizontal scales, we further compute power spectra of CMDTE in wavenumber space (Fig. 3.7). The power spectra of the control simulation at 1300 LT when the growth of the error slowdown in both FLAT and TOPO are also plotted as a reference of the background energy spectrum. During the first 3 h, both the errors in FLAT and TOPO grow at the domain scale (~100 km). From 0900 LT, the error spectra start to behave differently. In TOPO, the power spectra start to grow at about 2-km

scale before 0900 LT and continue to grow at scales below 50 km, pronounced at the *O*(10 km) scale. The spectra then spread to larger scales after 1040 LT, indicating a peak at about 20 km at 1100 LT. In FLAT, on the other hand, the spectra start the growth at a late time after 0940 LT, and instead of propagating throughout the scales below 50 km, they amplify at scales below 10 km and have peaks at a scale corresponding to individual convective cells (~5km) at 1100 LT. In this way, the characteristic of the error spectra again shows the properties related to different temporal and spatial features of the convection development in FLAT and TOPO. Specifically, the power spectra of TOPO start to pronouncedly amplify earlier at a larger scale than those of FLAT, corresponding to the early development and larger horizontal scale of the convective clouds due to the existence of the mountain.

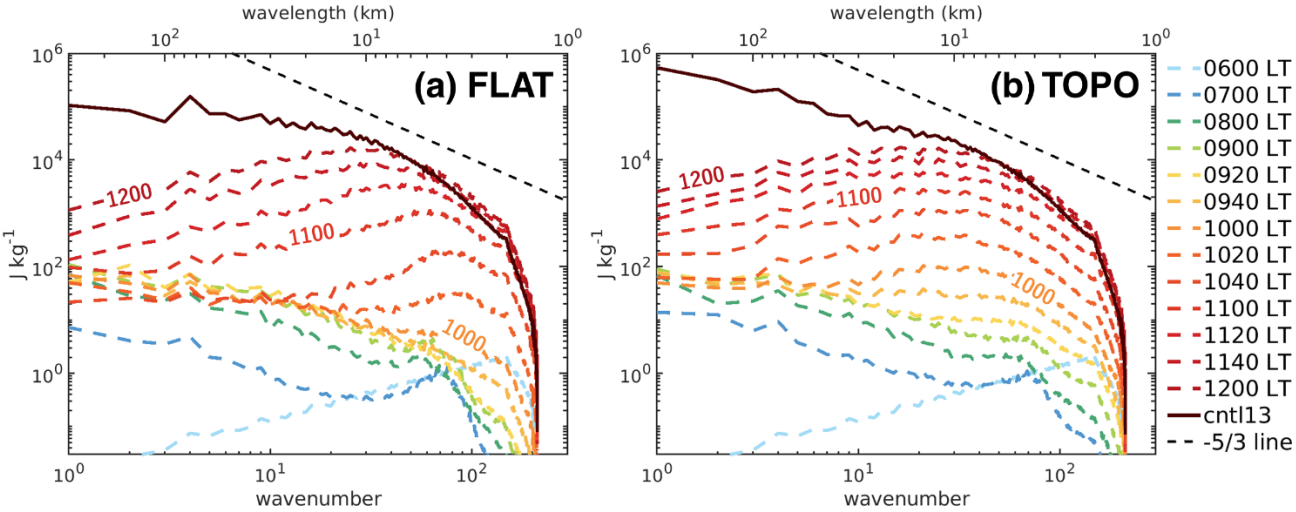

Figure 3.7 CMDTE power spectra averaged below 10-km height (color dashed curve) in (a) FLAT and (b) TOPO. The dark red solid curve shows the power spectrum of the control simulation at 1300 LT on 23 June. The black-dashed line shows the reference of a -5/3 spectrum slope.

Besides FLAT and TOPO, other experiments also show error growth corresponding to the development of moist convection. Figure 3.8 depicts the horizontal distribution of the CMDTE at the time right after convection initiation for the experiments with different

mountain topography and background winds. The distribution of convective clouds is depicted by the defined cloud grids to show the convection development within several hours after the convection initiation. To better show the detail of the distribution of errors and convective clouds, only a portion of the domain with 150×150 km range is depicted. For the experiments with mountain topography, the plots show the sub-domain around the mountains; for the experiments without mountain topography, the plots show an arbitrarily selected sub-domain containing convective clouds during convection initiation time. Consistent with the results of FLAT and TOPO, Fig. 3.8 also shows that the distribution of large errors coincides with the location of convective clouds.

In general, by comparing the convection development and the error growth dynamics, the results in this section showed the ability of moist convection to trigger the rapid error growth. Thus, the spatial, temporal, and spectral evolution and distribution of errors reflect the characteristic of convection development. To further address the impact of mountain topography on this error growth, in the following we will compare the errors based on the degree of convection development, such as the size of convective clouds or the CGR. For example, in Fig. 3.8, the error magnitude between TOPO and H500, or between TOPO and U00_TOPO is apparently different when the convective clouds in them have similar horizontal sizes. This point will be examined in more detail in the next section. The question here is that for moist convection at a similar development stage, whether the one developing under the influence of mountain topography triggers different error growth from that without the forcing of topography? Also, if there are differences, does this topographic effect behave differently under different mountain geometry?

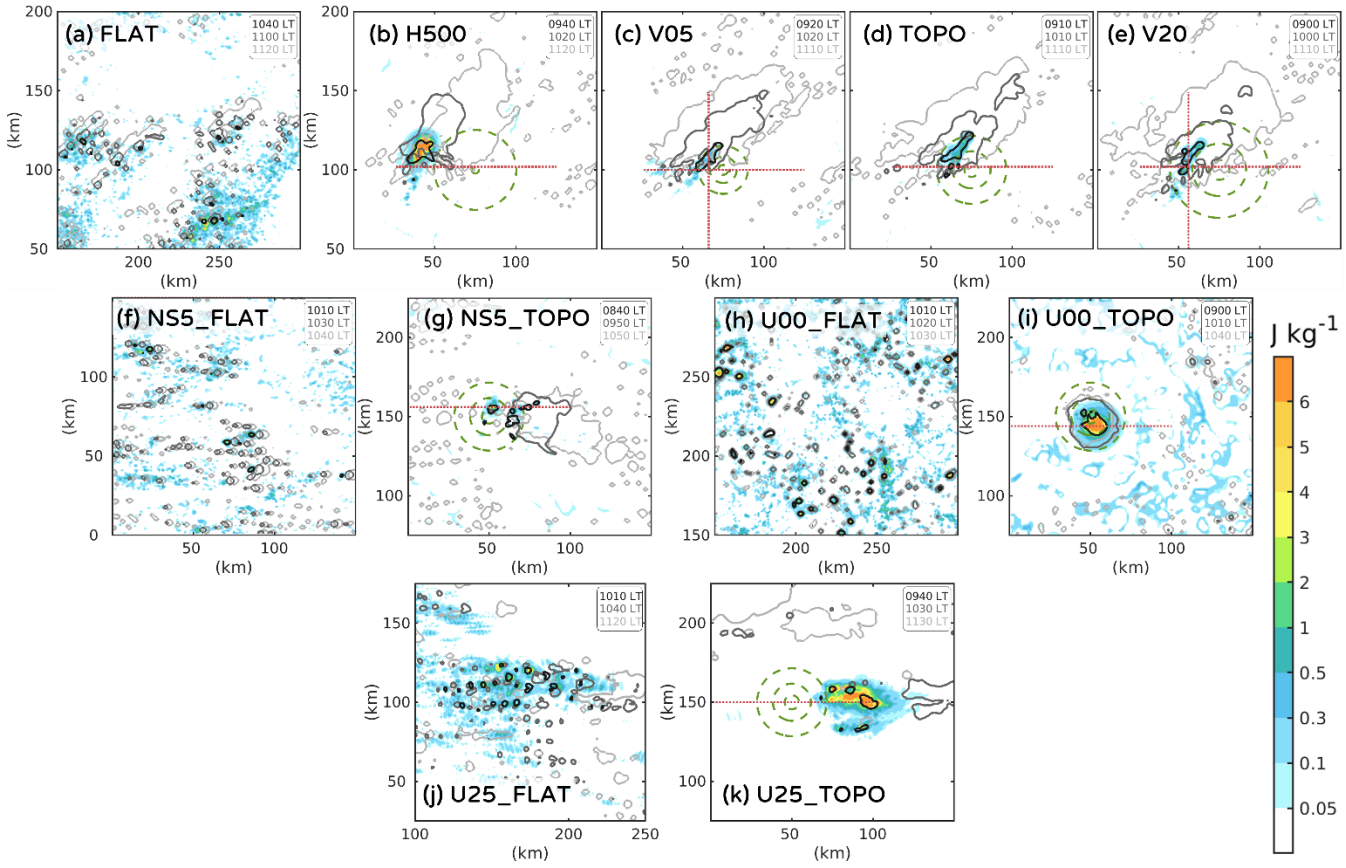

Figure 3.8 The CMDTE at the time of CGR equal to 0.1 % (color shaded) and the distribution of defined cloud grids at the times of CGR equal to 0.1, 1, and 5 % (black, gray, and light gray contours, respectively) for (a) FLAT, (b) H500, (c) V05, (d) TOPO, (e) V20, (f) NS5_FLAT, (g) NS5_TOPO, (h) U00_FLAT, (i) U00_TOPO, (j) U25_FLAT, and (k) U25_TOPO. The times of the contours are depicted by the numbers with the same color in the upper right of each panel. The green dashed contours depict the terrain height equal to 100, 500, 900 m. The red dotted lines show the location of the cross section depicted in Figs. 3.17-3.19 and 3.21. In (k), only the cloud grids between y=75~225 are counted to calculate CGR as the threshold of the plotting time to show the convective clouds downstream of the mountain. Note that only a portion of the whole computation domain is depicted here.

3.2 Topographic effects on error growth

In the previous section, we have shown the development of the simulated thunderstorms and the associated error growth dynamics. The experiments with and without topography show different features of error growth because convective clouds develop differently in them, highlighting the impact of topography on convection development. However, it is still difficult to conclude whether topography affects the error growth trigged by moist convection when the features of error shown in Figs. 3.5–3.7 greatly reflect the characteristic of convection development. For example, while the slope of the whole domain averaged error growth between 0900 to 1200 LT seems to be slightly shallower in TOPO than in FLAT (Fig. 3.6), it may only be because the error is smaller over the plain area due to the lack of moist convection, and not directly suggest that topography affects the error growth triggered by the moist convection itself.

Therefore, analysis based on the degree of convection development is desired to show the topographic effect on the error growth when the moist convection is occurring, regardless of the temporal or spatial difference in convective clouds. One idea here is to collect the results from different times and compare the error associated with each convective cloud of similar size. To do that, we detect individual cloud areas at different times and calculate CMDTE over each cloud area. The cloud areas are detected by finding the horizontal continuous regions of the cloud grids (identified in the control simulation; see Section 2.4.3) having 10 grids or larger. The detection of cloud area is illustrated by the red boxes in Figs. 3.5a and 3.5d; the area enclosed by a black contour in a red box represents an exact detected cloud area which is used to produce the following analysis.

Figure 3.9 depicts the scatterplots of the area size against the error for each detected cloud area in FLAT and TOPO. Here, the size of a cloud area is represented by the diameter of circles

with the same area size as the detected cloud area. The error is depicted in terms of the mean of the first 10 maximum values of vertical mass-weighted averaged CMDTE over the detected cloud areas, which represents the maximum magnitude that the error associated with a convective cloud could reach. The idea here is, assuming that rapid error growth is mainly triggered by moist convective processes, the convective clouds at a similar stage are expected to result in similar error magnitude when there is no external forcing like topography. Thus, comparing the errors among convective clouds of a similar size helps us address the topographic effects on the error growth.

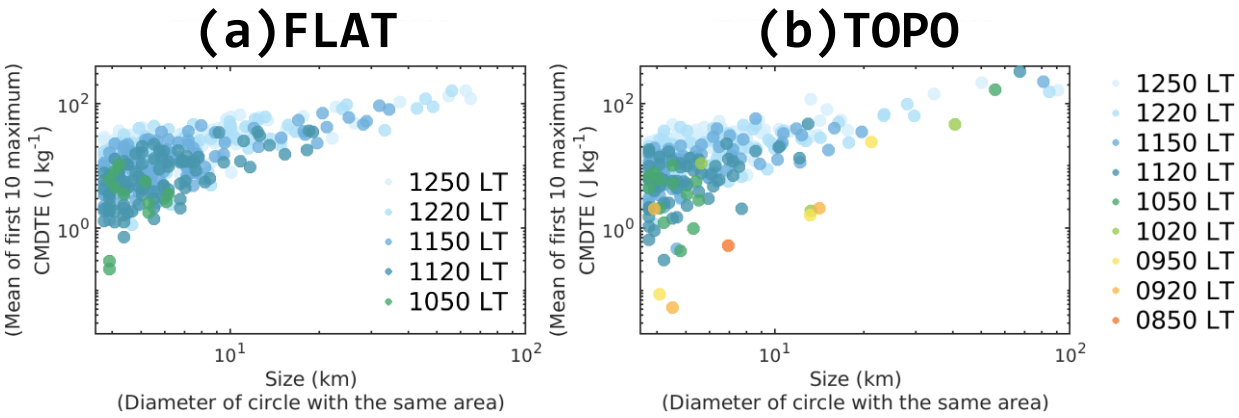

Figure 3.9 Scatterplots of the cloud size (x-axis) against the magnitude of CMDTE (y-axis) for cloud areas detected from (a) FLAT and (b) TOPO. Each point represents the results from a detected cloud area at a time represented by the color.

Comparing the results of FLAT and TOPO in Fig. 3.9, the scatterplots of TOPO after 1050 LT have similar distribution with those in FLAT (c.f. the points with cold color in Figs. 3.9a, b). However, some convective clouds in TOPO before 1050 LT result in scatterplots showing smaller errors than other clouds of similar sizes (c.f. the points with warm and cold color in Fig. 3.9). In TOPO, for example, there are three points of cloud area of about 15-km sizes having the error magnitude around *O*(1) (Fig. 3.9b), while in FLAT, the results with similar cloud area sizes could have an error magnitude large to *O*(10). The warm color points

in Fig. 3.9b correspond to the convective clouds that develop over the mountain area in the morning. For example, the three yellow points of 0950 LT in Fig. 3.9b are exactly the results of the cloud areas illustrated in Fig. 3.5d. The difference between Figs. 3.9a and 3.9b suggests that for convective clouds with similar size, those developed over the mountain have smaller errors at the early stage of development, implying the topographic effects on decreasing the error growth triggered by moist convection.

The topographic effect shown in Fig. 3.9 by comparing the results of FLAT and TOPO is further examined with different mountain geometry. Figure 3.10 shows the scatterplots of the errors against the size of cloud areas, just similar to Fig. 3.9 but depicting several experiments together in a diagram. The color scale here is then designed differently to distinguish Fig. 3.10 from Fig. 3.9. For the experiments with topography, only results of convective clouds before 1040 LT are shown here, because after this time convective clouds develop everywhere over the whole domain just like those in FLAT, and their results cover almost the same area as those in FLAT in the scatterplots (c.f. Figs. 3.9a, b); the results from FLAT are depicted completely just like Fig. 3.9a. In Fig. 3.10, the results from FLAT represent the relationship of the error magnitude with convective cloud size in the absence of the topographic effects. The impact of the mountain is then assessed by how the results of the experiments with topography depart from the area possessed by the square points (illustrated by the dashed triangle in Fig. 3.10a).

Figure 3.10 shows the topographic effect on mitigating error growth when the mountain is higher than 750 m. Specifically, many scatterplots of the experiments with topography in Figs. 3.10b-d locate outside the triangle area of FLAT, while most of them in Fig 3.10a are located within the area or at its edge. In other words, more convective clouds in the experiments with mountains higher than 750 m result in smaller errors than those clouds of similar sizes in FLAT. In contrast, the convective clouds in the experiments with 500-m mountain height show a similar magnitude of errors as those in FLAT. The mountain width,

although not as clearly as the mountain height, also shows different effects on the error growth. For example, Fig. 3.10b shows that some convective clouds with a size around 5 km in H750_V20 have slightly larger errors than those in H750_V05. Similarly, the results in Fig. 3.10c also show some convective clouds in V20 having larger errors than those in V05.

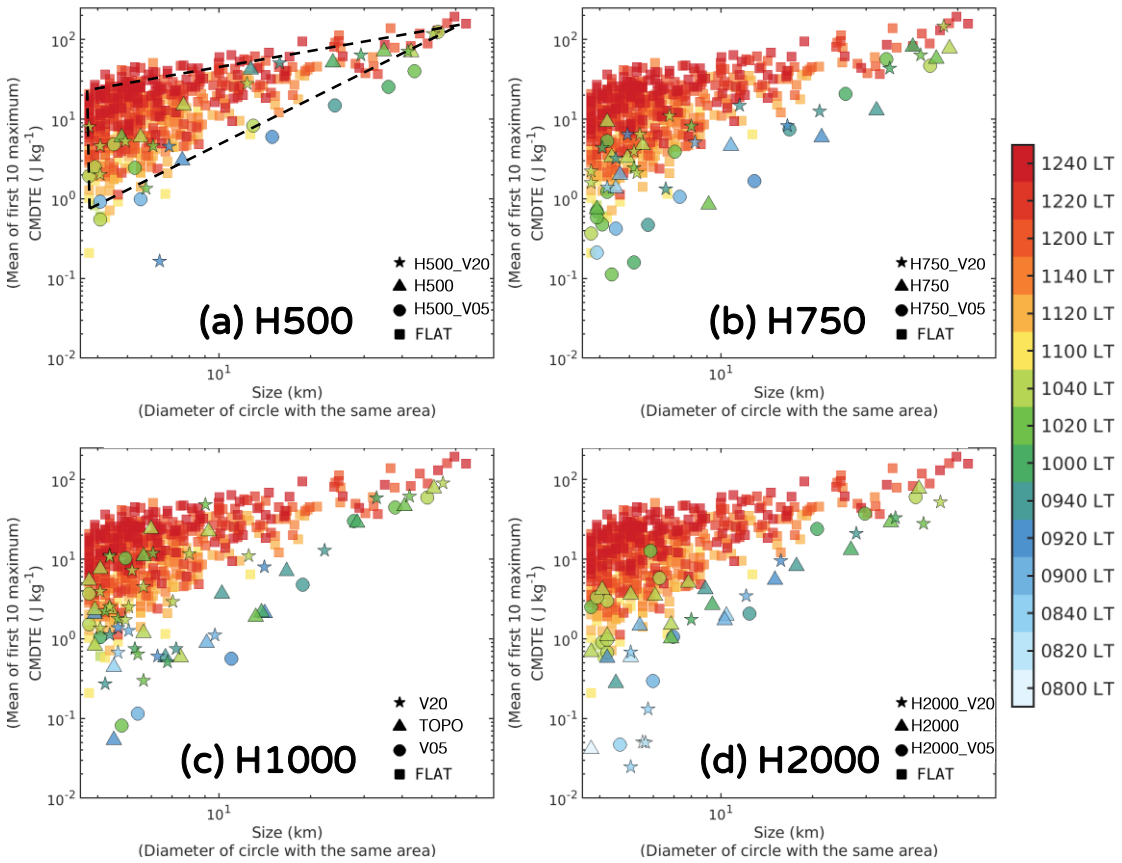

Figure 3.10 Similar to Fig. 3.9 but for results from FLAT depicted together with results from the experiment with (a) 500-m, (b) 750-m, (c) 1000-m, and (d) 2000-m height mountains (see Table 2.1 for the setting in each experiment). The square points of results from FLAT are the same in all panels; the dashed-line triangle in (a) illustrates the area possessed by them. Note that the color scale is different from Fig. 3.9 for distinguishing the plotting of several experiments in one diagram from the one with only one experiment.

Besides the comparison based on the horizontal sizes of convective clouds, we further compare the convection development and the error growth in the vertical direction. Figure 3.11 shows the time-height cross section of horizontally averaged CMDTE and the maximum

hydrometeors of the control simulation over a sub-domain. The range of the sub-domain is exactly the portion depicted in Fig. 3.8 for each experiment. The hydrometeors represent the development of moist convection in the vertical direction over time; the CMDTE shows the corresponding error growth. In FLAT, moist convection develops upward quickly from 1020 LT, and the error also grows rapidly, by an order of magnitude or greater, as soon as the convective clouds develop up to a specific height (Fig. 3.11a). It demonstrates that the error growth in the vertical direction is also highly related to the development of moist convection.

The topographic effects on the error growth are also shown in the vertical direction. In TOPO, the vertical development of moist convection starts at 0820 LT (Fig. 3.11b), earlier than that in FLAT because of the presence of the mountain. After the convection development started, the error in TOPO grows much more slowly than that in FLAT, suggesting that the topography has an effect of restraining the error growth. For example, after the convective cloud develops up to 5-km height in TOPO, it takes over one hour for the error at the same height to grow from below 0.001 to over 0.1 $\mathrm{J\,kg^{-1}}$, while it only takes around 30 minutes in FLAT.

The sensitivity of topographic effects to the mountain height and volume is also shown in the time-height cross section by comparing the results of TOPO, H500, and V20 (Figs. 3.11 b-d). In H500, different from TOPO, the error grows an order of magnitude or greater rapidly, similar to the one in FLAT (c.f. Figs. 3.11a-c). For example, at 5-km height, the error in H500 grows from 0.001 to over 0.1 $\mathrm{J\,kg^{-1}}$ within only 20 min. Although not as apparent as the sensitivity to the mountain height, different mountain width also lead to different topographic effect on mitigating error growth. In V05, for instance, while the vertical development of convective clouds seems to be similar to that in TOPO, the error grows less rapidly than in TOPO at the early stage of convection development (c.f. Figs. 3.11b, d). For example, at the 5-km height, the error in V05 stays below 0.001 $\mathrm{J\,kg^{-1}}$ for 20 minutes after the convection

develops up to that height at 0850 LT, while the one in TOPO grows an order of magnitude to 0.01 J kg^{-1} after 20 minutes of the formation of the clouds.

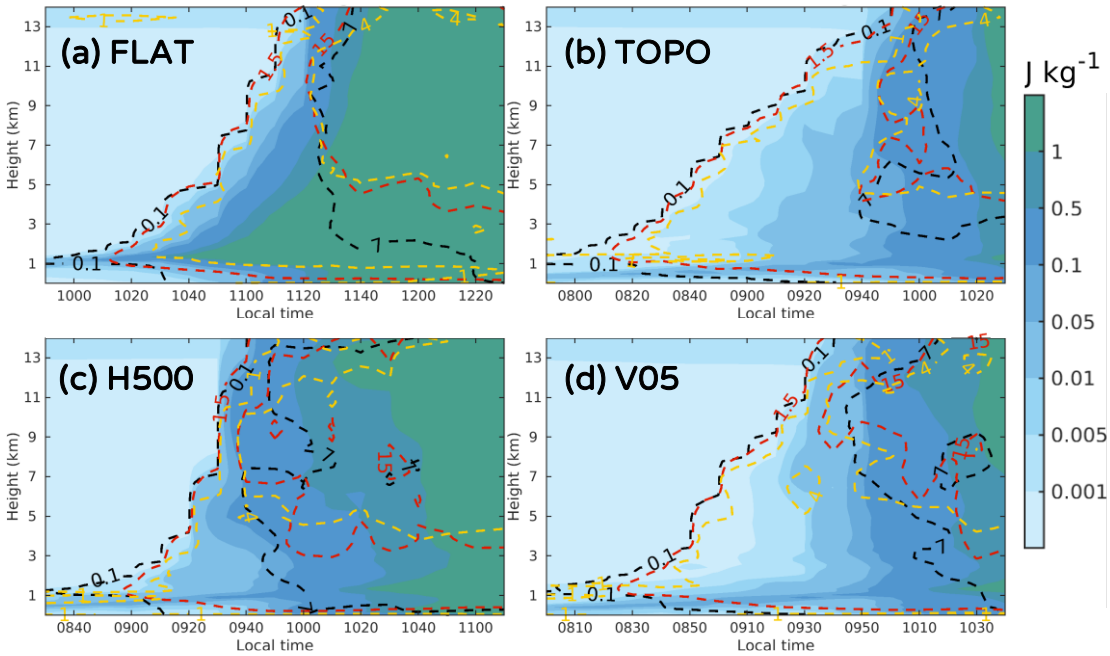

Figure 3.11 The time-height cross section of the horizontally averaged CMDTE (color shaded), and the horizontally maximum of hydrometeors (black dashed contours; 0.1 and 7 g kg^{-1}), upward wind (red dashed contours; 1.5 and 15 m s^{-1}), and θ anomaly (yellow dashed contours; 1 and 4 K) in the control simulations of (a) FLAT, (b) TOPO, (c) H500, and (d) V05. The results are calculated over a sub-domain whose range for each experiment is exactly the portion depicted in each panel of Fig. 3.8.

To further examine the topographic effects on different model state variables, the growth of different terms in the CMDTE (DiKE, DiSH, and DiLH; see also Section 2.4.1) is compared by the ratio of error in wavenumber space relative to the saturation error (Fig. 3.12). The saturation error is defined as the error at the time when the error growth rate λ (see Section 2.4.1) becomes smaller than 0.01 (refer to the black dashed-dotted line in Fig. 4.3). Figure 3.12 depicts the relative error spectra with the curves colored by the CGR, which represents the convection development. The time of the CGR starting to have non-zero values is seen as the time of convection initiation (CI). The results in Fig. 3.12 are plotted every 30 minutes for

8 hours, including the times of, before, and after CI. A larger space in the y-direction between curves means the more rapid error growth at that scale.

The different terms of the errors have different properties. In FLAT, before CI, DiKE and DiSH grow little while DiLH starts the growth throughout all scales. Regardless, all three terms of errors in FLAT have sudden rapid growth at scales below 20 km at the time of CI. In comparison, both TOPO and H500 have slower DiLH growth than FLAT, especially at scales smaller than 10 km at the time of CI. For example, 30 minutes before the CI, the relative error of DiLH in FLAT already has a magnitude of 1 % at the 2-km scale, while those in TOPO and H500 are around 0.1 %. For DiKE and DiSH in TOPO and H500, they also grow little before the CI. However, H500 shows sudden growth of DiKE and DiSH especially at the scales below 100 km after the time of CI while those in TOPO grow more gradually even after CI. Figure 3.12 suggests the different properties of error growth as well as different topographic effects on different model state variables. Particularly, DiKE and DiSH grow little before the CI in all experiments, while they have sudden growth around the time of CI in FLAT and H500, but not in TOPO. In comparison, DiLH starts the growth before CI in all experiments, while those in TOPO and H500 grow less rapidly than that in FLAT.

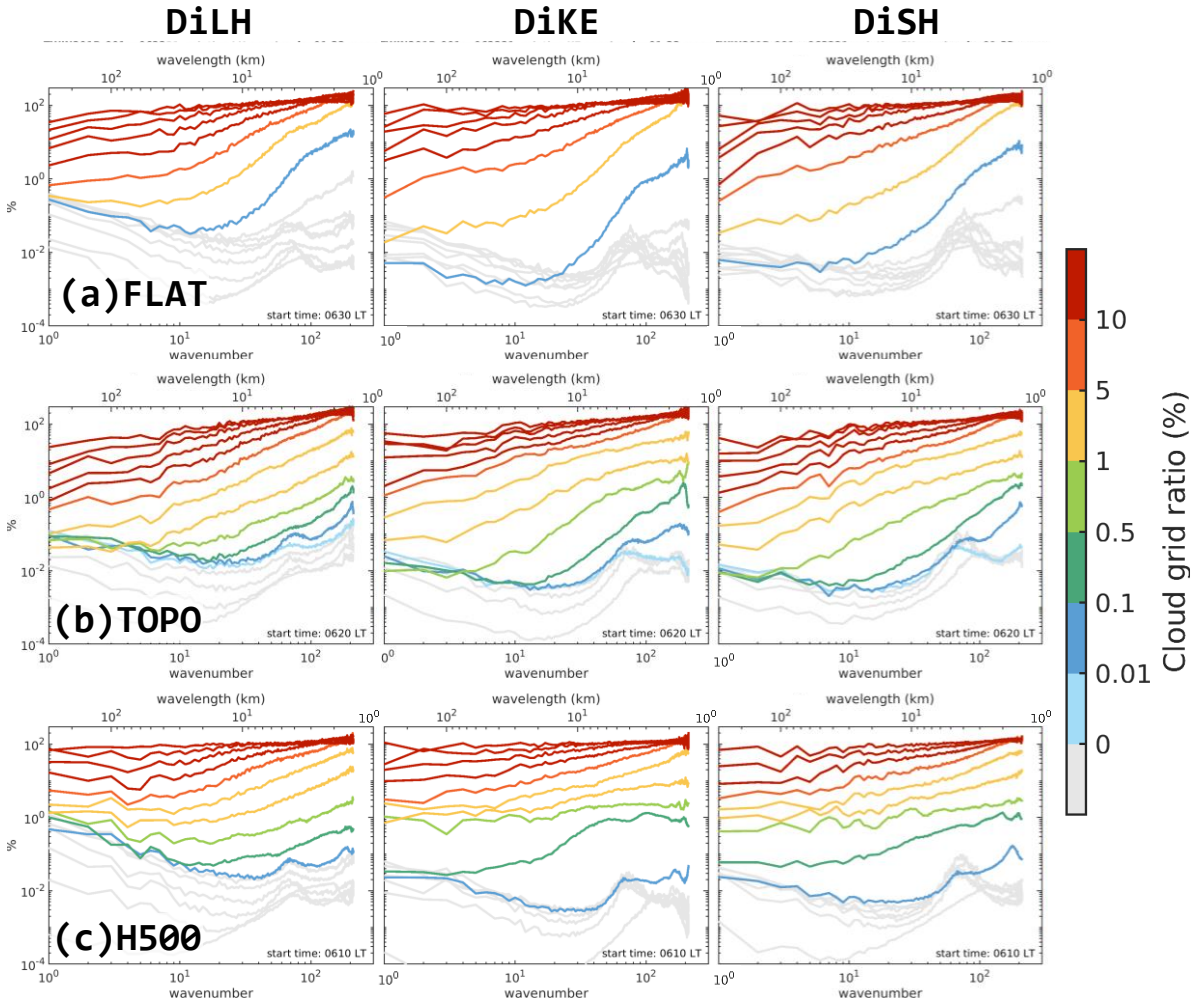

Figure 3.12 The relative error spectra of DiLH (left), DiKE (middle), and DiSH (right) in (a) FLAT (upper), (b) TOPO (middle), and (c) H500 (bottom). The curve color depicts the CGR over the whole domain of each experiment. The time interval between each curve is 30 minutes; the time of the first curve is depicted on the right bottom of each panel.

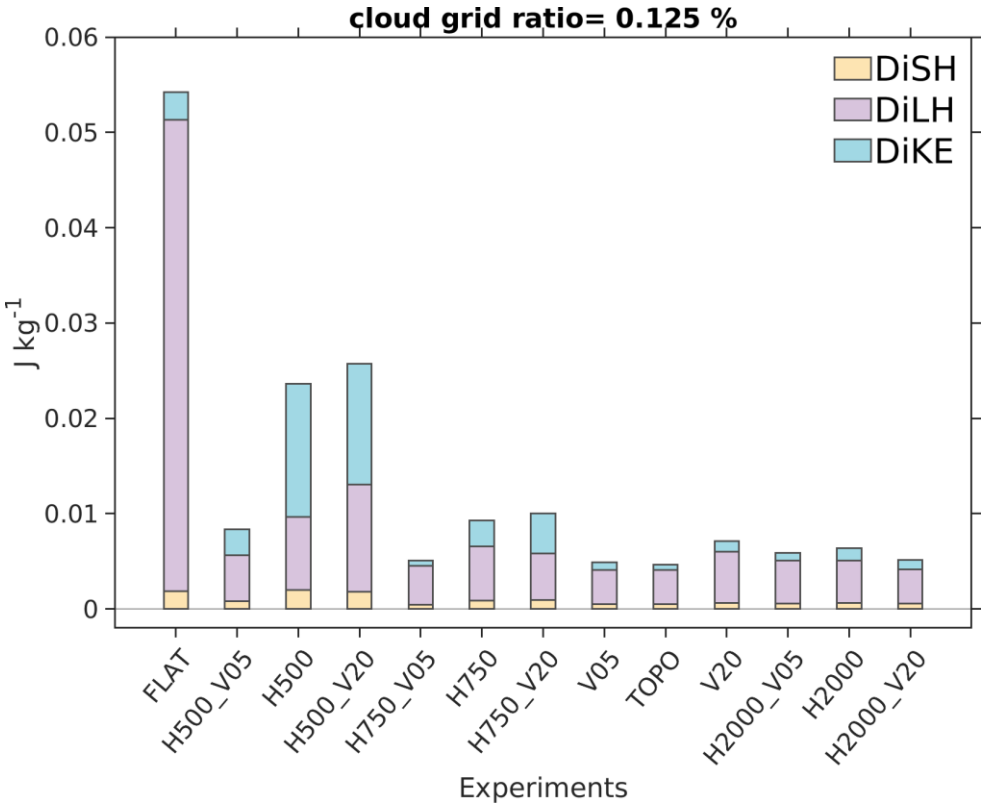

Figure 3.13 The value of DiSH (yellow), DiLH (purple), and DiKE (blue) at the time when the CGR over the whole domain reaches over 0.125% in each experiment (x-axis).

Figure 3.13 further presents the value of DiKE, DiSH, and DiLH when the CGR over the whole domain becomes larger than 0.125 % in each experiment using the original sounding wind profile (see Table 2.1). This threshold (0.125 %) is chosen for depicting the results at an early stage of moist convection development. The CGR equal to 0.125 % means that there are about 113 cloud grids over the whole domain. If these grids are one convective cloud, they can be converted to a cloud area with a size equal to 12 km depicted in Figs. 3.9 and 3.10. The CGR of 0.125 % is also within the dark green colored interval in Fig. 3.12.

At the time of this early stage of convection development, Fig. 3.13 compares the absolute values of different error terms among the experiments. In FLAT, the total error of DiKE, DiSH, and DiLH is the largest among the experiments; meanwhile, among three terms of the error in FLAT, DiLH is the largest one. In comparison, all experiments with mountain topography

show smaller total errors than FLAT at the early stage of convection development. The experiments with higher and narrower mountains tend to have smaller total errors, similar to the sensitivity shown in Figs. 3.10 and 3.11. Notably, the reduction of errors is mainly shown in DiLH. All experiments with mountain topography have much smaller DiLH than FLAT. Among the experiments with mountain topography, the differences are mainly shown in the term of DiKE. H500 and H500_V20 even have larger DiKE than FLAT at this early stage of convection development.

The comparison of different terms in CMDTE (Figs. 3.12 and 3.13) shows that the mountain topography has more impacts on the error of water vapor regardless of the mountain height or width, while the impacts on the errors of wind and temperature are less clear with lower and wider mountains. In H500, for example, the rapid growth of the error on the wind field may consequently result in a comparable CMDTE magnitude as FLAT, as the results shown in Figs. 3.10 and 3.11. This sensitivity of the topographic effects on the error growth of the different variables to the mountain geometry is considered to come from different mechanisms of CI. Further discussion is provided in Section 3.4.

3.3 Sensitivity experiments for the topographic effects on error growth

In the previous section, we demonstrated the impact of mountain topography on the error growth triggered by moist convection, which shows the sensitivity to the mountain geometry on different terms of the error. In this section, we further examine the sensitivity of this topographic effect to environmental flows and two other potential affecting factors: the absence of moist processes and the initial uncertainty on different model state variables. The former is examined by the experiments without microphysics parameterization; the latter is assessed by conducting twin experiments with initial differences added to potential

temperature (θ).

3.3.1 Different environmental flow conditions

The experiments without and with mountain topography under different background winds (Table 2.1) are compared to see if the topographic effects on mitigating the error growth are also found under different environmental flows. Figure 3.14, similar to Fig. 3.10 but for experiments with different wind conditions, shows the scatterplots of convective cloud sizes against the error magnitude. Here, the results of the experiments with topography are shown only before 1000 LT for the same purpose as that for Fig. 3.10 in which only the results before 1040 LT are depicted. The results in the experiments without topography are shown completely.

Moreover, in Fig. 3.14, some results from the experiments with topography are plotted with thick black edges, and some are not. The different edges distinguish the cloud areas near or downstream of the mountain (with thicker edges) and those not (without thicker edges). In the experiments with the U25 wind profile, many detected cloud areas are not located around the mountain, shown by the scatterplots without thick edges in Fig. 3.14d. In these experiments, some convective clouds did not disappear at night and kept their large size (~100 km) moving eastward over northern or southern parts of the domain until the morning (refer to Fig. 3.4f). These clouds are probably caused by the periodic lateral boundary condition making the southern and northern parts of the domain become the area between the two mountains because the terrain is virtually repeated under the periodic boundary condition. Thus, there may be suitable conditions, such as a convergence zone, over northern or southern parts of the domain that maintain the clouds not to dissipate. These clouds are not initiated by solar heating in the morning and thus are not our focus. Therefore, the comparison here will be focused on the results with thicker edges in Fig. 3.14, i.e., the convective clouds near or downstream of the mountain.

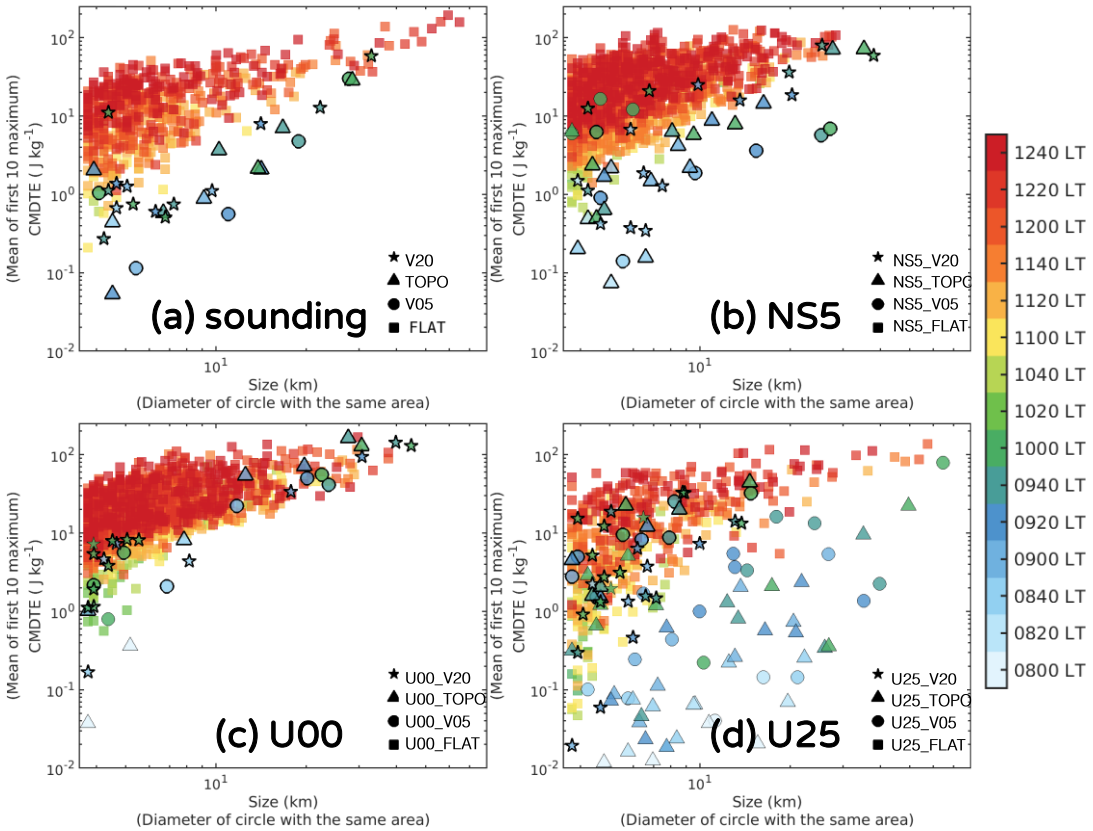

Figure 3.14 Similar to Fig. 3.10, but for the experiments with different background winds of (a) the original sounding data, (b) NS5, (c) U00, and (d) U25. Panel (a) has the same results as that shown in panel (c) in Fig. 3.10. The thicker edges of the points indicate the results from the detected cloud areas whose center is located in the area depicted by the green-dashed box in Fig. 3.4f for (b)-(d) and in the areas shown by Figs. 3.8c-e themselves for (a).

Similar to Fig. 3.10, the square scatterplots in Fig. 3.14 represent the error evolution with time and convection development when there is no topographic forcing. Again, if the results from the experiments with topography are located away from the area of the square scatterplots, it implies the impact of the mountain topography on error growth. Compared to the cases with the original background winds (Fig. 3.14a), the topographic effects are comparable in the experiments with constant background wind (NS5, Fig. 3.14b) but less clear in the experiments

without background wind (U00, Fig. 3.14c). For the experiments with the U25 wind profile (Fig. 3.14d), if we only focus on the results near and downstream of the mountain (i.e., the scatterplots with thicker edges), it is shown that the error magnitudes for these convective clouds are similar to those in FLAT, implying fewer topographic effects on the error growth associated with thermally induced moist convection. In this way, Figure 3.14 demonstrates the sensitivity of topographic effects on the error growth to environmental flows. Possible reasons for these sensitivities will be further discussed in Section 3.4.

3.3.2 Simulations without moist processes

The experiments without microphysics parameterization are conducted to assess the error growth dynamics and the sensitivity of topographic effects without moist processes. Here, the same initial condition at 0600 LT 23 June (i.e., the start time of twin experiments) of control and perturbed simulation in FLAT, TOPO, and H500 are used, and additional integrations are performed for both control and perturbed simulations after turned off the microphysics parameterization. These no-microphysics experiments are denoted as FLATnoMP, TOPOnoMP, and H500noMP, corresponding to the experiments with microphysics parameterization and the same topography, i.e., FLAT, TOPO, and H500, respectively.

Figure 3.15 shows the error evolutions of these experiments. For no-microphysics experiments, there is almost no error growth before 1100 LT regardless of the topography settings, suggesting a much lower nonlinearity in the simulated dynamical system without moist processes being parameterized. After 1100 LT, the rapid error growth found in the no-microphysics experiments is considered to be triggered by the dry convection induced by the solar heating. In the afternoon, the errors are much smaller in the experiments without moist processes than in those with moist processes. In addition, although the errors in the no-microphysics experiments reduced once in the afternoon, they continue growing after around 1500 LT without a sign of error saturation, implying a much less nonlinearity, because error

saturation is a characteristic of nonlinear dynamical systems.

In the no-microphysics experiments, while the errors averaged over the whole domain grow similarly among the experiments with different topography, those averaged over the mountain area show different evolutions. In TOPOnoMP, the error over the mountain area grows much slower than FLATnoMP and H500noMP during 1100-1300 LT. The slower error growth in TOPOnoMP suggests that topography has similar effects on error growth in the cases with and without moist processes being simulated. Specifically, topography decreases error growth, but this effect is sensitive to mountain height.

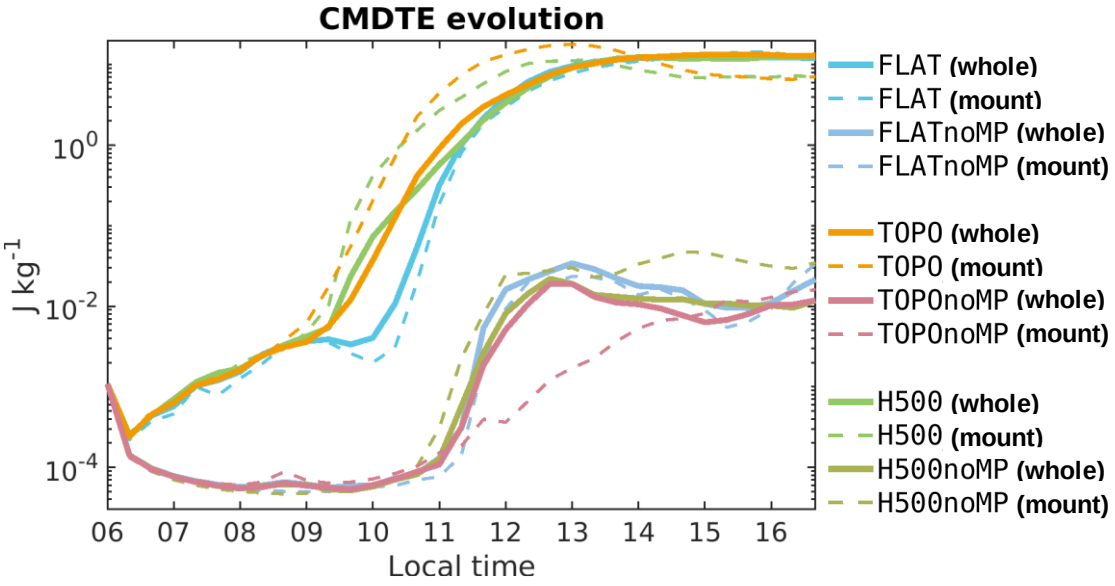

Figure 3.15 Time evolution of the CMDTE averaged over the whole domain (solid curves) and the mountain area (dashed curves) in the experiments indicated by the legend on the right. The range of the mountain area is indicated by the dashed-line box in Fig. 3.5d.

The sensitivity tests without moist processes demonstrate that the moist processes play a vital role in contributing to the nonlinearity of the atmospheric motion and weather phenomena. Nevertheless, regardless of whether moist processes are involved or not, the topographic effects on error growth have a similar sensitivity to mountain height, implying that this sensitivity is less relevant to the moist processes. Consistent with the comparison of DiKE and

DiLH in Fig. 3.12, the sensitivity tests here further suggest that the different topographic effects on error growth in TOPO and H500 can be attributed to the difference of flow dynamics but not of the moist processes like condensation or evaporation. This will be further discussed in Section 3.4.

3.3.3 Initial error on potential temperature

To assess the sensitivity of error growth and the topographic effects to the initial uncertainty in different model state variables, we performed a number of twin experiments with the initial error added to potential temperature (θ). Specifically, additional perturbed simulations are conducted by adding random perturbations with an amplitude of 0.25 K to the θ of the same control simulations used previously. The amplitude of θ perturbation used here yields the same initial magnitude of CMDTE as that of the water vapor mixing ratio used previously. The experiments using the same control simulation as FLAT, TOPO, and H500 but have perturbed simulations with initial errors on θ are denoted as FLAT_THM, TOPO_THM, and H500_THM, respectively. For convenience, the experiments with initial errors on moisture field (FLAT, TOPO, and H500) and temperature field (FLAT_THM, TOPO_THM, and H500_THM) are collectively called “the QV experiments” and “the THM experiments”, respectively.

Here, both the CMDTE and its individual terms, DiKE, DiSH, and DiLH, are examined (Fig. 3.16). Irrespective of the terms of the error, the differences among the experiments shown in Fig. 3.16 become very minor after 1200 LT. Different properties of error growth are shown for the periods before the moist convection develops (0600-0900 LT) and at the initial stage during the convection development (0900-1200 LT). Before the moist convection develops, the errors grow more slowly in the THM experiments than in the QV experiments. For DiSH in the THM experiments, they even distinctly decrease before the CI (indicated by the CGR) even though the initial error is added to the temperature field. The slower error growth implies

that before the moist convection develops, the processes in the atmosphere are less sensitive to the initial uncertainty in the temperature field.

Around the time of CI, all errors in both QV and THM experiments start to grow rapidly. After the rapid growth starts, the errors in the THM and QV experiments with the same topography become identical quickly in two hours or less. During this period (around 0930 to 1100 LT), the errors in the THM experiments grow more rapidly than those in the QV experiments. Nevertheless, the topographic effects shown in TOPO on the error growth at the early stage of convection development is also shown in TOPO_THM. Specifically, all the error terms in TOPO_THM generally stay at a similar level after convection initiates at around 0820 LT. On the other hand, FLAT_THM has exponential error growth even before its convection start to develop at 1030 LT.

The sensitivity of the topographic effect to the mountain height is also seen similarly in the THM experiments as in the QV experiments. In H500_THM, the DiKE and DiSH show sudden growth as soon as the CI, while the DiLH has similar growth as that in TOPO_THM. The results in Fig. 3.16 suggest that the sensitivity of topographic effect on DiLH is less sensitive to mountain height than that on DiKE and DiSH, consistent with that suggested by Fig. 3.12. The error growth during 0930 to 1100 LT demonstrates that the topographic effect on error growth acts similarly when the initial uncertainty is in the temperature field.

After 1100 LT, all the terms of the errors shown in Fig. 3.16 grow similarly regardless of the topography and initial error types. At this time, the convective activities (represented by CGR) become similar among the experiments with different topography. It is considered that this vigorous convective activity triggers the error growing to a similar magnitude in all experiments, despite the different error growth properties before 1100 LT. As a result, the different initial error types lead to little difference in the error growth after the mature stage of convection development, highlighting the nature of moist convection on triggering error

growth at a mature stage.

In summary, the sensitivity tests of adding the initial error to the temperature field imply the followings. First, the atmospheric processes are less sensitive to the initial uncertainty in the temperature than in the moisture field when no moist convection develops in the morning. Second, the topographic effects work similarly regardless of the initial error added to moisture or temperature fields. Last, the moist convection at mature stages can trigger errors growing to a similar level, despite the difference of the error growth at initial stages.

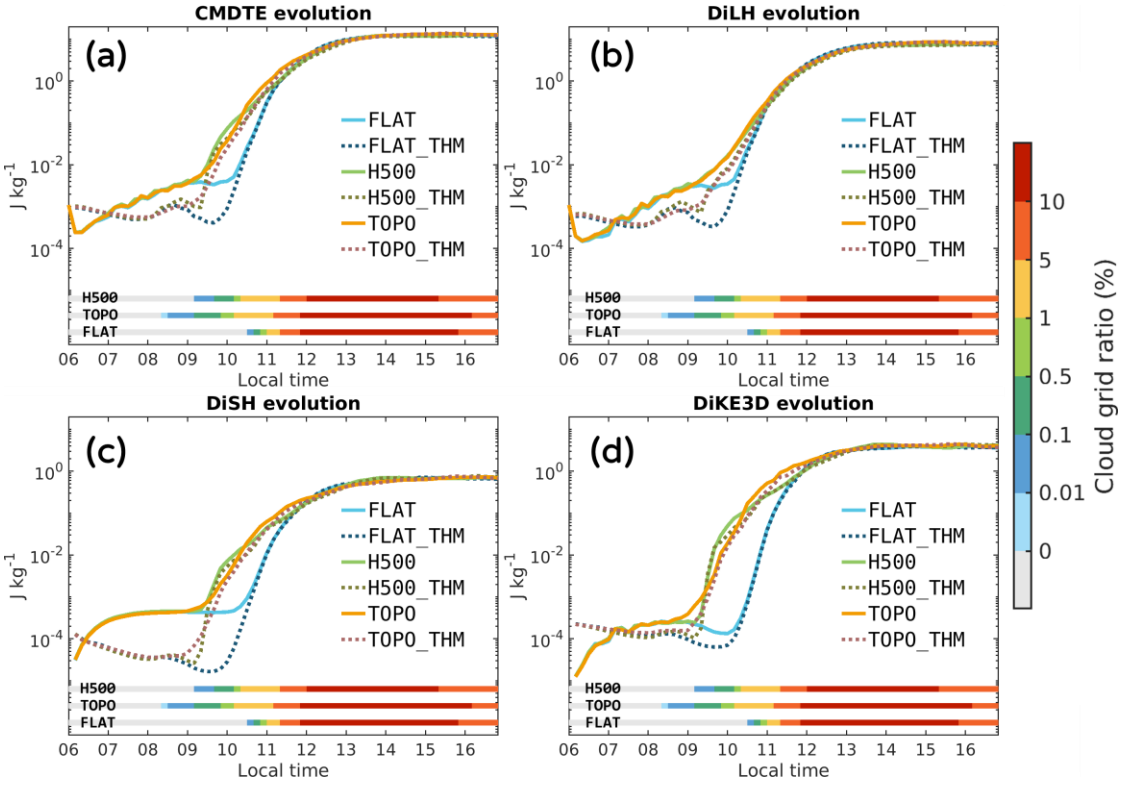

Figure 3.16 Time evolution of the (a) CMDTE, (b) DiLH, (c) DiSH, and (d) DiKE averaged over the whole domain in the QV (FLAT, TOPO, and H500) and THM experiments (FLAT_THM, TOPO_THM, and H500_THM). The colored lines at the bottom of each panel depict the CGR in the control simulation of FLAT, TOPO, and H500 from the bottom to top, respectively; they are the same in each panel. The THM experiments share the same control simulations as the QV experiment, so the CGR depicted here is also the one in the THM experiments.

3.4 Mechanisms for the topographic effects on error growth

In this section, we discuss the possible reason for the topographic effect on the error growth triggered by moist convection and its sensitivity to mountain geometry and background winds. The discussion is focused on the mechanisms and properties of convection initiation and development to figure out what kind of moist convective processes could be the reasons for different error growth.

First, the sensitivity of the topographic effects to the mountain height is investigated with the results of TOPO and H500. Here, we examine the cross section of θ anomaly and wind of the control simulation for these two experiments at the time when the clouds formed (Fig. 3.17). In both TOPO and H500, there is a positive θ anomaly on the lee side (i.e., west) of the mountain due to the downward motion and mixing across the isentropic, which occurred at midnight and continued throughout the nighttime. At the same time, the wind on the lee side is weak at night because of the mountain blockage; the weak wind area is clearer in TOPO than in H500 (figure not shown). After the sun rises, the solar heating on the surface of the mountain slope leads to the difference in temperature between the air near the mountain slope surface and the air away from the mountain at the same altitude, which generates positive buoyancy over the mountain slope and drives upslope wind. In TOPO, compared to H500, the higher mountain leads to a larger buoyancy force accompanied by a condition of weaker wind on the lee (i.e., west) side, resulting in the westerly upslope wind near the surface on the lee side of the mountain (see x=50~70 in Fig. 3.17a). The encounter of this thermally driven upslope wind and the background wind results in a convergence on the lee side of the mountain, triggering upward motion (see x=65 in Fig. 3.17a). Owing to this stronger upward motion, the cloud on the lee side keeps developing to a larger convective cloud, like the one depicted in Fig. 3.2h or 3.8d. On the other hand, the cloud generated by the mechanical upward forcing of the mountain on the windward (i.e., east) side (see x=80 in Fig. 3.17a) does not develop into

a deep convective cloud. In other words, the convective clouds in TOPO over the mountain in the morning are mainly initiated by the convergence of thermally driven upslope wind and the background wind on the lee side of the mountain. The similar CI mechanism on the lee side of mountains has also been indicated by previous studies (Banta and Schaaf 1987; Akaeda et al. 1995; Chen et al. 2002; Hagen et al. 2011; Hassanzadeh 2016).

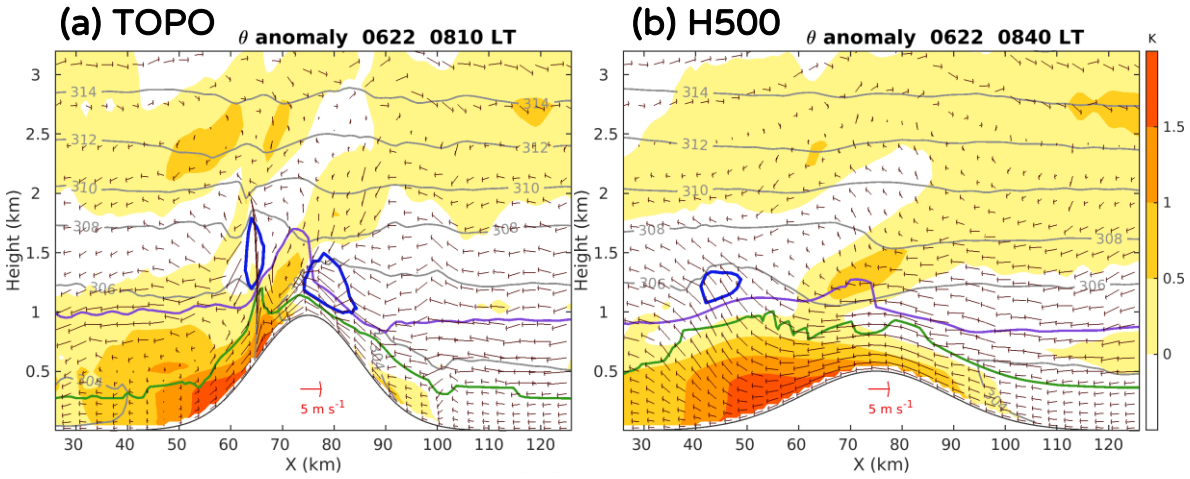

Figure 3.17 Vertical cross section in x-direction at y=102 (see red-dotted lines in Figs. 3.8b, d) of θ anomaly (color shaded), wind (arrows), and hydrometeors (blue contour; 0.1 g kg^{-1}) in the control simulation of (a) TOPO at 0810 LT and (b) H500 at 0840 LT. The purple and green curves represent the height of LFC and the thickness of the absolute instability layer, respectively.

In contrast, the above CI mechanism is absent in the experiments with a lower mountain. In H500, the mountain height is not enough to trigger the upslope wind on the lee (i.e., west) side in the morning (Fig. 3.17b). The mountain height in H500 is lower than LFC (see the purple curve in Fig. 3.17b), so on the windward (i.e., east) side, clouds also do not form due to the upslope winds caused by the mechanical forcing of the mountain. Consequently, deep convection was not initiated until the solar heating resulted in a thick enough absolute instability layer (see the green curve in Fig. 3.17b) in which the θ decreases with height. Over the area with a thick enough absolute instability layer, a small amount of upward displacement

triggered by a positive θ anomaly can easily reach LFC and induce further upward motion anywhere. This process of CI over a heated mountain is considered to result in higher uncertainty of upward wind than that in TOPO, leading to more rapid error growth.

Figure 3.17 suggests that the sensitivity of the topographic effect to the mountain height might be attributed to the different CI mechanisms in TOPO and H500. This possible reason for the sensitivity of the topographic effect is supported by the sensitivity experiments without moist processes. In Section 3.3.2, we have shown that the error growth of TOPOnoMP is slower over the mountain area than that of H500noMP. In TOPOnoMP, similar to the case in TOPO (Fig. 3.17a), upward motion on the lee (i.e., west) side occurs due to the convergence of the westerly thermally driven upslope wind and the easterly background wind (figure not shown). Similarly, H500noMP has a similar westerly flow as H500 (Fig. 3.17b) without an upslope wind on the lee side (figure not shown). There is no cloud formation in H500noMP and TOPOnoMP without the microphysics parameterization. Thus, the different properties of the dynamical flow are the most likely reason for the different error growth in these two experiments. In other words, the sensitivity of the topographic effect to mountain height can be attributed to the different dynamical processes of forming convective motion. In TOPO and TOPOnoMP, convective motion occurs in a specific area of the convergence between the background wind and thermally driven upslope wind. In comparison, in H500 and H500noMP, without the thermally driven upslope wind on the lee side, the processes of convective motion might have more uncertainty or nonlinearity than in TOPO and TOPOnoMP. Therefore, the errors, especially those of the wind field, grow more rapidly in H500 (H500noMP) than in TOPO (TOPOnoMP). The possible reason for the sensitivity of topographic effects suggested by Fig. 3.17 is also consistent with Fig. 3.12, which showed that the topographic effect on the error of wind is more sensitive to the mountain height than that on the error of moisture.

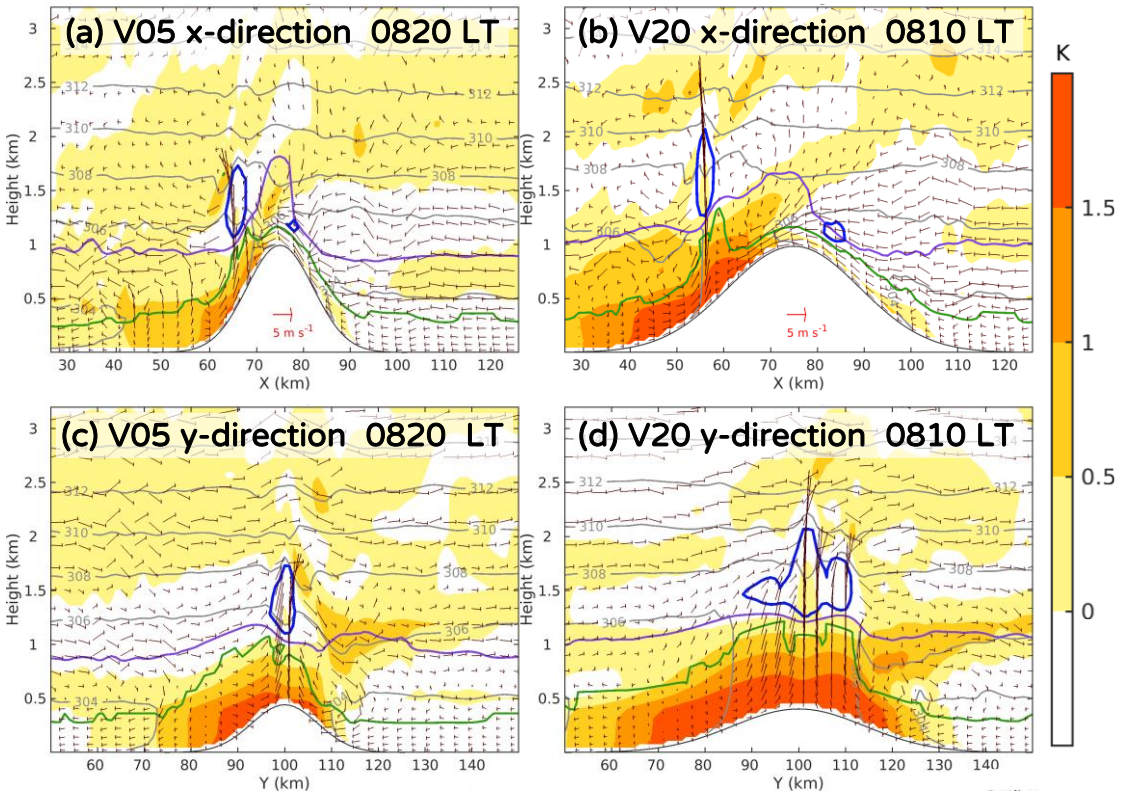

Figure 3.18 Similar to Fig. 3.17, but for (a) V05 at y=100, (b) V20 at y=102; and for the vertical cross section at y-direction of x=50 in (c) V05 and (d) V20. For the location of the cross section, please refer to red-dotted lines in Figs. 3.8c and 3.8e.

Similarly, it is considered that the sensitivity of topographic effects on error growth to the mountain width (Figs. 3.10, 3.11, and 3.13) is also caused by the different properties of the convection initiation. Here we again use the cross section of θ anomaly to compare the CI mechanisms with different mountain widths (Fig. 3.18). To clearly illustrate the difference, V05 and V20 are compared here. In both V05 and V20, similar to TOPO, deep moist convection is initiated by the convergence of the westerly thermally driven upslope wind and the easterly background wind on the west (i.e., lee) side of the mountain along the x-direction (Figs. 18a, b). The difference between V05 and V20 can be seen more clearly in the cross section along the y-direction (Figs. 3.18c, d). In V20 which has a wider mountain, the area of positive θ anomaly is broader than that in V05, and the convergence area of the upslope winds

in the y-direction seems to be also wider. Consequently, low-level air parcels have more chances to rise within this wider convergence area, which implies more uncertainty about the location of CI. The more uncertain condition results in more difference in an upward motion or the formation of the clouds, and thus, there is more error growth because of this uncertainty in V20. In comparison, the narrower convergence area of V05 could result in lower uncertainty of updraft within this concentrated area, further resulting in a smaller error at the early stage of convection development as in Fig. 3.11d.

The findings of the different CI mechanisms and their impact on the error growth lead us to further investigate the processes during convection development in the experiments with different background winds (Fig. 3.19). In U00_TOPO, the convection is triggered by the thermally driven upslope winds from all directions of the mountain and develops over the mountain top. This convective cloud almost stays at the same location and keeps developing vertically (Fig. 3.19b). With the convective cloud developing at the same place, the latent heat release from the condensation of water vapor keeps heating the air, resulting in a large positive θ anomaly. Positive θ anomaly means the warmer air than the horizontally surrounding air, indicating positive buoyancy. The positive buoyancy could further enhance upward motion, leading to stronger convection, which triggers more error growth. Therefore, a small initial difference in the location of upward motion and cloud formation could rapidly grow during the convection development. In this way, the diabatic heating from the moist convective processes plays a critical role in providing positive feedback on the error growth. This positive feedback of the moist convective process is considered to lead to rapid error growth in U00_TOPO. Thus, the errors are comparable in U00_TOPO and U00_FLAT (Fig. 3.14c), indicating less apparent topographic effects, even though the convective motion in U00_TOPO may also have less uncertainty than that in U00_FLAT at first because it is triggered by the convergence of upslope winds.

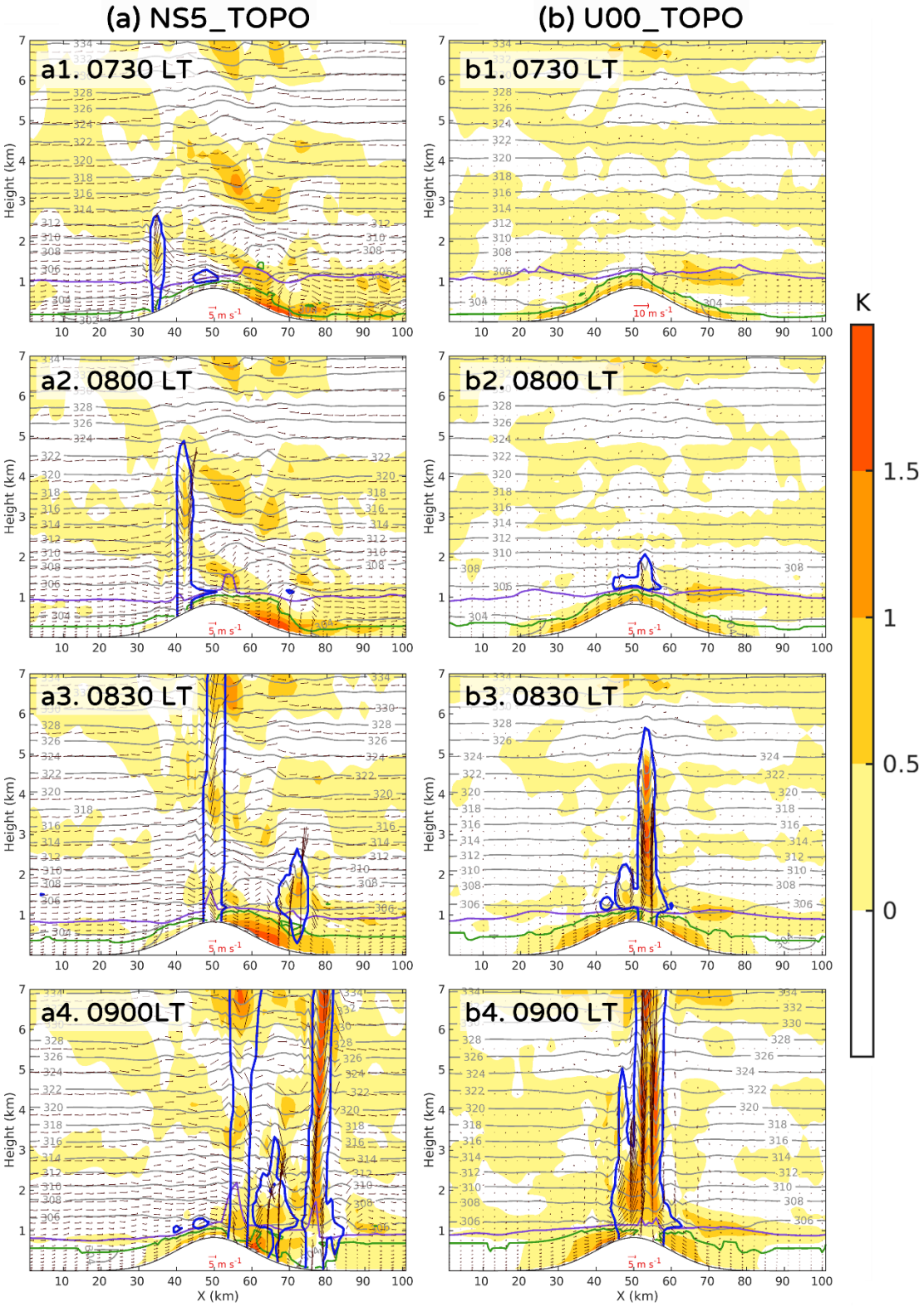

Figure 3.19 Similar to Fig. 3.17 but for (a) NS5_TOPO (y=156) and (b) U00_TOPO (y =144), respectively, from 0730 to 0900 LT in every 30 minutes interval. For the location of the cross section, please refer to red-dotted lines in Figs. 3.8g and 3.8i.

In comparison, a large positive θ anomaly is not observed in NS5_TOPO (Fig. 3.19a). In NS5_TOPO, clouds are induced by the rise of air mechanically forced by the mountain on the windward (i.e., west) side at an earlier time around 0600 LT (figure not shown) and keep developing until a later time (e.g., the one at around x=35 in Fig. 3.19a1). The clouds occurring on the windward side keep moving downstream, and hence the latent heating occurs at wider places, resulting in a weaker positive θ anomaly than in the case of U00_TOPO (c.f. Fig. 3.19a, b). The weaker positive θ anomaly means less warm air and weaker buoyancy forcing, which leads to less positive feedback on error growth. Meanwhile, similar to the case of TOPO, the convergence of the thermally driven upslope wind and the background winds is also observed in NS5_TOPO on the mountain lee side (i.e., east side, at around x=70 in Fig. 3.19a2). With this similar CI mechanism and without the strong positive feedback of diabatic heating like the one in U00_TOPO, NS5_TOPO consequently results in comparable topographic effects as TOPO (Figs. 3.14 a, b).

The different properties of convection development in U00_TOPO and NS5_TOPO suggest that diabatic heating plays and important role in the error growth associated with moist convection. The time-height cross section of the error and convective clouds further supports this point by showing the corresponding relationship between diabatic heating and the rapid error growth in NS5_TOPO and U00_TOPO (Fig. 3.20). In U00_TOPO, the amount of cloud increases rapidly and the maximum upward wind reaches 15 $\mathrm{m\ s^{-1}}$, indicating stronger moist convection, only after 1 hour when the cloud formed. At the same time, the positive θ anomaly also reaches 4 K and the error grows with orders of magnitude, from 0.001 to over 0.01 $\mathrm{J\ kg^{-1}}$ (Fig. 3.20b). In NS5_TOPO, on the other hand, the cloud amount, upward wind, and positive θ anomaly do not reach the same level as in U00_TOPO until 0900 LT, and the error also grows slowly before that time (Fig. 3.20a). It is considered that the positive θ anomaly resulting from latent heating provides further buoyancy force and contributes to both the

positive feedback of convection development and the error growth. Previous studies also have indicated similar processes of rapid error growth associated with latent heating in moist convection (e.g., Hohenegger et al. 2006; Zhang et al. 2016).

The results in Figs. 3.19 and 3.20 of NS5_TOPO and U00_TOPO imply that as the convection develops to a mature stage, more rapid error growth would be triggered by the positive feedback from diabatic heating that enhances the convective activity. Therefore, the topographic effects on error growth could become unclear after a particular stage when more vigorous moist convection is induced by latent heating. This can also be seen in the experiments with the original wind profile of the sounding data (Fig. 3.11). For example, in Fig. 3.11, the errors in all experiments with topography grow to a similar magnitude of 0.1 J kg^{-1} around the time when the upward wind and positive θ anomaly reach 15 m s^{-1} and 4 K, respectively.

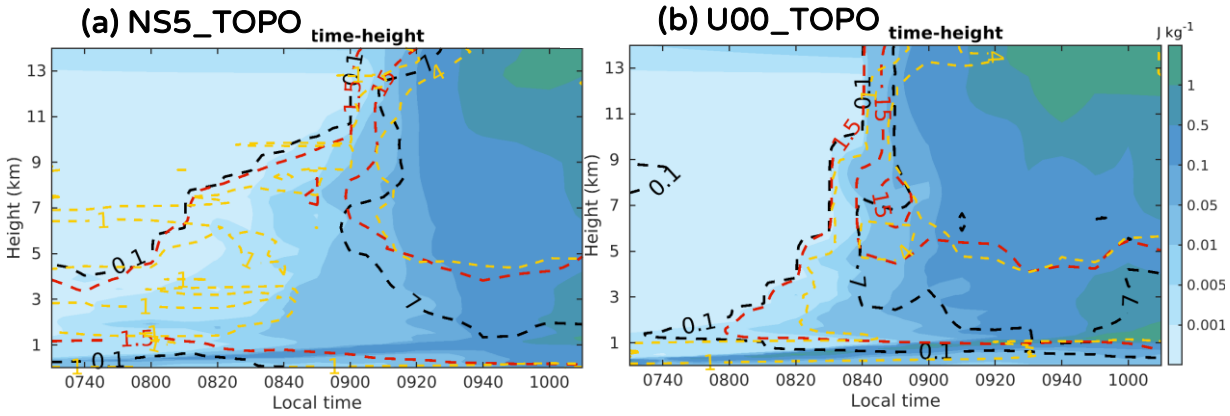

Figure 3.20 Similar to Fig. 3.11, but for (a) NS5_TOPO and (b) U00_TOPO.

For experiments with the U25 wind profile, the less clear topographic effects for thermally induced moist convection over the mountain area (Fig. 3.14d) may be attributed to the strong low-level wind shear that leads to more turbulent flows. In Fig 3.21a, which shows the time-height cross section of the error and convective clouds in U25_TOPO, the error grows

rapidly before the θ anomaly reaches a larger level (e.g., 4 K), implying that diabatic heating may not be the main reason for the initial error growth in U25_TOPO. Instead, the error growth in U25_TOPO may be triggered by the turbulent flow due to the strong wind speed shear near the surface. The strong wind speed shear results in eddies over the x-z cross section on the lee (i.e., east) side of the mountain. For example, at around x=75 below 1-km height in Fig. 3.21b, the wind vectors show the pattern of a clockwise rotation. Similar eddies patterns at around x=70~100 over the mountain area are also seen at other times during the CI in U25_TOPO (figure not shown). These eddies may play a role in mixing the low-level air with the environment and make the environment of convection development greatly different from other experiments in which similar eddies are absent (c.f. Figs. 3.17-3.19). In U25_TOPO, the error grows more rapidly before the convection development than the errors in other experiments. For example, the error in Fig. 3.21a at around 5-km height grows to over 0.001 J kg^{-1} almost one hour before the convective cloud grows to the same height; the error even grows by an order of magnitude to 0.01 J kg^{-1} at the time before the convective cloud reaches the same height at 0930 LT. This feature is distinct from the error growth dynamics in other experiments (c.f. Figs. 3.11, 3.20, and 3.21a). The results of U25_TOPO further suggest that error growth could be affected by multiple factors besides the mechanisms of triggering upward motion, increasing the complexity and difficulty of predicting thunderstorms by numerical models.

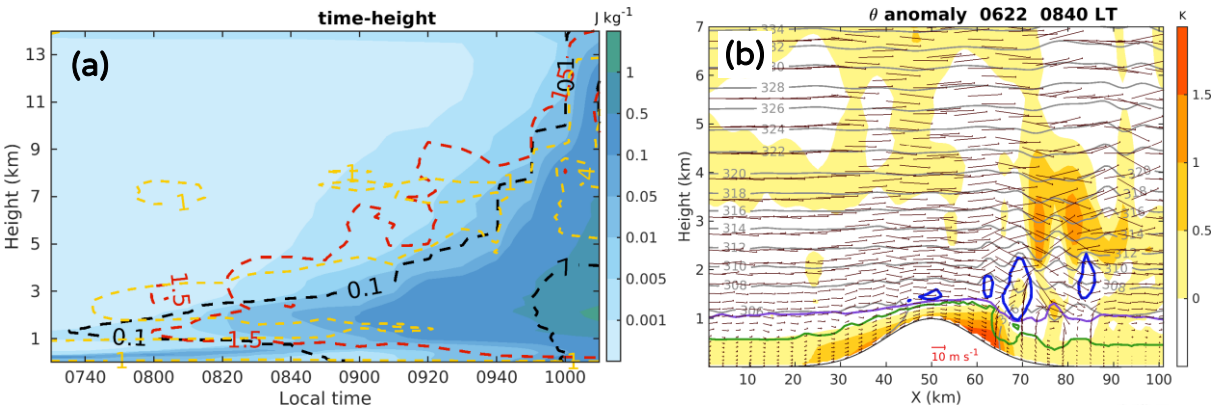

Figure 3.21 The results of U25_TOPO. (a) Similar to Fig. 3.20 but for U25_TOPO. (b) Similar to Fig. 3.17 but for U25_TOPO at y=150 (red-dotted lines in Fig. 3.8k) and 0910 LT.

3.5 Summary

In this chapter, we first confirmed the successful simulations of thunderstorms in diurnal cycles for experiments with different topography or background winds. Then the convective moist difference total energy (CMDTE) between the control and perturbed simulations in identical twin experiments is calculated to assess the error growth dynamics associated with the simulated thunderstorms. It is shown that the spatial, temporal, and spectral evolutions of the error are highly related to the development of moist convection for both experiments with and without topography.

To examine whether mountain topography affects the error growth triggered by moist convection at a similar life stage, the error is compared based on the degree of convection development. Both the comparison based on the horizontal sizes and evolution in the vertical direction of convective clouds suggests the topographic effects on mitigating the error growth triggered by thermally induced moist convection. Specifically, the errors are smaller associated with the convective clouds over the mountain than over flat areas at their early developing stage.

The experiments with different topography settings further reveal the sensitivity of this topographic effect to the mountain geometry. The experiments with the mountain higher than 750 m show the impact of topography on the error growth, while the experiments with 500-m height tend to have a similar level of the error as FLAT; and for mountains with the same height, the topographic effect of a narrower mountain tends to be clearer. This sensitivity to mountain geometry is further investigated by separately comparing the different terms in the CMDTE which represent the errors in moisture (DiLH), wind (DiKE), and temperature (DiSH) fields. The results show that mountain topography affects the growth of moisture error at the early stage of convection development regardless of the mountain height or width. The sensitivity of topographic effects on error growth to mountain geometry is mainly shown in the errors of wind and temperature.

Further analysis shows that this sensitivity to mountain geometry might result from different dynamical uncertainty in convection initiation (CI) mechanisms over mountains with different geometry. Specifically, for a higher mountain that can trigger upslope wind on the lee side of the background flow, the deep convection could be initiated by the convergence of the thermally driven upslope wind and background winds on the lee side (e.g., on the west side of the mountain in the experiments using the wind profile of the sounding data). It is considered that this process of forming deep moist convection has less uncertainty and is less sensitive to initial differences, resulting in a slower error growth at the early stage of convection development. In contrast, this CI mechanism is absent with a lower mountain; thus, the lower mountain impacts less on the error growth associated with moist convection. Similarly, the sensitivity of topographic effects to mountain width may also come from the dynamical processes. The narrower mountain builds narrower convergence and updraft area, resulting in less uncertainty for developing deep convection and thus less error growth when the convection is initiated.

The sensitivity tests turning off the microphysics parameterization support this hypothesis of the different dynamical uncertainty of CI over the mountains with different heights. When there is no moist process, a lower mountain still shows fewer decreasing effects on error growth than the higher one. In other words, the topographic effects on decreasing error growth may be less related to the microphysical processes in deep moist convection. Instead, the topographic effects are attributed to the impact of topography on the dynamical processes of CI.

The results also indicate the sensitivity of topographic effects to different flow conditions. For experiments with different background wind, the similar restraining effect of the topography on error growth is also shown in the experiments using a vertically uniform wind profile without vertical shear (NS5), while the effect is less clear in the experiments with zero background wind (U00) and vertically strong wind speed shear (U25).

The comparison of the potential temperature (θ) anomaly during the convection development in the experiments with different background winds reveals that the diabatic heating due to latent heat release may be a key component that triggers rapid error growth. For the experiments with mountain topography and zero background (U00_TOPO), the convective clouds stay at the same place in absence of the background wind to push them and keep heating the air at the same place. The diabatic heating in clouds results in the positive anomaly of temperature that provides further buoyancy forcing and facilitates the development of convective clouds and the following error growth. The differences in convection development (i.e., error) lead to more different diabatic heating and thus more differences in the continuous development of convection, resulting in positive feedback of latent heating on error growth. This positive feedback is considered to make the topographic effects on error growth unclear in the experiments without background wind.

The processes of the diabatic heating are also considered to be the reason that causes the

error to grow so rapidly after the convection continues developing that the topographic effects are only shown at the early stage of convection development. The point that diabatic heating triggers more error growth is supported by the time-height cross section of the error and θ anomaly. The analysis of the time-height cross section shows that when the θ anomaly increases to a higher level, the errors will grow more rapidly to a certain magnitude regardless of the topography settings. The twin experiments with the initial error added to potential temperature also highlight the ability of moist convection at a mature stage on triggering error growth. In these experiments, errors grow rapidly during the convection development regardless of its slower growth at the first.

In summary, the error growth triggered by thermally induced moist convection could be reduced when the intertwining of the topography and environmental flows leads to a smaller uncertainty of CI. In today's numerical models, the location and intensity of updrafts are still hard to be predicted accurately during the CI stage (Zhang et al. 2016). The results in this chapter imply that when the topography is sufficient to affect the circulation conditions and change the mechanisms of CI to a less uncertain situation, there is a chance to predict CI more accurately. However, this topographic effect could also be sensitive to other factors, such as the vertical shear of the background wind. At the same time, when convection continues growing, the error will also grow more rapidly, and the errors among experiments with different topography could become almost the same magnitude within one hour after the rapid growth start.

Chapter 4 The predictability limit of localized thunderstorms and the accompanying rainfall

The error growth properties in chaotic systems (Fig. 1.5) limit the predictability of the system. In other words, there exists an upper bound on the length of time for meaningful predictions; the bound cannot be broken by further reducing the errors in initial conditions (Lorenz 1969). In Chapter 3, we thoroughly investigated the impacts of mountain topography on error growth, mainly focusing on the early stage of convection development. We showed that topography could reduce the error growth trigged by moist convection because of the change in the convection initiation mechanism; this impact is sensitive to the mountain height and background wind. However, it is still not evident if there is a limit to predicting thermally induced thunderstorms and how topography and environmental flow impact the predictability limit. In this chapter, we investigate the predictability limit of thermally induced thunderstorms and the error growth dynamics that limit the predictability. Both the impacts of topography and background winds are investigated. Two metrics, convective moist difference total energy (CMDTE; see Section 2.4.1) and spatial correlation coefficient (SCC; see Section 2.4.2), are used to estimate the limit of predicting convective clouds and the accompanying rainfall, respectively, from different aspects. The former provides the limit of dynamically predicting instantaneous states of thunderstorms themselves at the model grid scale. The latter examines the limit of rainfall prediction from the point of view of improving the critical information on day-to-day weather forecasts.

4.1 The limit of predicting convective clouds

In this section, we examine if there is a limit to predicting the evolution of thermally induced thunderstorms and, if so, investigate possible factors that determine the limit time. The predictability limit is examined by conducting additional simulations having different amplitudes of the initial errors. The initial errors are also added at later times to assess the flow-dependent predictability. The time when initial errors reach a saturation level is usually used to indicate the loss of predictability (Dalcher and Kalnay 1987; Selz and Craig 2015; Weyn and Durran 2017; Judt et al. 2018; Zhang et al. 2019). The additional simulations are designed to examine if using a smaller initial error or initializing the simulation at a later time can extend the error saturation time, i.e., the predictability limit or the time of losing the capacity to improve predictions.

First, the comparison between FLAT and TOPO is performed. The control simulations in FLAT and TOPO are again used. The additional perturbed simulations are initialized by adding random perturbations of water vapor mixing ratio with the amplitudes 0.1 and ten times the original one of 0.01 $\mathrm{g\,kg^{-1}}$; i.e., 0.001 (denoted as P01) and 0.1 $\mathrm{g\,kg^{-1}}$ (as P10), respectively. Additional perturbed simulations are also initialized at 0800 (denoted as 08LT) and 1000 LT (as 10LT) with the same amplitude as the original one.

Figure 4.1 provides the evolution of domain-averaged CMDTE between the control simulation and these additional perturbed simulations. For all the perturbed simulations, the errors grow exponentially first and then reach saturation at a similar level. The time of reaching the saturation level is around 1300 LT, regardless of the start time of the simulation, the initial error amplitude, and the existence of the mountain or not, indicating the existence of a predictability limit. In other words, Fig. 4.1 suggests that reducing the initial error or starting the simulation at a later time brings little benefit to the prediction of convective clouds after

1300 LT. Meanwhile, topography also impacts little on this predictability limit.

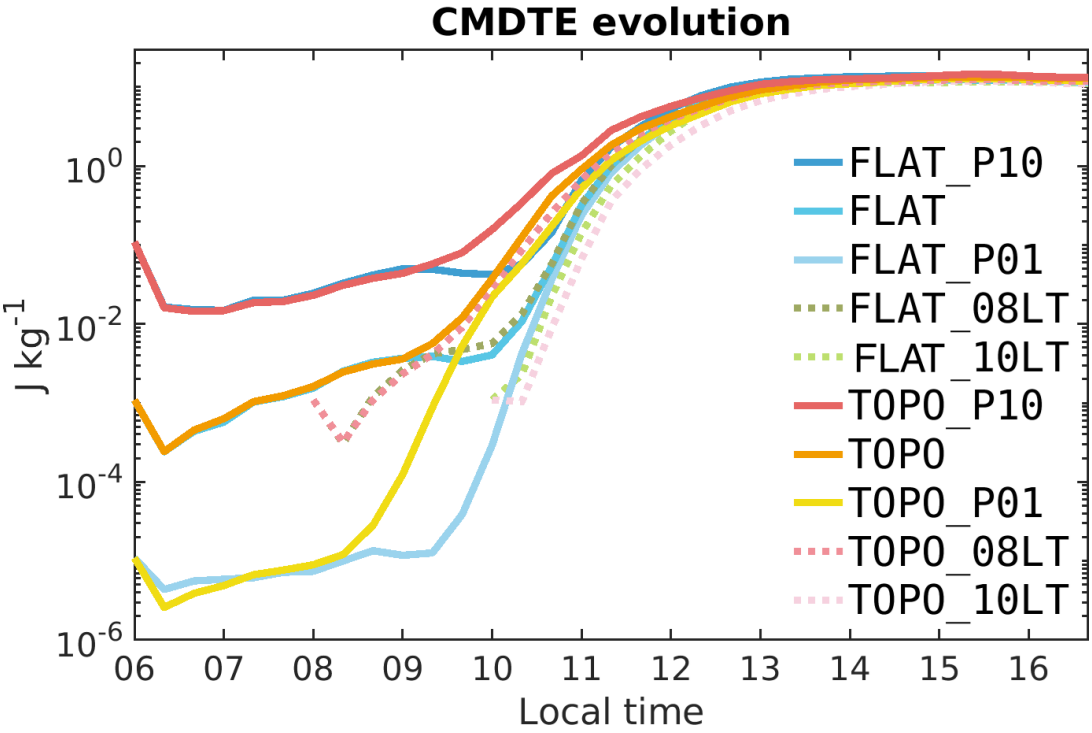

Figure 4.1 Time evolution of the domain averaged CMDTE calculated for the perturbed simulations with initial error amplitude equal to 0.1 (FLAT_P10 and TOPO_P10), 0.01 (FLAT and TOPO; the original ones), and 0.001 (FLAT_P01 and TOPO_P01) g kg^{-1} started at 0600 LT, and equal to 0.01 g kg^{-1} but started at 0800 LT (FLAT_08LT and TOPO_08LT) and 1000 LT (FLAT_10LT and TOPO_10LT). The results denoted by the legend started from "FLAT" ("TOPO") shared the same control simulation in FLAT (TOPO).

In general, Fig. 4.1 shows typical features of the error growth in a chaotic system with limited predictability, i.e., exponential growth and error saturation. The property that smaller initial errors lead to more rapid growth is consistent with previous studies (e.g., Zhang et al. 2003). However, it is worth noting that the results also show a strongly flow-dependent error growth rate which varies dramatically within only several hours, different from the typical error growth properties at synoptic scales. For instance, Zhang et al. (2019) showed that the simple error growth model of Eq. (1.1) with the constant error growth rate is well applicable

to describe the error growth at synoptic scales within two weeks. The time scale of the changes in the error growth rate at synoptic scales is generally seasonal, i.e., α is different for different seasons but can be regarded as a constant within several weeks. In contrast, the results in Fig. 4.1 show rapid changes in the error growth rate in only several hours. Therefore, although the same error amplitude leads to the same error growth rate at synoptic scales according to Eq. (1.1) with the constant α, this is not the case at convective scales. The underlying dynamics at convective scales is different from that at synoptic scales and is variable quickly in time, and therefore the simple error growth model with constant α may not be used for the convective-scale phenomena. As a result, the same error amplitude at different times does not necessarily lead to the same error growth. The growth of the error in FLAT_P01, for example, is more rapid than that in TOPO_P01 when they reach the same amplitude of, e.g., 10^{-2}. Compared with TOPO_P01, the error in FLAT_P01 reaches 10^{-2} at a later time when the underlying dynamics might become more unstable with more vigorous convective activity; thus, the error grows more rapidly.

Figure 4.1 demonstrates the limit of better predicting thermally induced thunderstorms before their initiation. The simulations started at later times also have error saturating at 1300 LT, resulting in an even shorter time range in which predictions could be improved. The only exception to the error saturation time is the result of TOPO_10LT. The error of TOPO_10LT is smaller than all others in Fig. 4.1 until around 1500 LT, suggesting a later saturation time. Quantitatively speaking, at 1300 LT, for example, the absolute magnitude of the domain-averaged CMDTE in TOPO_10LT is around 80 % of the error in TOPO_P01, which is initialized at an earlier time (0600 LT) but with only 10 % of the initial error amplitude compared with TOPO_10LT. The later error saturation time in TOPO_10LT might be related to the already initiated convective clouds in TOPO at 1000 LT (see Figs. 3.2g-l). It is implied that the predictability of thunderstorms might be longer when starting the prediction after

convection initiation, highlighting the difficulty of predicting thunderstorms before they occur.

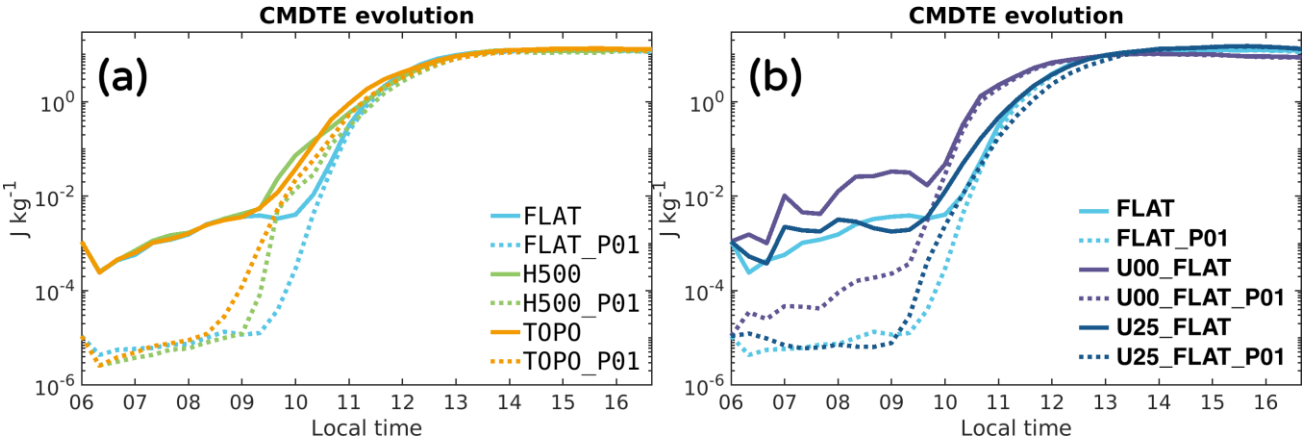

Figure 4.2 Similar to Fig. 4.1 but for the perturbed simulations with initial error amplitude of the original ones and equal to 0.001 $g\,kg^{-1}$ (denoted by "_P01") for the experiments with (a) different topography and (b) different background winds.

After confirming the existence of the predictability limit of thermally induced localized thunderstorms, we further assess the impact of mountain geometry and background wind on this predictability limit. The experiments with lower mountain height (H500) and different background winds (U00 and U25) are used, and the additional perturbed simulations initialized with 0.1 times the error magnitude (P01) are conducted. In the experiments with the original wind profile from the sounding data (Fig. 4.2a), errors growing from different initial amplitudes saturate at a similar time regardless of the topography settings. On the other hand, for the experiments with different background winds and no mountain topography (Fig. 4.2b), the error saturation time is characterized by the conditions of background winds. Specifically, the time when the initial errors of different amplitudes reach the same level implies the loss of predictability, i.e., reducing initial error cannot improve the prediction accuracy after that time. This time of predictability limit varies among the experiments with different background winds. In U25_FLAT, the saturation time is later than that in U00_FLAT, implying a longer

predictable range during which there is potential to improve the prediction. The result of U25_FLAT is roughly consistent with Weyn and Durran (2017), who showed that the mesoscale convective systems under stronger vertical wind shear could be more predictable than those in environments with weaker shear. Overall, Fig. 4.2 suggests that topography impacts little on the timing of losing predictability for thermally induced thunderstorms. In contrast, the predictability limit of thunderstorms differs under different environmental flows.

To further assess the processes that result in the different sensitivity of predictability to topography and environmental flow shown in Fig. 4.2, we examine the evolution of convective activity, represented by the cloud grid ratio (CGR), together with the error growth and the error growth rate λ (see Section 2.4.1). Since we already confirmed the existence of the predictability limit by using different perturbed simulations in Figs. 4.1 and 4.2, here we only compare the errors from the perturbed simulations started at 0600 LT with the initial error amplitude of 0.01 g kg^{-1} (i.e., the original one used in Chapter 3).

Figure 4.3 links the time of predictability limit with the convective activity. For experiments with the original wind profile but different topography (Fig. 4.3a), the convective activity reaches a maximum level at a similar time; the error growth of these experiments also slows down and reaches saturation at the same time. The error growth rate (λ) converges to a similar value at around 1300 LT for all experiments in Fig. 4.3a despite their differences before 1200 LT. In comparison, Fig. 4.3b shows that the convective activities in the experiments with different background winds reach the maximum at different times. These different times of the maximum convective activity are considered to indicate the time of the predictability limit.

The evolution of convective activity in Fig. 4.3, represented by the domain-averaged CGR, is determined by the overall convective activity over the computational domain. Figure 4.3a suggests that the mountain topography used here, which only partially occupies the domain, affects little on this overall convective activity after 1100 LT. Consequently, the

experiments with different topography in Fig. 4.3a have a similar time of the maximum convective activity. The similar time of maximum convective activity then leads to a similar time of predictability limit. For the same reason, because environmental flows could largely impact convection development (Muller 2013; Fu and Guo 2012), the experiments with different background winds show various maximum convective activity times, resulting in different times of predictability limit (Fig. 4.3b). In addition, the experiment with and without topography in Fig. 4.3b show much less difference for both the times of maximum convective activity and the predictability limit compared with the differences among the experiments with different background winds, further emphasizing the impact of environmental flows on the predictability limit is more distinguished than that of topography.

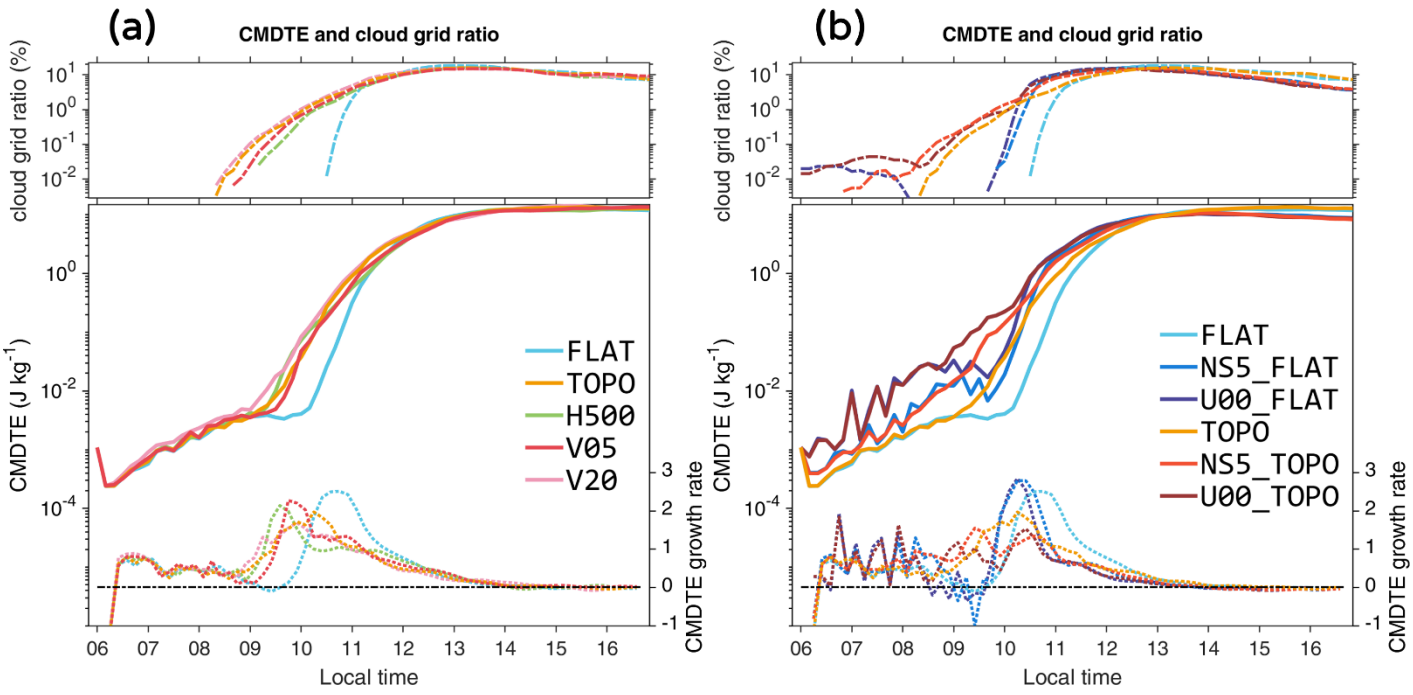

Figure 4.3 Time evolution of the CGR in the control simulation (upper), the CMDTE (solid curves in the bottom panel, left axis), and the error growth rate (dotted curves in the bottom panel, right axis) of the experiments with different (a) topography and (b) background winds. The TOPO and FLAT in (a) and (b) are exactly the same.

Overall, Fig. 4.3 suggests that the time of the maximum convective activity determines the time of losing predictability. Because environmental flows have greater effects on convection development, they impact the predictability limit time more than the mountain topography does. Figure 4.3 also highlights the feature of the strongly flow-dependent predictability at convective scales. In the case of thermally induced thunderstorms, the error growth rate (see dotted curves in Fig. 4.3) could change quickly with time as the convective activity becomes more vigorous in a few hours. As a result, errors grow even more rapidly towards the noon time and reach to saturation levels at the same time after the convective activity becomes the maximum. This error growth properties limit the space for improving the prediction afternoon even with a smaller initial error or starting the simulations at later times (Fig. 4.1).

4.2 The predictability limit of spatial rainfall pattern

Although temperature and wind are important atmospheric variables for evaluating the accuracy of NWPs, rainfall information is regarded as a combined result of dynamical and microphysical processes in the atmosphere. It is essential to evaluate the rainfall prediction to assess the ability of NWP. In addition, rainfall products are crucial to people's daily lives. Thus, from the viewpoint of providing better NWP, evaluating the limit of predicting rainfall is necessary. Here we focus on the rainfall patterns by using the spatial correlation coefficient (SCC; see Section 2.4.2) between the rainfalls of control and perturbed simulations to examine if the predictability of the rainfall brought by thunderstorms is also limited. The impacts of topography and environment flows are also assessed. As a reference of the rainfall pattern in each experiment, Fig. 4.4 provides the horizontal distribution of 12-h accumulated rainfall in the experiments compared in this section. Please also refer to Fig. 3.3 for 6-h accumulated rainfall in FLAT and TOPO.

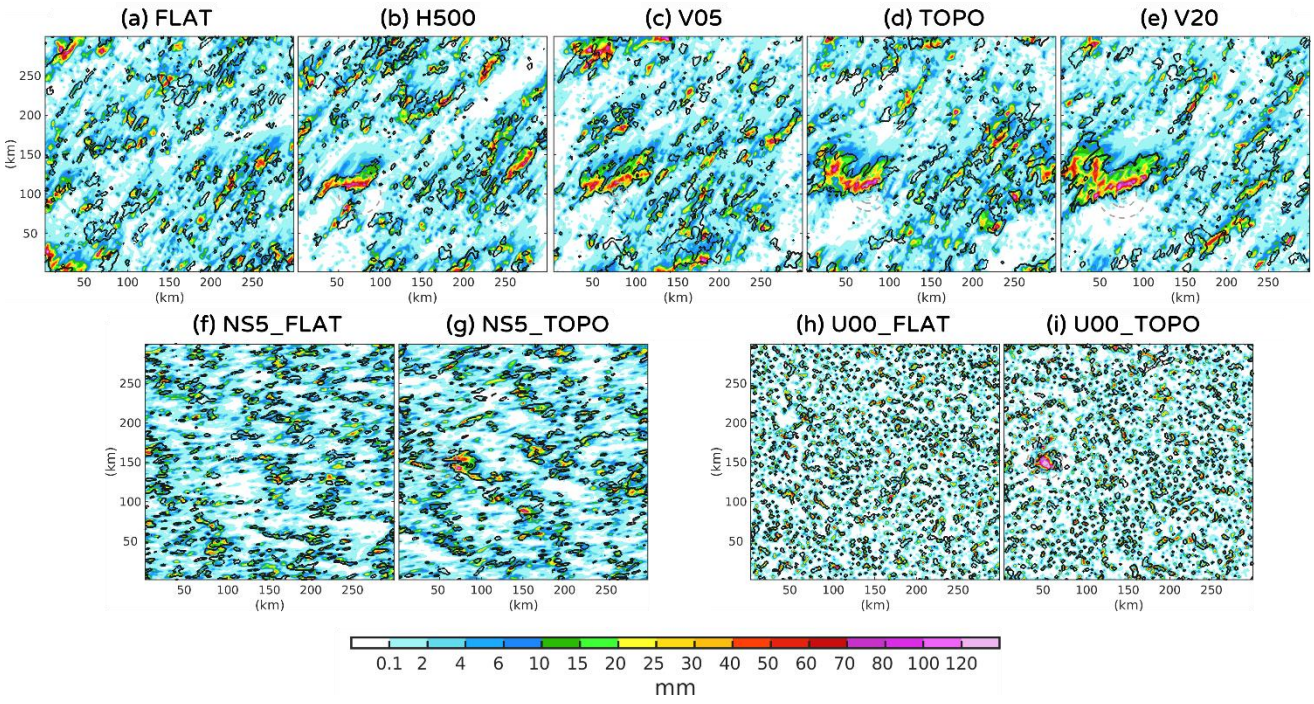

Figure 4.4 The 12-h accumulated rainfall (from 0700 LT) of the control (color shaded) and perturbed (black contour, 10mm) simulations in (a) FLAT, (b) H500, (c) V05, (d) TOPO, (e) V20, (f) NS5_FLAT, (g) NS5_TOPO, (h) U00_FLAT, and (i) U00_TOPO.

First, we compare the results of the experiments with different topography under the original wind profile from the sounding data. For the sake of robustness, for each experiment, four additional perturbed simulations against the control simulation were conducted by adding perturbations with the amplitude of 0.01 $\mathrm{g\,kg^{-1}}$ at 0600 LT (the same as the original one) using different random seeds. Namely, there are five perturbed simulations with the same start time and the amplitude of initial error in each experiment. The SCC scores are calculated separately between the control simulation and these five perturbed simulations.

For the hourly rainfall, which is the rainfall during the next one hour of the time depicted in Fig. 4.5a, the SCC scores decrease rapidly after 1100 LT, regardless of the topography settings. In the afternoon, the SCCs in all the experiments fluctuate around low values between 0 and 0.4, suggesting that there is no forecasting skill in the afternoon for all the experiments.

Figure 4.5a suggests that topography might also have little impact on the predictability limit of hourly rainfall. In addition, most experiments have SCC values dropping below 0.4 at around 1300 LT, corresponding to the error saturation time of CMDTE, which implies that the predictability limit time of hourly rainfall is similar to the limit of predicting convective clouds. In other words, it is also difficult to have confident hourly rainfall prediction for thunderstorms after the convective activity reaches maximum.

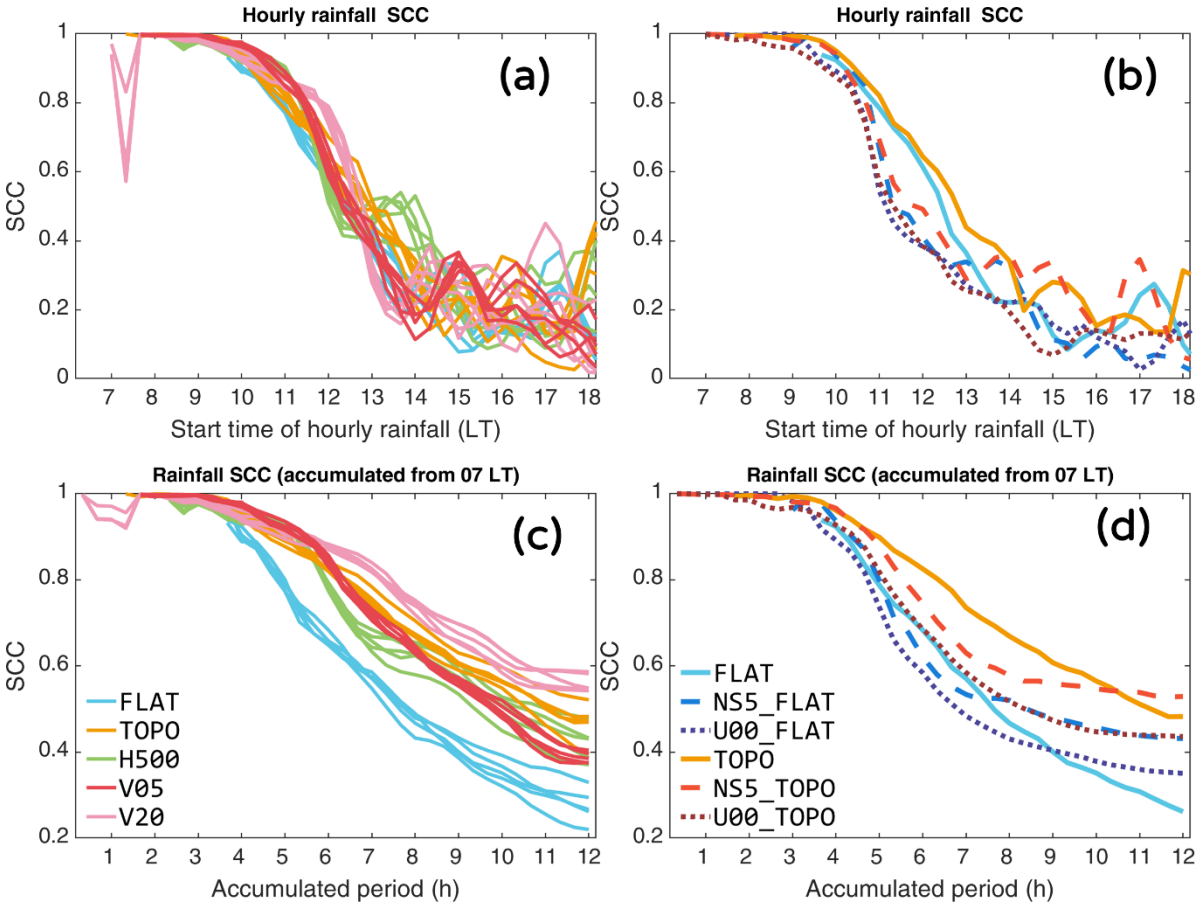

Figure 4.5 The SCCs between control and perturbed simulations of (a), (b) hourly rainfall and (c), (d) rainfall accumulated from 0700 LT for experiments with different (a), (c) topography and (b), (d) background winds. The SCCs are calculated every ten minutes. In (a) and (b), the x-axis shows the start time of the hourly rainfall (i.e., rainfall during 0700-0800 LT, 0710-0810 LT, etc.). The SCCs depicted at x=7, for example, are the scores of the hourly rainfall in 0700-0800 LT. In (c) and (d), the SCCs are depicted for the rainfall during 0700-0710, 0700-0720, etc. The SCCs at x=1, for example, are the scores of rainfall accumulated from 0700 LT for one hour (i.e., 0700-0800 LT).

For the experiments with different background winds, no additional perturbed simulation is performed, and the SCCs are calculated between the control and the original perturbed simulations. In spite of that, the hourly rainfall SCCs of the experiments with different background winds (Fig. 4.5b) seem to suggest similar properties of the predictability limit. The SCCs decrease rapidly during 1000 to 1300 LT and eventually fluctuate between values of 0 and 0.3. Meanwhile, there are more evident differences in the scores among the experiments with different background winds than among the experiments with different topography settings. For example, TOPO and FLAT have similar SCCs until around 1200 LT, while the SCCs between TOPO and NS5_TOPO (or U00_TOPO) quickly depart after 1000 LT. The results in Fig. 4.5a and 4.5b are consistent with the error growth properties shown by CMDTE (Fig. 4.3), indicating that the background wind has a greater impact on the predictability limit than topography does.

On the other hand, results show that topography has a greater impact on the accumulated rainfall over several hours. As shown in Fig. 4.5c, FLAT has notably lower SCCs than all the experiments with mountain topography for the rainfall accumulated for time periods longer than four hours. In the afternoon, the SCCs of the accumulated rainfall differ distinctly among different experiments, unlike the SCCs of hourly rainfall (c.f. Figs. 4.5a, b). Among the experiments in Fig. 4.5c, V20 shows the highest scores when the accumulation period is longer than 6 hours. Even in the lower mountain case, H500, which showed smaller topographic effects on the error growth in Chapter 3, the SCC scores are higher than those in FLAT throughout the accumulated period.

Such topographic effects are also examined for the experiments with different background winds (Fig. 4.5d). Unlike the comparison in terms of hourly rainfall or CMDTE (which suggests that background wind has a greater impact than topography), in Fig. 4.5d, the experiments with topography have higher SCC scores than those without topography.

Meanwhile, the differences in the SCC scores between U00_FLAT and U00_TOPO seem to be smaller than those between FLAT and TOPO or between NS5_FLAT and NS5_TOPO. In other words, Fig. 4.5d suggests a clear impact of topography on the several-hour accumulation rainfall prediction; at the same time, the degree of this topographic effect is also sensitive to environmental flows, similar to the conclusion in Chapter 3.

Overall, Fig. 4.5 shows the limit of improving hourly rainfall prediction in the afternoon, while the accumulated rainfall for several hours might be better predicted with the existence of mountain topography. There are two possible reasons for the obvious topographic effect on the predictability of the several-hour accumulation rainfall.

One is because the experiments with topography do have higher rainfall scores at the early stage of convection development regardless of the mountain geometry (see 0700-1100 LT in Fig. 4.5a). The topographic effects on the error growth of moisture are evident regardless of the mountain geometry (see Figs. 3.12 and 3.13 and their discussion in Chapter 3), leading to fewer errors of rainfall distribution in all the experiments with mountain topography. In the morning, convective clouds developed vigorously over the mountain area and generated heavy rainfall having a similar spatial pattern between the control and perturbed simulations (see Figs. 3.3 and 4.4). Therefore, when accumulating the rainfall until the afternoon, the similar spatial pattern of rainfall over the mountain area keeps the SCC scores higher in the experiments with topography than without topography.

The other reason is the constraint of the mountain on the domain-scale rainfall distribution. While the exact location and structure of individual convective clouds are almost unpredictable in the afternoon, the convective clouds in the experiments with topography overall develop only outside the mountain area in the afternoon (Fig. 3.2j). Thus, the large-scale distribution of rainfall could be restrained by the mountain. In other words, topography impacts the predictability of rainfall at the domain scale. The accumulation of rainfall smooths

out the smaller-scale patterns; therefore, the impact of topography clearly appears.

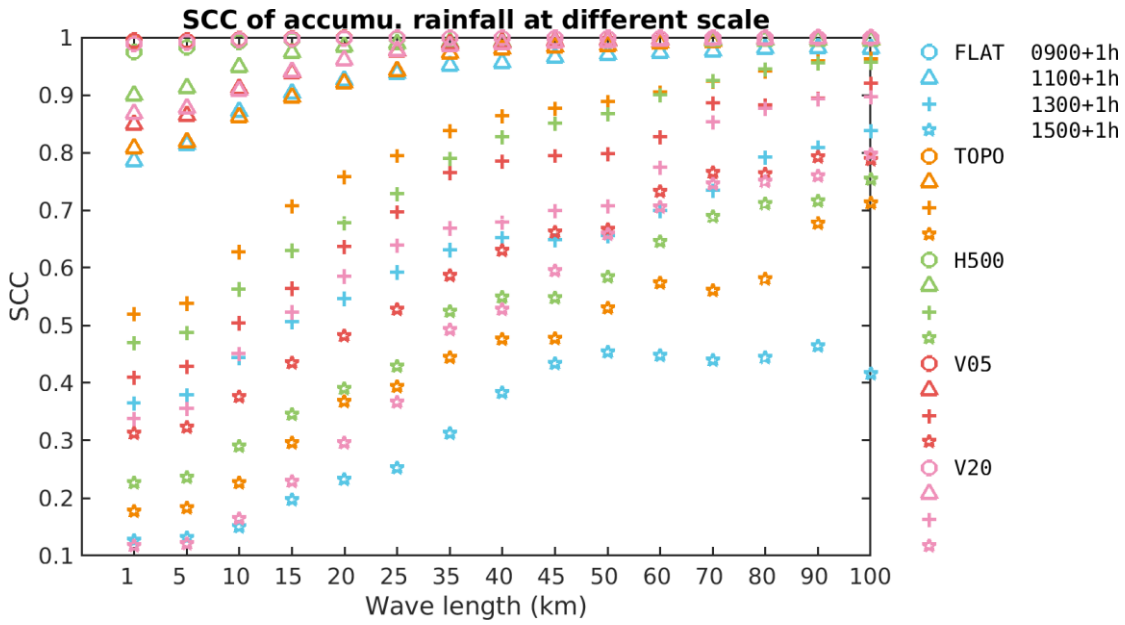

Figure 4.6 The SCCs of the hourly rainfall at 0900 (circles), 1100 (triangles), 1300 (plus sign), and 1500 (stars) LT calculated from the rainfall between control and perturbed simulations whose smaller scale characteristic below a specific scale (depicted by x-axis) is filtered.

The impact of topography on the domain-scale rainfall prediction can be shown by the SCC of low-pass filtered rainfall distribution (Fig. 4.6, see Section 2.4.2 for the detail of the calculation). In Fig. 4.6, the SCC scores at the leftmost point on the x-axis (1 km, the model grid spacing) are the same as those without filtering (Figs. 4.5a, b). The hourly rainfall scores are similar at different scales in the morning. In the afternoon, the rainfall scores at smaller scales decrease greatly while those at the larger scales remain exceeding about 0.4. For example, at 1500 LT, while all experiments have SCCs lower than 0.4 at the 1-km scale, only the experiments with topography have SCCs higher than 0.6 at scales larger than 80 km. The results in Fig. 4.6 are similar to those in Bachmann et al. (2019), who indicated the impact of topography on the predictability limit of rainfall by using scale-dependent rainfall scores. For

example, if the SCC value of 0.8 is assumed to be a reliable prediction threshold, the hourly rainfall at this reliable threshold at 1300 LT is seen at a scale of 100 km in FLAT while is found at a scale of about 25 km in TOPO, suggesting a better prediction at finer scales in TOPO.

4.3 Summary and discussion

In this chapter, we investigated predictability limit by using identical twin experiments with different topography and environmental flow conditions. Firstly, the predictability limit of thermally induced localized thunderstorms is examined by comparing the convective moist difference total energy (CMDTE). Secondly, we assessed the predictability limit of the accompanying rainfall distribution by using the spatial correlation coefficient (SCC).

The CMDTE of perturbed simulations with different initial error amplitude and start time are first compared. The results show that there is a clear predictability limit at which reducing initial error or starting the simulation later does not extend the time of the error saturation. The error growth rate is strongly flow-dependent and changes dramatically with time, which can be linked to the activity of moist convection. The error growth becomes more rapid with the convection development, and in the end, the errors saturate at the time of maximum convective activity. Different from synoptic scales, in the present case of thermally induced thunderstorms, the underlying dynamics change so rapidly that slower error growth at first does not necessarily result in longer predictability. Thus, because of the little impacts on the maximum convective activity, mountain topography has little impact on the predictability limit even if the error growth is mitigated at the early stage of convection development.

On the other hand, the experiments with different background winds show different error saturation times, implying the changes in predictability limit. In these experiments, the error saturation time also coincides with the maximum convective activity time, which is different among the experiments with different background winds. It is considered that the maximum

convective activity time determines the limit of predicting thermally induced thunderstorms in a diurnal cycle. Thus, the environmental flow, which affects the convection development and the time of the maximum convective activity, affects the time of losing predictability.

Then, the predictability of rainfall is assessed by using SCCs of rainfall distribution. For hourly rainfall, the scores dropped rapidly and ended in no forecasting skill in the afternoon regardless of topography settings. Similar to the comparison using CMDTE, the environmental flow shows a greater impact on the hourly rainfall predictions than the topography does. On the other hand, the scores of several-hours accumulation rainfall show more substantial effects from the mountain topography. For experiments with original sounding wind profile, all the experiments with topography have higher scores of 12-h accumulated rainfall than the cases without topography. In addition, for experiments with different background winds, the impact of the topography on several-hour accumulated rainfall is greater than that of environmental flow. This topographic effect on the accumulated rainfall prediction might come from the impact of the mountain on the error of the moisture field and the rainfall distribution at the domain scale.

The score of hourly rainfall and the evolution of CMDTE reveal the difficulty of dynamically predicting the instantaneous location and intensity of moist convection after it develops to a mature stage. The mountain topography may affect little on this limit. On the other hand, the prediction of long-term (3–12 h) accumulated rainfall distribution seems to be affected more by mountain topography. The clearer topographic effects on accumulation rainfall imply that we may be more confident in predicting accumulated rainfall over the mountainous areas.

Topography was considered to enhance the atmospheric predictability (Vukicevic and Errico 1990; Boer 1994; Kalnay 2002). For mesoscale phenomena, Carbone et al. 2002 pointed out that convective systems tend to have larger characteristic scales under topographic

forcing and expected that the rainfall produced by those convective systems might have a longer predictable time length. The results of this study imply that the location, intensity, and detailed internal structure of convective clouds are still difficult to predict at the 1-km scale even if convection organizes to a larger scale and exists for a longer time. Nevertheless, it may be easier to predict the rainfall brought by large-organized convective systems over mountainous areas at meso-β scales, especially for rainfall accumulated for several hours.

Meanwhile, we must notice that even with better initial conditions or model configuration, the chaotic nature of thunderstorms might limit the space for improving instantaneous deterministic dynamical predictions. Instead of further improving deterministic dynamical predictions, we can put more efforts into developing ensemble prediction systems that better represent the uncertainty of convection development. The efforts could also be put to statistically analyze the environmental conditions favored by deep moist convection to guide the occurrence of thunderstorms (e.g., Lin et al. 2012; Chen et al. 2016; Chang et al. 2017) or even to indicate the flow-dependent predictability of a specific day. Further studies with more realistic model configurations would be desired for providing insights into the real world's daily weather prediction.

Chapter 5 Conclusions

The prediction of high-impact weather phenomena such as thunderstorms is essential and affects people's decisions on their daily lives and commercial activities. While the numerical weather prediction (NWP) models are continuously being improved, predicting thermally induced localized thunderstorms in warm seasons is still a challenging task today. Thunderstorms are considered to have a predictable time length short of a few hours, especially for the localized ones whose characteristic scale is relatively small. In addition to improving the forecast skills of the NWP models, it is also important to understand the limit of predictability to develop more efficient strategies for weather prediction. Although previous studies have indicated the low predictability of thunderstorms, relatively less literature has focused on the thermally induced thunderstorms characterized by diurnal cycles. The impact of topography on predictability is also not well elaborated. Further studies are still needed to advance the understanding of predictability at convective scales.

This study investigated the impact of topography and environmental flow conditions on both error growth and predictability limit of thermally induced localized thunderstorms. The simulations of thunderstorms were conducted with the Weather Research and Forecast (WRF) model in an idealized framework under different conditions of topography and environmental flow. Identical twin experiments under a perfect model assumption were performed using the simulations of thunderstorms to assess the error growth dynamics and predictability.

In Chapter 3, the simulations of thunderstorms in all experiments exhibited clear diurnal cycles of domain-average rainfall and surface-air temperature. Meanwhile, convective clouds still indicate a variety in the distribution, horizontal extents, and orientations in different experiments. Then, we used the twin experiments to investigate the properties of the error

growth triggered by moist convection. The experiments showed that the error grows rapidly with the development of moist convection. Thus, the spatial distribution, temporal evolution, and spectral properties of the error reflect the features of the simulated moist convection. This is consistent with previous studies (e.g., Zhang et al. 2003; Zhang et al. 2016).

Previous studies paid little attention to the impact of topography on the error growth associated with moist convection. Here we compared the error in the twin experiments with and without mountain topography to clarify the topographic effects on error growth for the first time. We showed that mountain topography could reduce the error growth triggered by moist convection during the convection initiation. This topographic effect is found to be sensitive to mountain geometry and background flow conditions. Further analysis revealed that the topographic effect on error growth could be attributed to less uncertainty in the mechanisms of convection initiation. Specifically, the convergence of the background wind and thermally driven upslope wind facilitates upward motion in a fixed area, resulting in less uncertainty of forming deep convection. Therefore, the effect of topography on reducing error growth only acts under specific conditions when the interaction of the background flow and heated mountain leads to the less uncertain situation of convection initiation and development.

The comparison of the error on different fields of moisture, wind, and temperature also revealed that different atmospheric variables respond differently to the topographic effect on error growth. For the error on the moisture field, topography showed impacts at the early stage of convection development regardless of the mountain geometry or flow conditions. In contrast, the growth of the error on wind fields could only be reduced when the mountain geometry is sufficient to drive the circulation for the convection initiation. This finding is expected to provide a new insight into NWPs when dealing with the error in different terms of atmospheric variables over mountainous areas. For example, over mountainous areas, the wind fields in models might need to be updated by assimilating observations more frequently than

the moisture field.

The impact of mountain topography on the error growth becomes less clear at a mature stage of convection development when the diabatic heating from latent heat release in clouds further enhances the convective activity and leads to more error growth. The rapid error growth in all experiments reaches saturation after a few hours of the convection development, indicating a limit of predictability. The predictability of thunderstorms is further investigated in Chapter 4.

The predictability of thermally induced localized thunderstorms characterized by diurnal cycles received less attention in previous studies. Our results revealed that the error reaches saturation after the convective activity reaches a maximum, indicating the failure of predicting thunderstorms at this saturation time, regardless of initial error amplitude or the start time of the simulation. This result also implies that the predictability limit of the thunderstorms in a diurnal cycle critically depends on the time of maximum convective activity and cannot be extended by using a smaller initial error or starting the prediction at a later time. Because relatively little literature has focused on the predictability of thunderstorms in a diurnal cycle, our new findings advance the knowledge of predicting thermally induced thunderstorms which are commonly seen in warm seasons. In particular, starting the numerical prediction at a later time may not be able to improve the deterministic forecast of thermally induced thunderstorms beyond the time of its maximum activity. In addition, the result showed that environmental flow has greater impacts on this predictability limit determined by the time of maximum convective activity than the mountain topography does, because environmental flow affects the properties of convection development and thus the maximum convective activity time.

Then, from the viewpoint of providing critical information on day-to-day forecasts, the comparison of spatial rainfall patterns revealed the different impacts of topography on predicting hourly rainfall and accumulated rainfall for several hours over mountain areas. The

results showed the failure of hourly rainfall prediction quickly in a few hours regardless of the topography conditions. On the other hand, the prediction of the rainfall accumulated for several hours showed clearer impacts from mountain topography. The several-hour accumulated rainfall has higher scores in the experiments with than without mountain topography regardless of environmental flows. The higher scores of the accumulated rainfall with mountain topography are a result of the constraint from the mountain on the domain scale rainfall distribution. The findings here enriched the understanding of the rainfall prediction over mountainous areas. Although previous studies indicated that topography could increase the predictability of convective rainfall (Bachmann et al. 2019, 2020), our results suggested that this advantage may not be able to apply to all aspects of rainfall prediction. The predictability of hourly rainfall at model grid-scale (1 km in this study) may not be benefited from the existence of mountain topography because of the failure of models to predict the exact location and strength of thunderstorms.

In general, error growth and predictability are highly related to the properties of moist convection in interest. Thus, the factors that change the mechanisms during the convection initiation and development could also result in different error growth and predictability. Topography mitigates the error growth during the convection initiation when the topography can trigger convection in a way with less uncertainty. On the other hand, environmental flows impact the duration of the convection life cycles, which leads to different limit times of predictability. While topography impacts less on the instantaneous prediction of thunderstorms after moist convection grows to a mature stage, its restraint on moisture field and large-scale rainfall distribution leads to a more reliable prediction of several-hours accumulated rainfall. These findings advanced the understanding of the predictability at convective scales and are expected to provide insight into the interpretation of predictions of thunderstorms in NWP models.

Publication List

This thesis is based on the following journal papers.

1. The Impact of Topography on the Initial Error Growth Associated with Moist Convection, Scientific Online Letters on the Atmosphere (SOLA), 17, 134-139, doi.org/10.2151/sola.2021-024 (advance online publication in June 2021; released in July 2021).
   WU, Pin-Ying, and Tetsuya TAKEMI

2. The Impacts of Topography and Environmental Flow Conditions on the Predictability of Localized Thunderstorms and the Associated Error Growth in a Diurnal Cycle, Journal of the Atmospheric Sciences (in revision).
   WU, Pin-Ying, and Tetsuya TAKEMI

The author was responsible in conducting above works independently under the supervision of Dr. Tetsuya Takemi.

Another publication by the author as a reference is as follows

3. Convective-Scale Sampling Error and Its Impact on the Ensemble Radar Data Assimilation System: A Case Study of a Heavy Rainfall Event on 16 June 2008 in Taiwan. Monthly Weather Review, 148, 3631–3652, doi.org/10.1175/MWR-D-19-0319.1
   WU, Pin-Ying, Shu-Chih YANG, Chih-Chien TSAI, and Hsiang-Wen CHENG

Acknowledgements

First and foremost, I would like to express my deepest thank to my supervisor, Prof. Tetsuya Takemi, for his guidance and support in all aspects. Thanks for his encouragement towards conference attendance, where I have benefitted a lot through meaningful discussions with other researchers.

I would also like to thank the committee for patiently reading my thesis and giving constructive comments and suggestions, which considerably helped improve this work.

Thanks to Prof. Emeritus Hirohiko Ishikawa for his generous support on the conference attendance and helpful comments at every seminar. I would also like to thank Prof. Takeshi Enomoto for always being welcome to any discussion in which I have gotten lots of valuable advice on both research and career.

I am also grateful to Dr. Takuya Kawabata in Meteorological Research Institute and Dr. Kazuo Saito in Japan Meteorological Business Support Center for their beneficial discussion in conferences. I feel deep gratitude towards their kind supporting and understanding for me to spend the time to finish the thesis. Thanks also to Dr. Takuya Kawabata for his valuable advice and discussion on the revision of the thesis.

Thanks to the American Meteorological Society, John Wiley & Sons, Inc., and the Meteorological Society of Japan for permitting the reuse of their copyrighted works in this thesis.

I wish to thank Ms. Yoshiko Toda for her support on all the administrative matters and the warm words of encouragement during daily chatting. A lot of thanks to all other members of Severe Storm Lab and Climate Environment Lab in Disaster Prevention Research Institute

who have been excellent mentors, companions, and friends. Thank you for helping me get used to life in Japan, having meaningful discussions, studying, and having fun together. I have enjoyed being part of this community.

I am grateful to Watanuki International Scholarship Foundation for their generous financial support, which covers most parts of the living expenses in Japan and the tuition fee during the PhD program. I was also supported by the scholarship in fiscal year 2021 from the fund of Graduate School of Science, Kyoto University.

Thanks to YP for always being a friend, giving advice, and encouraging me during all the hard times. Finally, I would like to thank my parents for supporting and understanding me being in another country without being home for such a long time.

Reference

Akaeda, K., J. Reisner, and D. Parsons, 1995: The role of mesoscale and topographically induced circulations in initiating a flash flood observed during the TAMEX project. *Mon. Wea. Rev.*, **123**, 1720–1739, https://doi.org/10.1175/1520-0493(1995)123<1720:TROMAT>2.0.CO;2.

Arakawa, A., and V. R. Lamb, 1977: Computational design of the basic dynamical processes of the UCLA general circulation model. *Methods Comput. Phys.*, **17**, Academic Press, 173–265.

Bachmann, K., C. Keil, G. C. Craig, M. Weissmann, and C. A. Welzbacher, 2020: Predictability of deep convection in idealized and operational forecasts: Effects of radar data assimilation, orography, and synoptic weather regime. *Mon. Wea. Rev.*, **148**, 63–81, https://doi.org/10.1175/MWR-D-19-0045.1.

——, ——, and M. Weissmann, 2019: Impact of radar data assimilation and orography on predictability of deep convection. *Quart. J. Roy. Meteor. Soc.*, **145**, 117–130, https://doi.org/10.1002/qj.3412.

Banta, R. M., 1984: Daytime boundary-layer evolution over mountainous terrain. Part 1: Observations of the dry circulations. *Mon. Wea. Rev.*, **112**, 340–356, https://doi.org/10.1175/1520-0493(1984)112<0340:DBLEOM>2.0.CO;2.

——, and C. Barker Schaaf, 1987: Thunderstorm genesis zones in the Colorado Rocky mountains as determined by traceback of geosynchronous satellite images. *Mon. Wea. Rev.*, **115**, 463–476, https://doi.org/10.1175/1520-0493(1987)115<0463:TGZITC>2.0.CO;2.

Barthlott, C., U. Corsmeier, C. Meißner, F. Braun, and C. Kottmeier, 2006: The influence of mesoscale circulation systems on triggering convective cells over complex terrain. *Atmos. Res.*, **81**, 150–175, https://doi.org/10.1016/j.atmosres.2005.11.010.

Bei, N., and F. Zhang, 2007: Impacts of initial condition errors on mesoscale predictability of heavy precipitation along the Mei-yu front of China. *Quart. J. Roy. Meteor. Soc.*, **133**, 83–99, https://doi.org/10.1002/qj.20.

——, and ——, 2014: Mesoscale predictability of moist baroclinic waves: Variable and scale-dependent error growth. *Adv. Atmos. Sci.*, **31**, 995–1008, https://doi.org/10.1007/s00376-014-3191-7.

Bierdel, L., T. Selz, and G. C. Craig, 2018: Theoretical aspects of upscale error growth on the mesoscales: Idealized numerical simulations. *Quart. J. Roy. Meteor. Soc.*, **144**, 682–694, https://doi.org/10.1002/qj.3236.

Boer, G. J., 1994: Predictability regimes in atmospheric flow. *Mon. Wea. Rev.*, **122**, 2285–2295, https://doi.org/10.1175/1520-0493(1994)122<2285:PRIAF>2.0.CO;2.

Bjerknes, V., 1904: Das Problem der Wettervorhersage, betrachtet vom Standpunkte der Mechanik und der Physik. *Meteor. Z.*, **21**, 1–7. (English translation by Y. Mintz, 1954: The problem of weather forecasting as a problem in mechanics and physics. Reprinted in Shapiro and Grøna°s (1999), 1–4.)

Boffetta, G., A. Celani, A. Crisanti, and A. Vulpiani, 1997: Predictability in two-dimensional decaying turbulence. *Phys. Fluids*, **9**, 724–734, https://doi.org/10.1063/1.869227.

——, and S. Musacchio, 2017: Chaos and predictability of homogeneous-isotropic turbulence. *Phys. Rev. Lett.*, **119**, 54102, https://doi.org/10.1103/PhysRevLett.119.054102.

Bryan, G. H., J. C. Wyngaard, and J. M. Fritsch, 2003: Resolution requirements for the simulation of deep moist convection. *Mon. Wea. Rev.*, **131**, 2394–2416, https://doi.org/10.1175/1520-0493(2003)131<2394:RRFTSO>2.0.CO;2.

Buizza, R., and M. Leutbecher, 2015: The forecast skill horizon. *Quart. J. Roy. Meteor. Soc.*, **141**, 3366–3382, https://doi.org/10.1002/qj.2619.

Carbone, R. E., and J. D. Tuttle, D. A. Ahijevych, and S. B. Trier, 2002: Inferences of predictability associated with warm season precipitation episodes. *J. Atmos. Sci.*, **59**, 2033–2056, https://doi.org/10.1175/1520-0469(2002)059<2033:IOPAWW>2.0.CO;2.

——, W. A. Cooper, and W.-C. Lee, 1995: Forcing of flow reversal along the windward slopes of Hawaii. *Mon. Wea. Rev.*, **123**, 3466–3480, https://doi.org/10.1175/1520-0493(1995)123<3466:FOFRAT>2.0.CO;2.

Chang, H.-L., B. G. Brown, P.-S. Chu, Y.-C. Liou, and W.-H. Wang, 2017: Nowcast guidance of afternoon convection initiation for Taiwan. *Wea. Forecasting*, **32**, 1801–1817, https://doi.org/10.1175/WAF-D-16-0224.1.

Changnon, S. A., 2001: Damaging thunderstorm activity in the United States. *Bull. Amer. Meteor. Soc.*, **82**, 597–608, https://doi.org/10.1175/1520-0477(2001)082<0597:DTAITU>2.3.CO;2.

Charney, J. G., 1947: The dynamics of long waves in a baroclinic westerly current. *J. Atmos. Sci.*, **4**, 136–162, https://doi.org/10.1175/1520-0469(1947)004<0136:TDOLWI>2.0.CO;2.

——, R. Fjörtoft, and J. von Neumann, 1950: Numerical integration of the barotropic vorticity equation. *Tellus*, **2**, 237–254, https://doi.org/10.1111/j.2153-3490.1950.tb00336.x.

Chen, C.-S., and C.-Y. Lin, 1997: A numerical study of airflow over Taiwan Island. *Atmos. Environ.*, **31**, 463–473, https://doi.org/10.1016/S1352-2310(96)00191-4.

——, C.-Y. Lin, Y.-J. Chuang, and H.-C. Yeh, 2002: A study of afternoon heavy rainfall in Taiwan during the Mei-yu season. *Atmos. Res.*, **65**, 129–149, https://doi.org/10.1016/S0169-8095(02)00061-3.

——, and Y.-L. Chen, 2003: The rainfall characteristics of Taiwan. *Mon. Wea. Rev.*, **131**, 1323–1341, https://doi.org/10.1175/1520-0493(2003)131<1323:TRCOT>2.0.CO;2.

Chen, T.-C., J.-D. Tsay, and E. S. Takle, 2016: A forecast advisory for afternoon thunderstorm occurrence in the Taipei Basin during summer developed from diagnostic analysis. *Wea. Forecasting*, **31**, 531–552, https://doi.org/10.1175/WAF-D-15-0082.1.

——, M.-C. Yen, J.-C. Hsieh, and R. W. Arritt, 1999: Diurnal and seasonal variations of the rainfall measured by the automatic rainfall and meteorological telemetry system in Taiwan. *Bull. Amer. Meteor. Soc.*, **80**, 2299–2312, https://doi.org/10.1175/1520-0477(1999)080<2299:DASVOT>2.0.CO;2.

Cheng, H.-W., S.-C. Yang, Y.-C. Liou, and C.-S. Chen, 2020: An investigation of the sensitivity of predicting a severe rainfall event in northern Taiwan to the upstream condition with a WRF-based radar data assimilation system. *SOLA*, **16**, 97–103, https://doi.org/10.2151/sola.2020-017.

Cheng, L.-W., and C.-K. Yu, 2019: Investigation of orographic precipitation over an isolated, three-dimensional complex topography with a dense gauge network, radar observations, and upslope model. *J. Atmos. Sci.*, **76**, 3387–3409, https://doi.org/10.1175/JAS-D-19-0005.1.

Cintineo, R. M., and D. J. Stensrud, 2013: On the predictability of supercell thunderstorm evolution. *J. Atmos. Sci.*, **70**, 1993–2011, https://doi.org/10.1175/JAS-D-12-0166.1.

Clark, D., A. Armua, C. Freeman, D. J. Brener, and A. Berera, 2021: Chaotic measure of the transition between two- and three-dimensional turbulence. *Phys. Rev. Fluids*, **6**, https://doi.org/10.1103/physrevfluids.6.054612.

Clark, P., N. Roberts, H. Lean, S. P. Ballard, and C. Charlton-Perez, 2016: Convection-permitting models: A step-change in rainfall forecasting. *Meteor. Appl.*, **23**, 165–181, https://doi.org/10.1002/met.1538.

Crook, N. A., 2001: Understanding Hector: The dynamics of island thunderstorms. *Mon. Wea. Rev.*, **129**, 1550–1563, https://doi.org/10.1175/1520-0493(2001)129<1550:UHTDOI>2.0.CO;2.

Dai, A., and K. E. Trenberth, 2004: The diurnal cycle and its depiction in the community climate system model. *J. Climate*, **17**, 930–951, https://doi.org/10.1175/1520-0442(2004)017<0930:TDCAID>2.0.CO;2.

Dalcher, A., and E. Kalnay, 1987: Error growth and predictability in operational ECMWF forecasts. *Tellus*, **39A**, 474–491, https://doi.org/10.1111/j.1600-0870.1987.tb00322.x.

Daley, R., 1981: Predictability experiments with a baroclinic model. *Atmos.-Ocean*, **19**, 77–89, https://doi.org/10.1080/07055900.1981.9649102.

Demko, J. C., B. Geerts, Q. Miao, and J. A. Zehnder, 2009: Boundary layer energy transport and cumulus development over a heated mountain: An observational study. *Mon. Wea. Rev.*, **137**, 447–468, https://doi.org/10.1175/2008MWR2467.1.

Done, J. M., G. C. Craig, S. L. Gray, and P. A. Clark, 2012: Case-to-case variability of predictability of deep convection in a mesoscale model. *Quart. J. Roy. Meteor. Soc.*, **138**, 638–648, https://doi.org/10.1002/qj.943.

Dowell, D. C., L. J. Wicker, and C. Snyder, 2011: Ensemble Kalman filter assimilation of radar observations of the 8 May 2003 Oklahoma City supercell: Influences of reflectivity observations on storm-scale analyses. *Mon. Wea. Rev.*, **139**, 272-294.

Durran, D. R., and J. A. Weyn, 2016: Thunderstorms do not get butterflies. *Bull. Amer. Meteor. Soc.*, **97**, 237–243, https://doi.org/10.1175/BAMS-D-15-00070.1.

——, and M. Gingrich, 2014: Atmospheric predictability: Why butterflies are not of practical importance. *J. Atmos. Sci.*, **71**, 2476–2488, https://doi.org/10.1175/JAS-D-14-0007.1.

Eady, E. T., 1949: Long waves and cyclone waves. *Tellus*, **1**, 33–52, https://doi.org/10.1111/j.2153-3490.1949.tb01265.x.

Ehrendorfer, M., R. M. Errico, and K. D. Raeder, 1999: Singular-vector perturbation growth in a primitive equation model with moist physics. *J. Atmos. Sci.*, **56**, 1627–1648, https://doi.org/10.1175/1520-0469(1999)056<1627:SVPGIA>2.0.CO;2.

Fang, X., Y.-H. Kuo, and A. Wang, 2011: The impacts of Taiwan topography on the predictability of typhoon Morakot's record-breaking rainfall: A high-resolution ensemble simulation. *Wea. Forecasting*, **26**, 613–633, https://doi.org/10.1175/WAF-D-10-05020.1.

Flesch, T. K., and G. W. Reuter, 2012: WRF model simulation of two Alberta flooding events and the impact of topography. *J. Hydrometeor.*, **13**, 695–708, https://doi.org/10.1175/JHM-D-11-035.1.

Fritsch, J. M., and R. E. Carbone, 2004: Improving quantitative precipitation forecasts in the warm season: A USWRP research and development Strategy. *Bull. Amer. Meteor. Soc.*, **85**, 955–966, https://doi.org/10.1175/BAMS-85-7-955.

Froude, L. S. R., L. Bengtsson, and K. I. Hodges, 2013: Atmospheric predictability revisited. *Tellus*, **65A**, 19022, https://doi.org/10.3402/tellusa.v65i0.19022.

Fu, D., and X. Guo, 2012: A cloud-resolving simulation study on the merging processes and effects of topography and environmental winds. *J. Atmos. Sci.*, **69**, 1232–1249, https://doi.org/10.1175/JAS-D-11-049.1.

Gopalakrishnan, S. G., S. B. Roy, and R. Avissar, 2000: An evaluation of the scale at which topographical features affect the convective boundary layer using large eddy simulations. *J. Atmos. Sci.*, **57**, 334–351, https://doi.org/10.1175/1520-0469(2000)057<0334:AEOTSA>2.0.CO;2.

Grimsdell, A. W., and W. M. Angevine, 2002: Observations of the afternoon transition of the convective boundary layer. *J. Appl. Meteor.*, **41**, 3–11, https://doi.org/10.1175/1520-0450(2002)041<0003:OOTATO>2.0.CO;2.

Hagen, M., J. van Baelen, and E. Richard, 2011: Influence of the wind profile on the initiation of convection in mountainous terrain. *Quart. J. Roy. Meteor. Soc.*, **137**, 224–235, https://doi.org/10.1002/qj.784.

Hanley, K. E., D. J. Kirshbaum, S. E. Belcher, N. M. Roberts, and G. Leoncini, 2011: Ensemble predictability of an isolated mountain thunderstorm in a high-resolution model. *Quart. J. Roy. Meteor. Soc.*, **137**, 2124–2137, https://doi.org/10.1002/qj.877.

Harlim, J., M. Oczkowski, J. A. Yorke, E. Kalnay, and B. R. Hunt, 2005: Convex error growth patterns in a global weather model. *Phys. Rev. Lett.*, **94**, 228501, https://doi.org/10.1103/PhysRevLett.94.228501.

Hassanzadeh, H., J. Schmidli, W. Langhans, L. Schlemmer, and C. Schär, 2016: Impact of topography on the diurnal cycle of summertime moist convection in idealized simulations. *Meteorologische Zeitschrift*, **25**, 181–194, https://doi.org/10.1127/metz/2015/0653.

Hohenegger, C., and C. Schär, 2007a: Atmospheric predictability at synoptic versus cloud-resolving scales. *Bull. Amer. Meteor. Soc.*, **88**, 1783–1794, https://doi.org/10.1175/BAMS-88-11-1783.

——, and ——, 2007b: Predictability and error growth dynamics in cloud-resolving models. *J. Atmos. Sci.*, **64**, 4467–4478, https://doi.org/10.1175/2007JAS2143.1.

——, D. Lüthi, and C. Schär, 2006: Predictability mysteries in cloud-resolving models. *Mon. Wea. Rev.*, **134**, 2095–2107, https://doi.org/10.1175/MWR3176.1.

Hong, S.–Y., and J.–O. J. Lim, 2006: The WRF single–moment 6–class microphysics scheme (WSM6). *J. Korean Meteor. Soc.*, **42**, 129–151.

Houze, R. A., 2012: Orographic effects on precipitating clouds. *Rev. Geophys.*, **50**, https://doi.org/10.1029/2011RG000365.

Iacono, M. J., J. S. Delamere, E. J. Mlawer, M. W. Shephard, S. A. Clough, and W. D. Collins, 2008: Radiative forcing by long-lived greenhouse gases: Calculations with the AER radiative transfer models. *J. Geophys. Res.*, **113**, D13103, https://doi.org/10.1029/2008JD009944.

Imamovic, A., L. Schlemmer, and C. Schär, 2019: Mountain volume control on deep-convective rain amount during episodes of weak synoptic forcing. *J. Atmos. Sci.*, **76**, 605–626, https://doi.org/10.1175/JAS-D-18-0217.1.

Janjić, Z. I., 1994: The step-mountain eta coordinate model: Further developments of the convection, viscous sublayer, and turbulence closure schemes. *Mon. Wea. Rev.*, **122**, 927–945, https://doi.org/10.1175/1520-0493(1994)122<0927:TSMECM>2.0.CO;2.

Janowiak, J. E., V. J. Dagostaro, V. E. Kousky, and R. J. Joyce, 2007: An examination of precipitation in observations and model forecasts during NAME with emphasis on the diurnal cycle. *J. Climate*, **20**, 1680–1692, https://doi.org/10.1175/JCLI4084.1.

Johnson, A., and Coauthors, 2014: Multiscale Characteristics and Evolution of Perturbations for Warm Season Convection-Allowing Precipitation Forecasts: Dependence on Background Flow and Method of Perturbation. *Mon. Wea. Rev.*, **142**, 1053–1073, https://doi.org/10.1175/MWR-D-13-00204.1.

Johnston, M. C., C. E. Holloway, and R. S. Plant, 2018: Cloud trails past Bermuda: A five-year climatology from 2012 to 2016. *Mon. Wea. Rev.*, **146**, 4039–4055, https://doi.org/10.1175/MWR-D-18-0141.1.

Judt, F., 2018: Insights into atmospheric predictability through global convection-permitting model simulations. *J. Atmos. Sci.*, **75**, 1477–1497, https://doi.org/10.1175/JAS-D-17-0343.1.

——, 2020: Atmospheric predictability of the tropics, middle latitudes, and polar regions explored through global storm-resolving simulations. *J. Atmos. Sci.*, **77**, 257–276, https://doi.org/10.1175/JAS-D-19-0116.1.

——, S. S. Chen, and J. Berner, 2016: Predictability of tropical cyclone intensity: Scale-dependent forecast error growth in high-resolution stochastic kinetic-energy backscatter ensembles. *Quart. J. Roy. Meteor. Soc.*, **142**, 43–57, https://doi.org/10.1002/qj.2626.

Jury, M. R., 2020: Diurnal summer climate of the Abyssinia highlands. *Int. J. Climatol.*, **40**, 4575–4585, https://doi.org/10.1002/joc.6476.

Kalnay, E., 2002: *Atmospheric Modeling, Data Assimilation and Predictability*. Cambridge: Cambridge University Press, 368 pp, https://doi.org/10.1017/CBO9780511802270.

Kerns, B. W. J., Y.-L. Chen, and M.-Y. Chang, 2010: The diurnal cycle of winds, rain, and clouds over Taiwan during the Mei-yu, summer, and autumn rainfall regimes. *Mon. Wea. Rev.*, **138**, 497–516, https://doi.org/10.1175/2009MWR3031.1.

Kirshbaum, D. J., B. Adler, N. Kalthoff, C. Barthlott, and S. Serafin, 2018: Moist orographic convection: Physical mechanisms and links to surface-exchange processes. *Atmos.*, **9**, https://doi.org/10.3390/atmos9030080.

——, and D. R. Durran, 2005: Atmospheric factors governing banded orographic convection. *J. Atmos. Sci.*, **62**, 3758–3774, https://doi.org/10.1175/JAS3568.1.

Kotsuki, S., K. Terasaki, K. Kanemaru, M. Satoh, T. Kubota, and T. Miyoshi, 2019: Predictability of record-breaking rainfall in Japan in July 2018: Ensemble forecast experiments with the near-real-time global atmospheric data assimilation system NEXRA. *SOLA*, **15A**, 1-7, https://doi.org/10.2151/sola.15A-001.

Kovacs, M., and D. J. Kirshbaum, 2016: Topographic impacts on the spatial distribution of deep convection over southern Quebec. *J. Appl. Meteor.*, **55**, 743–762, https://doi.org/10.1175/JAMC-D-15-0239.1.

Kuo, K.-T., and C.-M. Wu, 2019: The precipitation hotspots of afternoon thunderstorms over the Taipei Basin: Idealized numerical simulations. *J. Meteor. Soc. Japan*, **97**, 501–517, https://doi.org/10.2151/jmsj.2019-031.

Langhans, W., J. Schmidli, O. Fuhrer, S. Bieri, and C. Schär, 2013: Long-term simulations of thermally driven flows and orographic convection at convection-parameterizing and cloud-resolving resolutions. *J. Appl. Meteor.* **52**, 1490–1510, https://doi.org/10.1175/JAMC-D-12-0167.1.

Lawson, J. R., 2019: Predictability of idealized thunderstorms in buoyancy–shear space. *J. Atmos. Sci.*, **76**, 2653–2672, https://doi.org/10.1175/JAS-D-18-0218.1.

Leith, C. E., and R. H. Kraichnan, 1972: Predictability of turbulent flows. *J. Atmos. Sci.*, **29**, 1041–1058, https://doi.org/10.1175/1520-0469(1972)029<1041:POTF>2.0.CO;2.

Leoncini, G., R. S. Plant, S. L. Gray, and P. A. Clark, 2010: Perturbation growth at the convective scale for CSIP IOP18. *Quart. J. Roy. Meteor. Soc.*, **136**, 653–670, https://doi.org/10.1002/qj.587.

Leung, T. Y., M. Leutbecher, S. Reich, and T. G. Shepherd, 2019: Atmospheric predictability: Revisiting the inherent finite-time barrier. *J. Atmos. Sci.*, **76**, 3883–3892, https://doi.org/10.1175/JAS-D-19-0057.1.

Levizzani, V., F. Pinelli, M. Pasqui, S. Melani, A. G. Laing, and R. E. Carbone, 2010: A 10-year climatology of warm-season cloud patterns over Europe and the Mediterranean from Meteosat IR observations. *Atmos. Res.*, **97**, 555–576, https://doi.org/10.1016/j.atmosres.2010.05.014.

Li, J., T. Chen, and N. Li, 2017: Diurnal variation of summer precipitation across the central Tian Shan mountains. *J. Appl. Meteor*, **56**, 1537–1550, https://doi.org/10.1175/JAMC-D-16-0265.1.

Lilly, D.K., 1962: On the numerical simulation of buoyant convection. *Tellus*, **14**, 148–172, https://doi.org/10.3402/tellusa.v14i2.9537.

——, 1990: Numerical prediction of thunderstorms—has its time come? *Quart. J. Roy. Meteor. Soc.*, **116**, 779–798, https://doi.org/10.1002/qj.49711649402.

Lin, P.-F., P.-L. Chang, B. Jong-Dao Jou, J. W. Wilson, and R. D. Roberts, 2012: Objective prediction of warm season afternoon thunderstorms in northern Taiwan using a fuzzy logic approach. *Wea. Forecasting*, **27**, 1178–1197, https://doi.org/10.1175/WAF-D-11-00105.1.

Lorenz, E. N., 1963: Deterministic nonperiodic flow. *J. Atmos. Sci.*, **20**, 130–141, https://doi.org/10.1175/1520-0469(1963)020<0130:DNF>2.0.CO;2.

——, 1969: The predictability of a flow which possesses many scales of motion. *Tellus*, **21**, 289–307, https://doi.org/10.1111/j.2153-3490.1969.tb00444.x.

——, 1982: Atmospheric predictability experiments with a large numerical model. *Tellus*, **34**, 505–513, https://doi.org/10.1111/j.2153-3490.1982.tb01839.x.

Magnusson, L., and E. Källén, 2013: Factors Influencing Skill Improvements in the ECMWF Forecasting System. *Mon. Wea. Rev.*, **141**, 3142–3153, https://doi.org/10.1175/MWR-D-12-00318.1.

Mapes, B., S. Tulich, T. Nasuno, and M. Satoh, 2008: Predictability aspects of global aqua-planet simulations with explicit convection. *J. Meteor. Soc. Japan*, **86A**, 175–185, https://doi.org/10.2151/jmsj.86A.175.

Markowski, P. M., 2020: What is the intrinsic predictability of tornadic supercell thunderstorms? *Mon. Wea. Rev.*, **148**, 3157–3180, https://doi.org/10.1175/MWR-D-20-0076.1.

Melhauser, C., and F. Zhang, 2012: Practical and Intrinsic Predictability of Severe and Convective Weather at the Mesoscales. *J. Atmos. Sci.*, **69**, 3350–3371, https://doi.org/10.1175/JAS-D-11-0315.1.

Métais, O., and M. Lesieur, 1986: Statistical predictability of decaying turbulence. *J. Atmos. Sci.*, **43**, 857–870, https://doi.org/10.1175/1520-0469(1986)043<0857:SPODT>2.0.CO;2.

Miao, J.-E., and M.-J. Yang, 2020: A modeling study of the severe afternoon thunderstorm event at Taipei on 14 June 2015: The roles of sea breeze, microphysics, and terrain. *J. Meteor. Soc. Japan*, **98**, 129–152, https://doi.org/10.2151/jmsj.2020-008.

Miglietta, M. M., A. Manzato, and R. Rotunno, 2016: Characteristics and predictability of a supercell during HyMeX SOP1. *Quart. J. Roy. Meteor. Soc.*, **142**, 2839–2853, https://doi.org/10.1002/qj.2872.

Morss, R. E., C. Snyder, and R. Rotunno, 2009: Spectra, spatial scales, and predictability in a quasigeostrophic Model. *J. Atmos. Sci.*, **66**, 3115–3130, https://doi.org/10.1175/2009JAS3057.1.

Mu, M., W. Duan, and Y. Tang, 2017: The predictability of atmospheric and oceanic motions: Retrospect and prospects. *Sci. China Earth Sci*, **60**, 2001–2012, https://doi.org/10.1007/s11430-016-9101-x.

Mulholland, J. P., S. W. Nesbitt, R. J. Trapp, and J. M. Peters, 2020: The influence of terrain on the convective environment and associated convective morphology from an idealized modeling perspective. *J. Atmos. Sci.*, **77**, 3929–3949, https://doi.org/10.1175/JAS-D-19-0190.1.

Muller, C., 2013: Impact of convective organization on the response of tropical precipitation extremes to warming. *J. Climate*, **26**, 5028–5043, https://doi.org/10.1175/JCLI-D-12-00655.1.

Nastrom, G. D., and K. S. Gage, 1985: A Climatology of atmospheric wavenumber spectra of wind and temperature observed by commercial aircraft. *J. Atmos. Sci.*, **42**, 950–960, https://doi.org/10.1175/1520-0469(1985)042<0950:ACOAWS>2.0.CO;2.

Nesbitt, S. W., D. J. Gochis, and T. J. Lang, 2008: The diurnal cycle of clouds and precipitation along the Sierra Madre Occidental observed during NAME-2004: Implications for warm season precipitation estimation in complex terrain. *J. Hydrometeor.*, **9**, 728–743, https://doi.org/10.1175/2008JHM939.1.

Ngan, K., and G. E. Eperon, 2011: Middle atmosphere predictability in a numerical weather prediction model: revisiting the inverse error cascade. *Quart. J. Roy. Meteor. Soc.*, **138**, 1366–1378, https://doi.org/10.1002/qj.984.

——, P. Bartello, and D. N. Straub, 2009: Predictability of rotating stratified turbulence. *J. Atmos. Sci.*, **66**, 1384–1400, https://doi.org/10.1175/2008JAS2799.1.

Nielsen, E. R., and R. S. Schumacher, 2016: Using convection-allowing ensembles to understand the predictability of an extreme rainfall event. *Mon. Wea. Rev.*, **144**, 3651–3676, https://doi.org/10.1175/MWR-D-16-0083.1.

Nomura, S., and T. Takemi, 2011: Environmental stability for afternoon rain events in the Kanto Plain in summer. *SOLA*, **7**, 9–12, https://doi.org/10.2151/sola.2011-003.

Palmer, T. N., A. Döring, and G. Seregin, 2014: The real butterfly effect. *Nonlinearity*, **27**, R123–R141, https://doi.org/10.1088/0951-7715/27/9/r123.

Persson, A., 2005: Early operational numerical weather prediction outside the USA: An historical introduction. Part 1: Internationalism and engineering NWP in Sweden, 1952–69. *Meteor. Appl.*, **12**, 135–159, https://doi.org/DOI: 10.1017/S1350482705001593.

Potvin, C. K., E. M. Murillo, M. L. Flora, and D. M. Wheatley, 2017: Sensitivity of supercell Simulations to Initial-Condition Resolution. *J. Atmos. Sci.*, **74**, 5–26, https://doi.org/10.1175/JAS-D-16-0098.1.

Powers, J. G., and Coauthors, 2017: The weather research and forecasting model: Overview, system efforts, and future directions. *Bull. Amer. Meteor. Soc.*, **98**, 1717–1737, https://doi.org/10.1175/BAMS-D-15-00308.1.

Reynolds, C. A., P. J. Webster, and E. Kalnay, 1994: Random Error Growth in NMC's Global Forecasts. *Mon. Wea. Rev.*, **122**, 1281–1305, https://doi.org/10.1175/1520-0493(1994)122<1281:REGING>2.0.CO;2.

Richardson, L.F., 1922: *Weather Prediction by Numerical Process*. Cambridge Univ. Press, 236 pp.

Roe, G. H., 2005: Orographic precipitation. *Annu. Rev. Earth Planet. Sci.*, **33**, 645–671, https://doi.org/10.1146/annurev.earth.33.092203.122541.

Romatschke, U., and R. A. Houze, 2010: Extreme summer convection in South America. *J. Climate*, **23**, 3761–3791, https://doi.org/10.1175/2010JCLI3465.1.

Rotunno, R., and C. Snyder, 2008: A generalization of Lorenz's model for the predictability of flows with many scales of motion. *J. Atmos. Sci.*, **65**, 1063–1076, https://doi.org/10.1175/2007JAS2449.1.

Schmidli, J., 2013: Daytime heat transfer processes over mountainous terrain. *J. Atmos. Sci.*, **70**, 4041–4066, https://doi.org/10.1175/JAS-D-13-083.1.

——, S. Böing, and O. Fuhrer, 2018: Accuracy of simulated diurnal valley winds in the Swiss Alps: Influence of grid resolution, topography filtering, and land surface datasets. *Atmos.*, **9**, https://doi.org/10.3390/atmos9050196.

Selz, T., 2019: Estimating the intrinsic limit of predictability using a stochastic convection scheme. *J. Atmos. Sci.*, **76**, 757–765, https://doi.org/10.1175/JAS-D-17-0373.1.

——, and G. C. Craig, 2015: Upscale error growth in a high-resolution simulation of a summertime weather event over Europe. *Mon. Wea. Rev.*, **143**, 813–827, https://doi.org/10.1175/MWR-D-14-00140.1.

Serafin, S., and Coauthors, 2018: Exchange processes in the atmospheric boundary layer over mountainous terrain. *Atmos.*, **9**, https://doi.org/10.3390/atmos9030102.

Simmons, A. J., and A. Hollingsworth, 2002: Some aspects of the improvement in skill of numerical weather prediction. *Quart. J. Roy. Meteor. Soc.*, **128**, 647–677, https://doi.org/10.1256/003590002321042135.

——, R. Mureau, and T. Petroliagis, 1995: Error growth and estimates of predictability from the ECMWF forecasting system. *Quart. J. Roy. Meteor. Soc.*, **121**, 1739–1771, https://doi.org/10.1002/qj.49712152711.

Skamarock, W. C., 2004: Evaluating mesoscale NWP models using kinetic energy spectra. *Mon. Wea. Rev.*, 132, 3019–3032, https://doi.org/10.1175/MWR2830.1.

——, and Coauthors, 2019: A description of the Advanced Research WRF Model version 4. No. NCAR/TN-556+STR, 145 pp., http://dx.doi.org/10.5065/1dfh-6p97.

——, S.-H. Park, J. B. Klemp, and C. Snyder, 2014: Atmospheric kinetic energy spectra from global high-resolution nonhydrostatic simulations. *J. Atmos. Sci.*, **71**, 4369–4381, https://doi.org/10.1175/JAS-D-14-0114.1.

Smagorinsky, J., 1963: General circulation experiments with the primitive equations. *Mon. Wea. Rev.*, **91**, 99–164, https://doi.org/10.1175/1520-0493(1963)091<0099:GCEWTP>2.3.CO;2.

Smolarkiewicz, P. K., R. M. Rasmussen, and T. L. Clark, 1988: On the dynamics of Hawaiian cloud bands: Island forcing. *J. Atmos. Sci.*, **45**, 1872–1905, https://doi.org/10.1175/1520-0469(1988)045<1872:OTDOHC>2.0.CO;2.

Straus, D., and D. Paolino, 2008: Intermediate time error growth and predictability: tropics versus mid-latitudes. *Tellus*, **61A**, 579–586, https://doi.org/10.1111/j.1600-0870.2009.00411.x.

Sun, Y. Q., and F. Zhang, 2016: Intrinsic versus practical limits of atmospheric predictability and the significance of the butterfly effect. *J. Atmos. Sci.*, **73**, 1419–1438, https://doi.org/10.1175/JAS-D-15-0142.1.

——, and ——, 2020: A new theoretical framework for understanding multiscale atmospheric predictability. *J. Atmos. Sci.*, **77**, 2297–2309, https://doi.org/10.1175/JAS-D-19-0271.1.

——, R. Rotunno, and F. Zhang, 2017: Contributions of moist convection and internal gravity waves to building the atmospheric −5/3 kinetic energy spectra. *J. Atmos. Sci.*, **74**, 185–201, https://doi.org/10.1175/JAS-D-16-0097.1.

Surcel, M., I. Zawadzki, and M. K. Yau, 2015: A study on the scale dependence of the predictability of precipitation patterns. *J. Atmos. Sci.*, **72**, 216–235, https://doi.org/10.1175/JAS-D-14-0071.1.

Takemi, T., 2014: Characteristics of summertime afternoon rainfall and its environmental conditions in and around the Nobi Plain. *SOLA*, **10**, 158–162, https://doi.org/10.2151/sola.2014-033.

——, and R. Rotunno, 2003: The effects of subgrid model mixing and numerical filtering in simulations of mesoscale cloud systems. *Mon. Wea. Rev.*, **131**, 2085–2101, https://doi.org/10.1175/1520-0493(2003)131<2085:TEOSMM>2.0.CO;2.

——, and S. Tsuchida, 2014: Statistical analysis on precipitation events over the Kinki District, Japan in summer (in Japanese with an English abstract). *Annuals of Disas. Prev. Res. Inst., Kyoto Univ.*, **57B**, 216-238, https://www.dpri.kyoto-u.ac.jp/nenpo/no57/ronbunB/a57b0p24.pdf.

Tewari, M., and Coauthors, 2004: Implementation and verification of the unified NOAH land surface model in the WRF model. *20th conference on weather analysis and forecasting16th conference on numerical weather prediction*, pp. 11–15.

Thompson, P. D., 1953: On the theory of large-scale disturbances in a two-dimensional baroclinic equivalent of the atmosphere. *Quart. J. Roy. Meteor. Soc.*, **79**, 51–69, https://doi.org/10.1002/qj.49707933905.

——, 1957: Uncertainty of initial state as a factor in the predictability of large scale atmospheric flow patterns. *Tellus*, **9**, 275–295, https://doi.org/10.1111/j.2153-3490.1957.tb01885.x.

Tompkins, A. M., and A. G. Semie, 2017: Organization of tropical convection in low vertical wind shears: Role of updraft entrainment. *J. Adv. Model. Earth Syst.*, **9**, 1046–1068, https://doi.org/10.1002/2016MS000802.

Toth, Z., and E. Kalnay, 1993: Ensemble forecasting at NMC: The generation of perturbations. *Bull. Amer. Meteor. Soc.*, **74**, 2317–2330, https://doi.org/10.1175/1520-0477(1993)074<2317:EFANTG>2.0.CO;2.

Tracton, M. S., and E. Kalnay, 1993: Operational ensemble prediction at the National Meteorological Center: Practical Aspects. *Wea. Forecasting*, **8**, 379–398, https://doi.org/10.1175/1520-0434(1993)008<0379:OEPATN>2.0.CO;2.

Tribbia, J. J., and D. P. Baumhefner, 2004: Scale interactions and atmospheric predictability: An updated perspective. *Mon. Wea. Rev.*, **132**, 703–713, https://doi.org/10.1175/1520-0493(2004)132<0703:SIAAPA>2.0.CO;2.

Vergeiner, I., and E. Dreiseitl, 1987: Valley winds and slope winds — Observations and elementary thoughts. *Meteor. Atmos. Phys.*, **36**, 264–286, https://doi.org/10.1007/BF01045154.

Vincent, C. L., and T. P. Lane, 2016: Evolution of the diurnal precipitation cycle with the passage of a Madden–Julian oscillation event through the Maritime Continent. *Mon. Wea. Rev.*, **144**, 1983–2005, https://doi.org/10.1175/MWR-D-15-0326.1.

Vukicevic, T., and R. M. Errico, 1990: The Influence of Artificial and Physical Factors upon Predictability Estimates Using a Complex Limited-Area Model. *Mon. Wea. Rev.*, **118**, 1460–1482, https://doi.org/10.1175/1520-0493(1990)118<1460:TIOAAP>2.0.CO;2.

Wallace, J. M., 1975: Diurnal variations in precipitation and thunderstorm frequency over the conterminous United States. *Mon. Wea. Rev.*, **103**, 406–419, https://doi.org/10.1175/1520-0493(1975)103<0406:DVIPAT>2.0.CO;2.

Walser, A., D. Lüthi, and C. Schär, 2004: Predictability of Precipitation in a Cloud-Resolving Model. *Mon. Wea. Rev.*, **132**, 560–577, https://doi.org/10.1175/1520-0493(2004)132<0560:POPIAC>2.0.CO;2.

Weisman, M. L., and J. B. Klemp, 1982: The Dependence of Numerically Simulated Convective Storms on Vertical Wind Shear and Buoyancy. *Mon. Wea. Rev.*, **110**, 504–520, https://doi.org/10.1175/1520-0493(1982)110<0504:TDONSC>2.0.CO;2.

Weyn, J. A., and D. R. Durran, 2017: The dependence of the predictability of mesoscale convective systems on the horizontal scale and amplitude of initial errors in idealized simulations. *J. Atmos. Sci.*, **74**, 2191–2210, https://doi.org/10.1175/jas-d-17-0006.1.

——, and ——, 2018: Ensemble spread grows more rapidly in higher-resolution simulations of deep convection. *J. Atmos. Sci.*, **75**, 3331–3345, https://doi.org/10.1175/jas-d-17-0332.1.

——, and ——, 2019: The scale dependence of initial-condition sensitivities in simulations of convective systems over the southeastern United States. *Quart. J. Roy. Meteor. Soc.*, **145**, 57–74, https://doi.org/10.1002/qj.3367.

White, J. D., A. Aiyyer, and J. O. H. Russell, 2021: The impact of orography on the African easterly wave stormtrack. *J. Geophys. Res. Atmos.*, **126**, e2020JD033749, https://doi.org/10.1029/2020JD033749.

Whiteman, C.D., 1990: Observations of thermally developed wind systems in mountainous terrain. *Atmospheric Processes over Complex Terrain, Meteor. Monogr.*, No. 23, Amer. Meteor, 5-42, Soc. https://doi.org/10.1007/978-1-935704-25-6_2.

Wu, N., X. Zhuang, J. Min, and Z. Meng, 2020: Practical and intrinsic predictability of a warm-sector torrential rainfall event in the south China monsoon region. *J. Geophys. Res. Atmos.*, **125**, e2019JD031313, https://doi.org/10.1029/2019JD031313.

Ying, Y., and F. Zhang, 2017: Practical and intrinsic predictability of multiscale weather and convectively coupled equatorial waves during the active phase of an MJO. *J. Atmos. Sci.*, **74**, 3771–3785, https://doi.org/10.1175/JAS-D-17-0157.1.

Zhang, F., C. Snyder, and R. Rotunno, 2003: Effects of moist convection on mesoscale predictability. *J. Atmos. Sci.*, **60**, 1173–1185, https://doi.org/10.1175/1520-0469(2003)060<1173:EOMCOM>2.0.CO;2.

——, and D. Tao, 2013: Effects of vertical wind shear on the predictability of tropical cyclones. *J. Atmos. Sci.*, **70**, 975–983, https://doi.org/10.1175/JAS-D-12-0133.1.

——, N. Bei, R. Rotunno, C. Snyder, and C. C. Epifanio, 2007: Mesoscale predictability of moist baroclinic waves: Convection-permitting experiments and multistage error growth dynamics. *J. Atmos. Sci.*, **64**, 3579–3594, https://doi.org/10.1175/JAS4028.1.

——, Y. Q. Sun, L. Magnusson, R. Buizza, S.-J. Lin, J.-H. Chen, and K. Emanuel, 2019: What is the predictability limit of midlatitude weather? *J. Atmos. Sci.*, **76**, 1077–1091, https://doi.org/10.1175/JAS-D-18-0269.1.

Zhang, Y., F. Zhang, D. J. Stensrud, and Z. Meng, 2015: Practical predictability of the 20 May 2013 tornadic thunderstorm event in Oklahoma: Sensitivity to synoptic timing and topographical influence. *Mon. Wea. Rev.*, **143**, 2973–2997, https://doi.org/10.1175/MWR-D-14-00394.1.

——, ——, ——, and ——, 2016: Intrinsic predictability of the 20 May 2013 tornadic thunderstorm event in Oklahoma at storm scales. *Mon. Wea. Rev.*, **144**, 1273–1298, https://doi.org/10.1175/MWR-D-15-0105.1.

Zhuang, X., J. Min, L. Zhang, S. Wang, N. Wu, and H. Zhu, 2020: Insights into convective-scale predictability in east China: Error growth dynamics and associated impact on precipitation of warm-season convective events. *Adv. Atmos. Sci.*, **37**, 893–911, https://doi.org/10.1007/s00376-020-9269-5.